CHALMERS
UNIVERSITY OF TECHNOLOGY

Finite-element modelling of compressed fibrous materials

Modelling of the sound absorption and transmission properties of multi-layer assemblies including compressed fibrous materials and comparison to the results obtained from the transfer-matrix-method and measurements

Master's thesis in Master Program Sound and Vibration

PABLO PANTER and AXEL KÅBERGER

Department of Architecture and Civil Engineering
CHALMERS UNIVERSITY OF TECHNOLOGY
Master's thesis ACEX30
Gothenburg, Sweden 2020

MASTER'S THESIS ACEX30

Finite-element modelling of compressed fibrous materials

Modelling of the sound absorption and transmission properties of multi-layer assemblies including compressed fibrous materials and comparison to the results obtained from the transfer-matrix-method and measurements

PABLO PANTER and AXEL KÅBERGER

Department of Architecture and Civil Engineering
Division of Applied Acoustics
CHALMERS UNIVERSITY OF TECHNOLOGY
Gothenburg, Sweden 2020

Finite-element modelling of compressed fibrous materials
Modelling of the sound absorption and transmission properties of multi-layer assemblies including compressed fibrous materials and comparison to the results obtained from the transfer-matrix-method and measurements
PABLO PANTER and AXEL KÅBERGER

Supervisor: François-Xavier Bécot (Matelys – Research Lab), Sophie Girolami and Krister Fredriksson (Volvo Group)
Examiner: Professor Wolfgang Kropp (Department of Architecture and Civil Engineering)

Department of Architecture and Civil Engineering
Division of Applied Acoustics
Chalmers University of Technology
SE-412 96 Gothenburg
Telephone +46 31 772 1000

Typeset in LaTeX
Gothenburg, Sweden 2020

Finite-element modelling of compressed fibrous materials
Modelling of the sound absorption and transmission properties of multi-layer assemblies including compressed fibrous materials and comparison to the results obtained from the transfer-matrix-method and measurements
PABLO PANTER and AXEL KÅBERGER
Department of Architecture and Civil Engineering
Chalmers University of Technology

Abstract

This thesis work addresses the finite-element-method (FEM) modelling of the sound transmission and absorption properties of multi-layer systems including compressed fibrous materials. The investigated system is a noise shield which is used for encapsulating the engine in trucks. Today, the complex surface impedance is used to represent this system in FEM modelling. With this method, the back face of the noise shield is considered as fully reflective and there is no possibility to assess transmission through the encapsulation. The present thesis work aims for improving the currently employed methods by taking more complex information into account, specifically by applying *Biot's theory* in the modelling of poroelastic materials.
The results of different FEM models are compared to the results obtained from transfer-matrix-method (TMM) models and measured data. Three out of seven models have been found to provide a good agreement between the FEM and TMM results as well as to measured data of the absorption coefficient.
A mesh size sensitivity study indicates that six to seven linear elements per smallest wavelength are sufficient to decrease the mesh-related error in the calculated sound transmission loss to below 1 dB for the investigated system. However, it has been found that today there are still hindering limits in terms of computational power when modelling soft poroelastic materials in FEM due to the small apparent wavelengths.

Keywords: FEM, poroelastic, multi-layer, sound transmission, sound absorption

Acknowledgements

First and foremost, we would like to thank our supervisors at Volvo Group, Krister Fredriksson and Sophie Girolami, and François-Xavier Bécot from Matelys – Research Lab for their excellent supervision. Without your help and guidance, this thesis work could not have been realised in this way!

Thank you Krister for having an open ear for all our problems, and for keeping us well organised. Thank you also for allowing us to take a slightly different path than initially planned, in our adaptation to the Covid-19 pandemic. Thank you Sophie for helping out whenever we have had issues with using Actran. Thank you François-Xavier for your excellent assistance in helping us to understand the necessary theoretical backgrounds, helping us with using AlphaCell and giving a lot of input to the project overall. Also a huge thank you for always answering spontaneous questions, even when everything else was shut down. We also want to thank our group leader at Volvo Group, Niusha Parsi, for finding a nice workspace for us and making sure we always had everything that we needed. A large thank you to everyone in the Corporate Standards group at Volvo Group for integrating us that nicely and teaching Pablo some Swedish. You made the weeks that we spent at Volvo as pleasant as possible for us and the fika breaks surely were a great source of energy.

Furthermore, we want to thank Börje Wijk and Wolfgang Kropp from Chalmers for making it possible that we could at least have our Kundt's tube measurements, even though the planned sound transmission measurement had to be cancelled due to the pandemic.

Last but not least, an indescribable thank you to our ever supporting and entertaining colleagues at MPSOV for two amazing years. The camaraderie we have developed is indeed a precious thing that we are sure will last many years.

Pablo Panter and Axel Kåberger, Gothenburg, July 2020

Contents

List of Figures

List of Tables

1 Introduction

1.1 Background

Noise pollution is an important issue in today's society. One part of the work for creating a better environment is to lower the noise emissions from vehicles. There will be a stepwise increase of the demands on vehicle noise in the future which puts higher design demands on the implemented noise treatments, one of which is to encapsulate the noise source. While heavy plating would be preferable for this task, demands on weight make it difficult. Therefore, the encapsulation is realised with complex multi-layer structures including compressed fibrous materials.

In the development process, the first steps are done in a finite-element-method (FEM) software environment. Today, the complex surface impedance is used to represent the absorptive properties of the poroelastic encapsulation in FEM modelling. With this method, the back face of the noise encapsulation shield is considered as fully reflective and there is no possibility to assess transmission through the encapsulation. Since the characterisation of sound transmission properties is of utmost importance for materials which are used for encapsulation, it is necessary to improve the current methods by taking more complex information into account.

This thesis work covers an important aspect in the development of better simulation procedures by focusing on the FEM modelling of the sound absorption and transmission properties of multi-layer structures including compressed poroelastic materials. Improving the simulation methods for assessing sound transmission through poroelastic materials will enable the development of configurations with higher sound transmission losses and thereby contribute to the reduction of noise pollution.

1.2 Aim

The aim of this thesis is to equip the engineers with a relevant method for modelling the performance of a multi-layer sound shield system with sufficient precision. This includes comparisons of different mathematical models in terms of accuracy and costs, such as computational time or evaluation of material properties. The thesis project looks for ways of simplifying the model while being accurate enough for engineering purposes. The FEM simulations are verified by comparing the results to the results from a transfer-matrix-method (TMM) implementation and measurements. While both sound absorption and transmission measurements have been planned, only the absorption measurements could be carried out.

This thesis relies on the use of third-party software. The FEM simulations are carried out using Actran (version 2020) and the TMM simulations are carried out using AlphaCell (version 12.0). While essential modelling approaches for poroelastic materials are available for both applications, certain modelling approaches are only available in one of them. Therefore, this thesis work also aims for establishing a link between both methods by investigating the equivalences of different modelling approaches. This will provide the engineers with tools to easily switch between both methods.

In the used software, parts of the calculations are hidden as intellectual property. Since the aim of the thesis is to provide tools for engineers and not to be a scientific review, this is deemed acceptable. It does, however, mean that some theoretical details are reduced to more conceptual explanations.

1.3 Report structure

Setting the basis for all following investigations, the theory behind the modelling of poroelastic materials, including the implementation in FEM and TMM, is presented in Chapter 2. The main part of the thesis then is split up into Chapter 3, which deals with modelling the sound absorption, and Chapter 4, which deals with modelling the sound transmission loss. These chapters contain descriptions of the applied methodology, as well as the simulation results including a discussion. Since the determination of the best modelling approaches is presented as an iterative process where subsequent models are based on the results obtained from previous models, the results are discussed where they are presented. Chapter 5 then provides a more general discussion, relating the results obtained from the absorption and transmission modelling to each other. The main results of this thesis work are then summarised in Chapter 6.

Appendix A presents theory which has been used in the analysis of the simulation results but is not explicitly part of the theory describing the propagation of sound in porous media. Appendix B gives a summary of the parameters which are used in the different fluid phase models. Appendix C presents a few additional investigations that complement the results presented in Chapter 3 and 4. Appendix D presents the results from Kundt's tube measurements, which have been carried out as a part of this thesis work but have not been used in the main investigation. Appendix E presents the planning that has been made to prepare a transmission loss measurement which has not been carried out.

All information in Appendix F is confidential and only included in the internal version of the report.

2

Theory

This chapter gives an introduction to the theory behind the modelling of poroelastic materials in Section 2.1, before giving a conceptual overview on the use of the transfer-matrix-method for modelling poroelastic materials in Section 2.2 and the finite-element method in Section 2.3.

2.1 Propagation of sound in porous media

Porous materials can be classified into cellular materials, granular materials, fibrous materials and perforated plates. These materials have in common that they consist of a porous solid structure – usually referred to as *solid phase*, *frame* or *skeleton* – which is filled with a fluid, usually air – referred to as *fluid phase*. The propagation of sound in air-saturated porous media can be described at different levels of accuracy and complexity. Early analytical solutions are based on Kirchhoff's expressions for the propagation of sound in uniform, circular tubes. Since analytical solutions are only possible for simple geometries and not applicable to the complex microstructure of common porous materials, several (mostly phenomenological) models have been developed later [2]. These assume the material skeleton to be rigid and motionless. Using *Biot's theory*, the elastic properties of the material skeleton can be taken into account by coupling the fluid and solid phases.
In short, the different types of models can be classified as follows [2]:

1. Motionless skeleton models
   The material skeleton is assumed rigid and motionless. Dissipation of energy in the solid phase is not considered. The material is represented by an *equivalent fluid*.
   (a) Analytical models
      - Only possible for simple pore geometries.
      - The material is assumed to be locally reacting, i.e. there are no connections between the pores and the input impedance does not depend on the angle of incidence.
   (b) Empirical models
      - Usually require only a small set of parameters.
   (c) Semi-phenomenological models
      - Models developed for more complicated pore structures. Require a larger set of parameters.
2. Diphasic models (*Biot's theory*)

- Wave propagation in both the fluid and the solid phase and interaction between both.
- Elastic properties of the skeleton and the dissipation in the solid phase are taken into account.
- Make use of *equivalent fluid* models to account for the dissipation in the fluid phase.

In the following, after a short section on analytical solutions, the different motionless skeleton models are presented in Section 2.1.2. Section 2.1.3 then establishes the link between the dissipations in the fluid and the solid phase by the use of *Biot's theory*.

2.1.1 Analytical solutions for sound propagation in porous media with cylindrical pores

The exact solution for the propagation of sound in a uniform, circular tube, as given by Kirchhoff in 1868, accounts for the effects of thermal conductivity and air viscosity in tubes of arbitrary diameter. It was found that these equations are unnecessarily complicated for many applications [3]. A simpler, approximate model was introduced by Zwikker and Kosten in 1949 and has since then been widely in use [4]. In the model by Zwikker and Kosten, the effects of viscosity and thermal conductivity are treated separately and are summarised in terms of complex compressibility and bulk modulus functions. Assuming that the thermal conductivity is zero gives the expression for the complex density and assuming that the viscosity is zero gives the expression for the complex bulk modulus [3]. The expressions of Zwikker and Kosten were only justified for the extreme of low and high frequencies, but numerical comparisons of their model with the exact Kirchhoff solution revealed a good agreement over a wide range of frequencies [3]. More recently, in 1991, Stinson has shown that the Zwikker and Kosten equations can be derived analytically from the more exact Kirchhoff equations when certain choices of tube radius and frequency are applied. Thereby, the validity of the Zwikker-Kosten equations in the range of frequency and tube radius for which these assumptions can be made was proven [3].
In his derivation of the Zwikker-Kosten equations Stinson limits the range of frequencies f and tube radii r_w to

$$r_\mathrm{w} f^{3/2} < 10^6 \text{ cm s}^{-3/2} \quad \text{and} \quad r_\mathrm{w} > 10^{-3} \text{ cm}. \tag{2.1}$$

Under this regime, several approximations can be made which lead to the separation of effects of viscosity and thermal conduction. This then gives the following formulas for the complex effective density ρ and the complex effective bulk modulus K for circular tubes, which are equivalent to the equations derived by Zwikker and Kosten [3]:

$$\rho(\omega) = \rho_0 \left\{ 1 - 2\left(-\mathrm{j}\frac{\omega}{\nu}\right)^{-1/2} \frac{G\left(r_\mathrm{w}\left(-\mathrm{j}\frac{\omega}{\nu}\right)^{1/2}\right)}{r_\mathrm{w}} \right\}^{-1}, \tag{2.2}$$

$$K(\omega) = \left(\frac{1}{\gamma P_0}\right)^{-1} \left\{ 1 + 2\left(\gamma - 1\right)\left(-\mathrm{j}\frac{\omega\gamma}{\nu'}\right)^{-1/2} \frac{G\left(r_\mathrm{w}\left(-\mathrm{j}\frac{\omega\gamma}{\nu'}\right)^{1/2}\right)}{r_\mathrm{w}} \right\}^{-1} \tag{2.3}$$

with

$$G(\zeta) = \frac{J_1(\zeta)}{J_0(\zeta)}, \tag{2.4}$$

where J_0 is the Bessel function of the first kind with order zero and

$$\upsilon = \gamma / \rho_0, \quad \upsilon' = \kappa / (\rho_0 C_\text{v}). \tag{2.5}$$

In these equations, r_w is the radius of the tube, c the speed of sound in the gas, ρ_0 the density of the gas, γ the specific heat ratio C_p/C_v, κ the thermal conductivity of the gas, P_0 the equilibrium pressure of air, C_v the specific heat (per unit mass) at constant volume and C_p the specific heat at constant pressure.

2.1.2 Sound propagation in porous media having a rigid and motionless frame

For common porous materials with complex micro-structures, analytical solutions are not possible. To describe sound propagation in such materials, several empirical and semi-phenomenological models have been developed which provide a description on a large scale [2].
For a rigid frame, the air inside of the pores can be replaced by an *equivalent fluid* on the macroscopic scale. The acoustical properties of this fluid can be described by the complex wavenumber k and the complex characteristic impedance Z_C. The viscous and inertial interaction with the frame is taken into account by a complex effective density $\tilde{\rho}$ and bulk modulus $\tilde{K}$, as it has been shown for the Zwikker-Kosten model. The main condition for this to be valid is that the characteristic dimensions of the pores are much smaller than the wavelength and that, at the microscopic scale, the saturating fluid can behave as an incompressible fluid [2].
In the following, a number of *equivalent fluid* models is introduced (Section 2.1.2.2). These models are based on several parameters characterising the skeleton which are introduced first. The material parameters change when a material is compressed. A model for this is described in Section 2.1.2.3. In Section 2.1.2.4 it is described how the complex wavenumber and the complex characteristic impedance can be obtained from the complex effective densities and bulk moduli given by the different models. Finally, Section 2.1.2.5 describes the perforated plate modelling approach.

Table B.1 gives an overview on which material parameters are used in which models.

2.1.2.1 Fluid phase parameters

Open porosity ϕ: *Open porosity*, or commonly referred to as just porosity, is a measure of how large the portion of the material is that consists of connected channels. It is defined as:

$$\phi = V_\text{o} / V_\text{t}, \tag{2.6}$$

where V_o is the volume of connected (open) pores and V_t the total volume of the medium. Open porosity is dimensionless [5][6].

Static air flow resistivity σ: One of the most central parameters in poromechanics is the *static air flow resistivity σ*. It is derived from *Darcy's Law*, which determines the ratio between the static gas pressure at the two sides of medium and the airflow speed [7]. The generalisation for 3D space was made by M. Hubbert, resulting in the following equation:

$$\phi\vec{v} = -\frac{k_0}{\eta}(\vec{\Delta}p - \rho\vec{g}), \tag{2.7}$$

where $\phi\vec{v}$ represents the volume flow, η is the dynamic viscosity of air, ρ the mass density, k_0 is the static permeability of the material, $\vec{\Delta}p$ the pressure gradient and g the gravity. By defining $\sigma = \frac{\eta}{k_0}$ and assuming that $\vec{\Delta}p \gg \rho\vec{g}$, the expression is further simplified to:

$$\sigma = \frac{-\vec{\Delta}p}{\phi\vec{v}} \tag{2.8}$$

The static air flow resistivity is specific for a medium and has the SI units $\mathrm{Ns/m^4}$ [8][9].

High frequency limit of tortuosity α_∞: The high-frequency limit of tortuosity can be interpreted as a measure of disorder in the system. Assuming a simple system it can be related to the angle of the channels which lead through the material. Its mathematical definition is, as stated in [10], based on the definition by D. Johnson *et al.*:

$$\alpha_\infty = \frac{\frac{1}{V}\int_V v^2\, dV}{\left(\frac{1}{V}\int_V \vec{v}\, dV\right)^2}, \tag{2.9}$$

where V is the volume of an average pore inside the homogenisation domain and $\vec{v}$ is the velocity of fluid particles at high frequencies. It is a dimensionless quantity [11][10].

Viscous characteristic length Λ: Viscous characteristic length is a parameter introduced by D. Johnson *et al.*, describing the viscous effects in pores at medium and high frequencies. In most cases, it is the radius of the interconnections between the pores, except for small radii, where the viscous boundary layer has a larger impact on the airflow. Its mathematical definition is:

$$\Lambda = 2\frac{\int_V v^2_{\mathrm{M,inviscid}}\, \mathrm{d}V}{\int_A v^2_{\mu,\mathrm{inviscid}}\, \mathrm{d}A}, \tag{2.10}$$

where $v_{\mathrm{M,inviscid}}$ is the macroscopic velocity of the air in the pore and $v_{\mu,\mathrm{inviscid}}$ the microscopic velocity along the wall of the pores. A is the area of the pore interface and V the volume of the pore. Viscous characteristic length has the SI-unit metres [11][12].

Thermal characteristic length Λ': The definition of the thermal characteristic acoustic length is similar to that of the viscous characteristic length but describes the thermal effects at medium and high frequencies. It correlates to the largest radius of the pores.

Its mathematical definition is similar to that of its viscous counterpart, but without the weighting of velocities:

$$\Lambda' = 2\frac{\int_V \mathrm{d}V}{\int_A \mathrm{d}A}. \tag{2.11}$$

Again, A is the surface of the pore interface and V the volume of the pore. The SI unit of this parameter is metres [13]. Just as the open porosity, the thermal characteristic length is a purely geometrical parameter.

Static thermal permeability k_0': Static thermal permeability describes thermal effects at low frequencies. It is defined as:

$$k_0' = \lim_{\omega \to 0} k'(\omega), \tag{2.12}$$

where the dynamic thermal permeability $k'(\omega)$ is defined as:

$$\phi\tau = \frac{k'(\omega)}{\kappa}\frac{\partial p}{\partial t}. \tag{2.13}$$

In this equation, ϕ is the open porosity, τ the excess temperature as a function of the changing pressure over time $\partial p/\partial t$ and κ the thermal conductivity of air. This can be interpreted as the thermal equivalent to *Darcy's Law*, seen in Equation 2.8 [14] [15].

Static viscous and thermal tortuosity: The material parameters static viscous and thermal tortuosity are the low-frequency limits of their dynamic counterparts. The definitions of the dynamic tortuosities are:

$$\frac{\alpha(\omega)}{\alpha_\infty} = \frac{k_0}{k(\omega)}\frac{\omega_\mathrm{c}}{\mathrm{j}\omega}, \tag{2.14}$$

$$\alpha'(\omega) = \frac{k_0'}{k'(\omega)}\frac{\omega_\mathrm{c}'}{\mathrm{j}\omega}. \tag{2.15}$$

The frequencies ω_c and ω_c' are transition frequencies [16].

Transition frequencies: In the viscous case, $\omega_\mathrm{c} = \frac{\eta\Phi}{\alpha_\infty k_0 \bar{\rho}}$ is the critical frequency between the viscous and inertia dominated regions. $\bar{\rho}$ is the fluid density at rest. For the thermal case, $\omega_\mathrm{c}' = \frac{\lambda\phi}{\bar{\rho} c_\mathrm{p} k_0{}'}$ is defined as the characteristic thermal frequency, where c_p is the isobaric heat capacity of the fluid [16].

2.1.2.2 Fluid phase models

Delany-Bazley: The Delany-Bazley model is an empirical model which uses the static flow resistivity σ as its only parameter. Delany and Bazley measured the complex wavenumber k and the characteristic impedance Z_C for many fibrous materials (various grades of glass-fibre and mineral-wool materials [17]) with porosity close to 1 for a large range of frequencies. From these measurements it was concluded that k and Z_C mainly depend on the frequency f and the flow resistivity σ of the material. Delany and Bazley found the following expressions to give a good fit to the measured values [2]:

$$Z_{\mathrm{C}} = \rho_0 c_0 \left[1 + 0.057X^{-0.754} - \mathrm{j}0.087X^{-0.732}\right], \tag{2.16}$$

$$k = \frac{\omega}{c_0}\left[1 + 0.0978X^{-0.700} - \mathrm{j}0.189X^{-0.595}\right], \tag{2.17}$$

where ρ_0 is the density of air and c_0 the speed of sound in air, with the angular frequency $\omega = 2\pi f$ and

$$X = \frac{\rho_0 f}{\sigma}. \tag{2.18}$$

Delany and Bazley suggested their laws to be valid within

$$0.01 < X < 1.0. \tag{2.19}$$

According to [2], "[it] may not be expected that single relations provide a perfect prediction of acoustic behaviour of all the porous materials in the frequency range defined by Equation [2.19]. [...] Nevertheless, the laws of Delany and Bazley are widely used and can provide reasonable orders of magnitude for Z_{C} and k." It is to be noted here that for fibrous materials, which are anisotropic, the flow resistivity is different in normal and planar direction of the material [2].

Delany-Bazley-Miki: The Delany-Bazley-Miki model is an attempt to correct an error where the real part of the impedance would turn negative for low frequencies. Miki revised the regression model, resulting in a new set of constants:

$$Z_{\mathrm{C}} = \left[1 + 0.070\left(\frac{f}{\sigma}\right)^{-0.632} - \mathrm{j}0.107\left(\frac{f}{\sigma}\right)^{-0.632}\right], \tag{2.20}$$

$$k = \frac{\omega}{c_0}\left[0.160\left(\frac{f}{\sigma}\right)^{-0.618} - \mathrm{j}\left(1 + 0.109\left(\frac{f}{\sigma}\right)^{-0.618}\right)\right]. \tag{2.21}$$

The revised model gives better results in the entire frequency range, especially for lower frequencies. Miki did not set a new limit for which the model was accurate and should not formally be assumed to work outside the previously stated limits in Equation 2.19 [18].

Miki: Alongside the previous method, Miki suggested a generalisation of the empirical methods, allowing accurate prediction for materials were the porosity ϕ of the material is not unity. The model also allows for changes in tortuosity α_∞. Miki defined these parameters as $\phi = NA\alpha_\infty$ and $\alpha_\infty = 1/\cos\theta$, where N is the number of pores per unit area, A the area of each pore opening (assuming each pore to be a tube) and θ the angle of the pore which leads through the material. This is presented in Figure 2.1. The resulting mathematical representation becomes:

$$Z_{\mathrm{C}} = \frac{\alpha_\infty}{\phi}\left[1 + 0.070\left(\frac{f}{\sigma}\right)^{-0.632} - \mathrm{j}0.107\left(\frac{f}{\sigma}\right)^{-0.632}\right], \tag{2.22}$$

$$k = \frac{\alpha_\infty \omega}{c_0}\left[0.160\left(\frac{f}{\sigma}\right)^{-0.618} - \mathrm{j}\left(1 + 0.109\left(\frac{f}{\sigma}\right)^{-0.618}\right)\right]. \tag{2.23}$$

Note that while the parameters α_∞ and ϕ are not defined as in Section 2.1.2.1, they are both using the assumptions mentioned above [19].

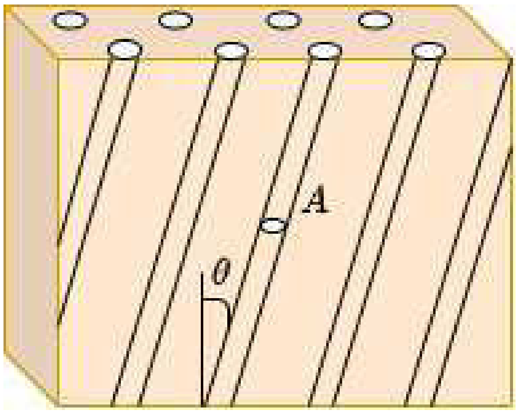

Figure 2.1: Figure of assumptions for the Miki model.

JCA: The Johnson-Champoux-Allard model describes the visco-inertial dissipative effects in porous materials. It is based on the work of D. Johnson *et al.*, describing the complex density of a motionless skeleton with arbitrary pore shapes. To do this, the authors defined the parameters viscous characteristic length Λ, as well as an expression for the dynamic tortuosity described in Section 2.1.2.1. The resulting equation for the complex density is [11][20]:

$$\tilde{\rho}(\omega) = \frac{\alpha_\infty \rho_0}{\phi}\left[1 + \frac{\sigma\phi}{\mathrm{j}\omega\rho_0\alpha_\infty}\sqrt{1 + \frac{4\alpha_\infty^2 \eta\rho_0\omega}{\sigma^2\Lambda^2\phi^2}}\right]. \tag{2.24}$$

Based on this, Y. Champoux and J. Allard derived an expression for the dynamic bulk modulus:

$$\tilde{K}(\omega) = \frac{\gamma P_0/\phi}{\gamma - (\gamma - 1)\left[1 - \mathrm{j}\frac{8\kappa}{\Lambda'^2 C_\mathrm{p}\rho_0\omega}\sqrt{1 + \mathrm{j}\frac{\Lambda'^2 C_\mathrm{p}\rho_0\omega}{16\kappa}}\right]^{-1}}. \tag{2.25}$$

In creating this method, the authors defined the thermal characteristic length Λ' (see Section 2.1.2.1) [13].
When the complex density and bulk modulus is know, the characteristic impedance and wavenumber can be calculated using Equations 2.44 and 2.45.

JCAL: The JCAL model is a continuation of the JCA model by D. Lafarge *et al.*, who recognised that there is a loss of information concerning the thermal permeability in the description of the bulk modulus at low frequencies. To tackle this issue, the group introduced the static thermal permeability k_0', defined as the low-frequency limit of the dynamic thermal permeability, resulting in the following expression:

$$\tilde{K}(\omega) = \frac{\gamma P_0/\phi}{\gamma - (\gamma - 1)\left[1 - \mathrm{j}\frac{\phi\kappa}{k_0' C_\mathrm{p}\rho_0\omega}\sqrt{1 + \mathrm{j}\frac{4k_0' C_\mathrm{p}\rho_0\omega}{\kappa\Lambda'^2\phi}}\right]^{-1}}. \tag{2.26}$$

The expression for the complex density remains the same, resulting in a total of five required material parameters [15][21].

JCAPL: The JCAPL model is a further extension of the JCA model by S. Pride. The model takes drag effects acting in the fluid due to changing pore sizes into account. These are assumed to vary with a certain periodicity, which is much shorter than the sound wavelength. This effect is represented as static viscous tortuosity α_0 and static thermal tortuosity α'_0, representing the thermal and mechanical effects of non-periodic or low frequent flow passing through the material. It resulted in a series of expressions for both the complex density and bulk modulus, after correction by D. Lafarge [22] [23]:

$$\tilde{\rho} = \frac{\rho_0 \tilde{\alpha}(\omega)}{\phi} \tag{2.27}$$

$$\tilde{\alpha} = \alpha_\infty \left[1 + \frac{1}{\mathrm{j}\omega} \tilde{F}(\omega)\right] \tag{2.28}$$

$$\tilde{F}(\omega) = 1 - P + P\sqrt{1 + \frac{M}{2P^2}\mathrm{j}\bar{\omega}} \tag{2.29}$$

$$\bar{\omega} = \frac{\omega \rho_0 k_0 \alpha_\infty}{\eta \phi} \tag{2.30}$$

$$M = \frac{8 k_0 \alpha_\infty}{\phi \Lambda^2} \tag{2.31}$$

$$P = \frac{M}{4\left(\frac{\alpha_0}{\alpha_\infty} - 1\right)} \tag{2.32}$$

$$\tilde{K}(\omega) = \frac{\gamma P_0}{\phi} \frac{1}{\tilde{\beta}(\omega)} \tag{2.33}$$

$$\tilde{\beta}(\omega) = \gamma - (\gamma - 1)\left[1 + \frac{1}{\mathrm{j}\bar{\omega}'} \tilde{F}'(\omega)\right]^{-1} \tag{2.34}$$

$$\tilde{F}'(\omega) = 1 - P' + P'\sqrt{1 + \frac{M'}{2P'^2}\mathrm{j}\bar{\omega}'} \tag{2.35}$$

$$\bar{\omega}' = \frac{\omega \rho_0 k'_0 C_\mathrm{p}}{\kappa \phi} \tag{2.36}$$

$$M' = \frac{8 k'_0}{\phi \Lambda'^2} \tag{2.37}$$

$$P' = \frac{M'}{4(\alpha'_0 - 1)} \tag{2.38}$$

2.1.2.3 Model for material compression

When a porous absorber is compressed, the flow characteristics of the material change, which is shown in Figure 2.2. The pore-openings are squeezed, resulting in a lower porosity. The tortuosity becomes higher as the same channel lengths need to fit into a thinner material. For similar reasons, the characteristic lengths become shorter, while a higher resistivity is generated as a result of the denser material. By measuring the structural changes using ultrasound, B. Castagnède *et al.* [24] found a rather simple relation between the changes in the material parameters and the compression rate $n = h_0/h$, where h_0 is the initial thickness of the material and h the current thickness.

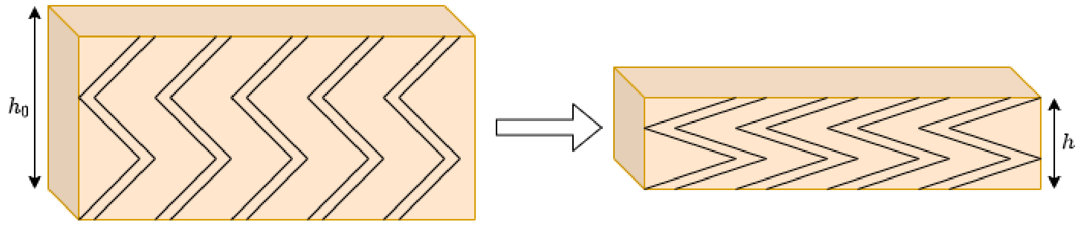

Figure 2.2: Compression of the material leads to geometrical changes of the pores/air-channels.

Static air flow resistivity σ:

$$\sigma_n = n\sigma_{(0)} \tag{2.39}$$

Open porosity ϕ:

$$\Phi^{(n)} = 1 - n(1 - \Phi^{(0)}) \tag{2.40}$$

High frequency limit of tortuosity α_∞:

$$\alpha_\infty^{(n)} = 1 - n(1 - \alpha_\infty^{(0)}) \tag{2.41}$$

Viscous characteristic length Λ:

$$\Lambda_{(n)} = \frac{\Lambda_{(0)}}{\sqrt{n}} + \frac{a}{2}\left(\frac{1}{\sqrt{n}} - 1\right) \tag{2.42}$$

Thermal characteristic length Λ':

$$\Lambda'_{(n)} = \frac{\Lambda'_{(0)}}{\sqrt{n}} + \left[\frac{a}{2}\left(\frac{1}{\sqrt{n}} - 1\right)\right] \tag{2.43}$$

In Equations 2.42 and 2.43 a is the mean diameter of the material fibres. Since $[\Lambda, \Lambda'] >> a$, the first term is sufficient for most cases [24].

2.1.2.4 Impedance and wavenumber for equivalent fluid models

The characteristic impedance Z_C and complex wavenumber k of a porous material are related to the equivalent dynamic density and bulk modulus as: [2]

$$Z_\mathrm{C} = \sqrt{\tilde{K}\tilde{\rho}}, \tag{2.44}$$

$$k = \omega\sqrt{\frac{\tilde{\rho}}{\tilde{K}}}. \tag{2.45}$$

Analogously, the expressions given by some models for the characteristic impedance and complex wavenumber can be converted into equivalent dynamic densities and bulk moduli. These expressions are valid for *equivalent fluid* models.
For simple cases, such as a single layer of porous material with a motionless skeleton backed by an impervious rigid wall excited by an incident plane wave sound field,

the surface impedance can be calculated directly from the characteristic impedance, giving the reflection factor and absorption coefficient [2]. For more complicated scenarios, such as multi-layer configurations, and when taking the elastic properties of the skeleton into account, it is required to use more sophisticated approaches based on *Biot's theory* which is introduced in Section 2.1.3.

2.1.2.5 Perforated plate and fluid phase models

In [25] N. Atalla and F. Sgard describe the classical models of airflow through a perforated rigid surface in terms of the fluid phase parameters. Using the JCA model, the flow resistivity, tortuosity and viscous and thermal characteristic lengths are expressed in terms of the perforation radius r and the perforation rate ϕ. Similarly to the model created by Miki (see Section 2.1.2.2), the channels are assumed to be uniform cylinders. Due to the uniformity, the viscous and thermal characteristic lengths remain the same as the radius of the cylinder:

$$\Lambda = \Lambda' = r. \tag{2.46}$$

The flow resistivity σ can be obtained from the perforation radius r and the open porosity (= perforation rate) ϕ as

$$\sigma = \frac{8\eta}{\phi r^2}, \tag{2.47}$$

where η is the dynamic viscosity of air. The effect of the tortuosity is represented by the effective density:

$$\tilde{\rho} = \rho_0 \tilde{\alpha}, \tag{2.48}$$

where $\tilde{\alpha}$ is the dynamic tortuosity.

Assuming the perforated plate to be backed by a semi-infinite air medium with an impedance of Z_B, the surface impedance can be calculated as:

$$Z_{\mathrm{A}'} = \mathrm{j}\omega\tilde{\rho}_{\mathrm{e}} d + \phi Z_{\mathrm{B}}, \tag{2.49}$$

$$\tilde{\rho}_{\mathrm{e}} = \rho_0 \alpha_\infty \left(1 + \frac{\sigma\phi}{\mathrm{j}\omega\rho_0\alpha_\infty} G_{\mathrm{j}}(\omega)\right), \tag{2.50}$$

$$G_{\mathrm{j}}(\omega) = \left(1 + 4\mathrm{j}\frac{\omega\rho_0\alpha_\infty^2\eta}{\sigma^2\phi^2\Lambda^2}\right)^{1/2}. \tag{2.51}$$

For this model to work in more complicated cases, such as against a porous backing, a set of correction terms needs to be applied. Details about this can be found in [25]. This way of describing a material is similar to the transfer-matrix-model discussed in Section 2.2. In fact, it is in that context that this perforated plate model is most commonly used.

2.1.3 Diphasic models (*Biot's theory*)

So far, the sound propagation in porous media has been described taking into account effects in the fluid phase only. These models can provide a sufficiently accurate description when the material skeleton is rather rigid and bonded onto a non-vibrating surface and can thus be considered motionless. However, in the general case of elastic materials, and especially in multi-layer configurations, it becomes necessary to additionally take the elastic properties of the solid phase into account. This is possible by the use of *Biot's theory* (after M. Biot), which describes the coupling between the fluid and the solid phase. Thus, additionally to the previously described dissipations in the fluid phase, it also allows for a description of the dissipations in the solid phase. Further, there are introduced two additional waves. While the *equivalent fluid* models only describe one compressional wave, taking the skeleton into account introduces one additional compressional wave and a shear wave, propagating (mainly) in the skeleton [2].

In the following, Biot's original model is introduced first. Then a more recent formulation of *Biot's theory* is presented, which allows for coupling different fluid phase models to different solid-phase models.

2.1.3.1 Biot's original model

The main assumptions used in the derivation of *Biot's theory* are [2]:

- The dissipation in the fluid phase (visco-inertial dissipation) is independent of the dissipation in the solid phase (structural losses). This allows the separate description of both dissipations. Biot's original theory includes viscous effects using a tortuosity factor and neglects thermo-dynamical dissipation.
- The phases are continuous, i.e. only connected pores are considered, and the fluid fully saturates the pore volumes. Pores which are encapsulated by the skeleton are considered parts of the skeleton.
- The standard deviation of the pore size distribution is low, so that a mean pore size value can be used with good accuracy.
- The mean pore size is small compared to the wavelengths in the fluid and the frame.
- The medium is isotropic, so it may be considered as homogeneous on a macroscopic scale.

Under these assumptions, *Biot's theory* relates stresses and strains in the material and the fluid with [2][26]:

$$\underline{\underline{\sigma}}^{\mathrm{s}}(\underline{u},\underline{U}) = \left[(\tilde{P}-2N)\nabla\cdot\underline{u} + \tilde{Q}\nabla\cdot\underline{U}\right]\underline{\underline{1}} + 2N\underline{\underline{\epsilon}}^{\mathrm{s}}, \tag{2.52}$$

$$\underline{\underline{\sigma}}^{\mathrm{f}}(\underline{u},\underline{U}) = (-\phi p)\underline{\underline{1}} = (\tilde{Q}\nabla\cdot\underline{u} + \tilde{R}\nabla\cdot\underline{U})\underline{\underline{1}}. \tag{2.53}$$

In these equations, ∇ is the nabla operator[1], $\underline{u}$ and $\underline{U}$ are the displacement vectors in the solid and the fluid, $\underline{\underline{\sigma}}^{\mathrm{s}}$ and $\underline{\underline{\sigma}}^{\mathrm{f}}$ are the stress tensors in the solid and the fluid, $\underline{\underline{\epsilon}}^{\mathrm{s}}$ and $\underline{\underline{\epsilon}}^{\mathrm{f}}$ are the strain tensors, $\nabla\cdot\underline{u}$ and $\nabla\cdot\underline{U}$ are the dilatations of the solid and the fluid and $\underline{\underline{1}}$ is the identity tensor. The tilde symbol indicates that the associated physical property is complex (including damping) and frequency dependent. The terminology used here writes vectors and matrices as $\underline{()}$ and $\underline{\underline{()}}$ respectively, indicating the number of dimensions.

[1] To avoid confusion, $\nabla\cdot$ indicates the divergence and ∇ the gradient.

The coefficient $\tilde{Q}$ couples the solid and the fluid. The term $\tilde{Q}\nabla\cdot\underline{U}$ gives the contribution of the air dilatation to the stress in the frame and $\tilde{Q}\nabla\cdot\underline{u}$ gives the contribution of the frame dilatation to the pressure variation in the air. With $\tilde{Q}=0$, Equation 2.52 becomes the stress-strain relation in elastic solids and Equation 2.53 becomes the stress-strain relation in elastic fluids [2]. $\tilde{R}$ may be interpreted as the bulk modulus of the fluid occupying a fraction ϕ of a unit volume of the material. It is related to the bulk modulus $\tilde{K}_\mathrm{f}$ of the fluid in the pores with $\tilde{R}=\phi\tilde{K}_\mathrm{f}$. ϕ is the open porosity [26]. The elastic coefficients $\tilde{P}$, $\tilde{Q}$ and $\tilde{R}$ are given as [2]

$$\tilde{P} = \frac{(1-\phi)\left[1-\phi-\frac{K_\mathrm{b}}{K_\mathrm{s}}\right]K_\mathrm{s}+\phi\frac{K_\mathrm{s}}{\tilde{K}_\mathrm{f}}K_\mathrm{b}}{1-\phi-\frac{K_\mathrm{b}}{K_\mathrm{s}}+\phi\frac{K_\mathrm{s}}{\tilde{K}_\mathrm{f}}}+\frac{4}{3}N, \tag{2.54}$$

$$\tilde{Q} = \frac{\left[1-\phi-\frac{K_\mathrm{b}}{K_\mathrm{s}}\right]\phi K_\mathrm{s}}{1-\phi-\frac{K_\mathrm{b}}{K_\mathrm{s}}+\phi\frac{K_\mathrm{s}}{\tilde{K}_\mathrm{f}}}, \tag{2.55}$$

$$\tilde{R} = \frac{\phi^2 K_\mathrm{s}}{1-\phi-\frac{K_\mathrm{b}}{K_\mathrm{s}}+\phi\frac{K_\mathrm{s}}{\tilde{K}_\mathrm{f}}}. \tag{2.56}$$

The coefficient N is the complex *in vacuo* shear modulus of the skeleton (including losses)

$$N = \frac{E_\mathrm{s}(1+\mathrm{j}\eta_\mathrm{s})}{2(1+\nu_\mathrm{s})}, \tag{2.57}$$

where E_s is the Young's modulus, η_s the loss factor and ν_s the Poisson's ratio. K_s is the bulk modulus of the elastic solid from which the skeleton is made and K_b is the bulk modulus of the skeleton *in vacuo*, given by [2]

$$K_\mathrm{b} = \frac{2N(\nu_\mathrm{s}+1)}{3(1-2\nu_\mathrm{s})} \tag{2.58}$$

The elastic coefficients $\tilde{P}$, $\tilde{Q}$ and $\tilde{R}$ have a frequency dependent complex amplitude, since $\tilde{K}_\mathrm{f}$ takes thermal effects in the pore into account.

The wave equations in the original Biot model read as [2]

$$-\omega^2(\tilde{\rho}_{11}\underline{u}+\tilde{\rho}_{12}\underline{U}) = (\tilde{P}-N)\nabla\nabla\cdot\underline{u}+N\nabla^2\underline{u}+\tilde{Q}\nabla\nabla\cdot\underline{U} \tag{2.59}$$

$$-\omega^2(\tilde{\rho}_{22}\underline{U}+\tilde{\rho}_{12}\underline{u}) = \tilde{R}\nabla\nabla\cdot\underline{U}+\tilde{Q}\nabla\nabla\cdot\underline{u} \tag{2.60}$$

with

$$\tilde{\rho}_{11} = \rho_1+\rho_\mathrm{a}-\mathrm{j}\sigma\phi^2\frac{G(\omega)}{\omega}, \tag{2.61}$$

$$\tilde{\rho}_{12} = -\rho_\mathrm{a}+\mathrm{j}\sigma\phi^2\frac{G(\omega)}{\omega}, \tag{2.62}$$

$$\tilde{\rho}_{22} = \phi\rho_0+\rho_\mathrm{a}-\mathrm{j}\sigma\phi^2\frac{G(\omega)}{\omega} \tag{2.63}$$

and

$$\rho_\mathrm{a} = \phi\rho_0(\alpha_\infty-1). \tag{2.64}$$

In these equations, ρ_1 is the density of the solid, ρ_0 is the density of air, σ is the static air flow resistivity and $G(\omega)$ is an expression linked to the different fluid phase models.[2] Several alternative formulations of *Biot's theory* have been developed [2], one of which is presented in Section 2.1.3.3.

2.1.3.2 The two compressional waves and the shear wave

Biot's theory accounts for three different waves propagating in a porous medium, namely two compressional waves and a shear wave. One of the compressional waves propagates in the fluid and the other (mainly) in the solid. Therefore, the two compressional waves are also referred to as *frame-borne* wave and *airborne wave*. The wave propagating mostly in the fluid is also referred to as *slow wave* while the *fast wave* is the one propagating in both media. The shear wave propagates only in the frame [2].
For materials where the frame is much heavier and stiffer than the air, the phases can be considered partially decoupled. For materials where the stiffness of the frame is in the same order of magnitude as the one of air and the density is about ten times larger, this partial decoupling does not exist at low frequencies up until a phase decoupling frequency [2]

$$f_0 = \frac{1}{2\pi}\frac{\phi^2\sigma}{\rho_1}, \tag{2.65}$$

where ρ_1 is the density of the material, σ the flow resistivity and ϕ the open porosity. Above this frequency, the material skeleton can be considered as motionless.
The squared complex wave numbers δ_{n}^2 of the two compressional waves are [2]

$$\delta_1^2 = \frac{\omega^2}{2(\tilde{P}\tilde{R}-\tilde{Q}^2)}\left[\tilde{P}\tilde{\rho}_{22}+\tilde{R}\tilde{\rho}_{11}-2\tilde{Q}\tilde{\rho}_{12}-\sqrt{\Delta}\right] \tag{2.66}$$

$$\delta_2^2 = \frac{\omega^2}{2(\tilde{P}\tilde{R}-\tilde{Q}^2)}\left[\tilde{P}\tilde{\rho}_{22}+\tilde{R}\tilde{\rho}_{11}-2\tilde{Q}\tilde{\rho}_{12}+\sqrt{\Delta}\right] \tag{2.67}$$

with

$$\Delta = \left[\tilde{P}\tilde{\rho}_{22}+\tilde{R}\tilde{\rho}_{11}-2\tilde{Q}\tilde{\rho}_{12}\right]^2 - 4\left(\tilde{P}\tilde{R}-\tilde{Q}^2\right)\left(\tilde{\rho}_{11}\tilde{\rho}_{22}-\tilde{\rho}_{12}^2\right). \tag{2.68}$$

The squared wave number for the shear wave is [2]

$$\delta_3^2 = \frac{\omega^2}{N}\left(\frac{\tilde{\rho}_{11}\tilde{\rho}_{22}-\tilde{\rho}_{12}^2}{\tilde{\rho}_{22}}\right). \tag{2.69}$$

2.1.3.3 Alternative Biot's formulation

An alternative representation of *Biot's theory*, using the solid displacement $\underline{u}$ and the pressure in the fluid p instead of the couple $\underline{u}^{\mathrm{s}}$ and $\underline{u}^{\mathrm{f}}$, was presented by N. Atalla *et al.* in 1998 [26]. Without introducing new assumptions, using this representation the number of degrees of freedom in each point reduces from six to four (one pressure and

[2] In [2] the expression $G(\omega)$ is used to summarise the different fluid phase models introduced in Section 2.1.2.2. It contains the expressions for the equivalent dynamic mass density and bulk modulus which have been presented earlier.

three frame displacements). This is of particular interest for numerical implementations due to the decreased computational effort [27]. The formulation of N. Atalla *et al.* was modified by F. Bécot and L. Jaouen [28] to directly include the equivalent dynamic density $\tilde{\rho}_{eq}$ and bulk modulus $\tilde{K}_{eq}$ for describing the dissipation in the fluid phase. The expressions for these can be obtained from the existing *equivalent fluid* models. This allows for choosing the model for the fluid phase based on the available material data.

The wave equations in this formulation read as [28][26]:

$$\nabla \cdot \underline{\underline{\hat{\sigma}}}^{s}(\underline{u}) + \omega^2 \tilde{\rho} \underline{u} = -\tilde{\gamma} \underline{\nabla} p, \tag{2.70}$$

$$\nabla^2 p + \frac{\tilde{\rho}_{22}}{\tilde{R}} \omega^2 p = \frac{\tilde{\rho}_{22}}{\phi^2} \tilde{\gamma} \omega^2 \nabla \cdot \underline{u}, \tag{2.71}$$

where $\underline{\underline{\hat{\sigma}}}^{s}(\underline{u})$ is the *in vacuo* stress tensor. The first equation is the structure equation where the left-hand side describes the elastodynamic behaviour of the skeleton *in vacuo*. The source-term on the right-hand side describes the force created by the pressure in the fluid, acting on the skeleton. The second equation is the fluid equation. Here the left-hand side is an equivalent Helmholtz equation for the fluid, when the frame is supposed motionless, and the source-term on the right-hand side describes the displacement of the skeleton, acting on the fluid. From this, it becomes clear that the terms on the right-hand side of the equations (including the coupling factor $\tilde{\gamma}$) are coupling terms, which couple the displacement of the skeleton to the pressure in the fluid. The coupling is of volume nature (note that the unit of the terms is $\mathrm{N/m^3}$). The variables in Equations 2.70 and 2.71 are given as [28]

$$\tilde{\rho} = \rho_1 + \phi \rho_0 - \frac{\rho_0^2}{\tilde{\rho}_{eq}} \tag{2.72}$$

$$\tilde{\gamma} = \frac{\rho_0}{\tilde{\rho}_{eq}} - 1 + \frac{K_b}{K_s} \tag{2.73}$$

$$\tilde{\rho}_{22} = \phi^2 \tilde{\rho}_{eq} \tag{2.74}$$

$$\tilde{R} = \frac{\phi^2 K_s}{\tilde{D}} \tag{2.75}$$

$$\tag{2.76}$$

with

$$\rho_1 = (1-\phi)\rho_s \tag{2.77}$$

$$\tilde{D} = 1 - \phi - \frac{K_b}{K_s} + \frac{K_s}{\tilde{K}_{eq}}. \tag{2.78}$$

In these equations, K_b is the bulk modulus of the skeleton at constant pressure in air, K_s is the bulk modulus of the elastic material from which the skeleton is made, ρ_0 is the density of air at rest and ρ_s is the density of the material from which the skeleton is made. The coefficients $\tilde{Q}$, $\tilde{R}$ and $\tilde{D}$ are related to the coupling between the elastic effects and the fluid properties, while the modified Biot's densities $\tilde{\rho}$ and $\tilde{\rho}_{22}$ depend only on the properties of the fluid phase and the pore geometry. The *equivalent fluid* expressions $\tilde{\rho}_{eq}$ and $\tilde{K}_{eq}$ describe the dissipation in the fluid, where $\tilde{\rho}_{eq}$ is associated with visco-inertial effects and $\tilde{K}_{eq}$ is associated with thermal effects.

2.1.3.4 Reduced formulations

There are several approaches for reducing the complexity and numerical effort of calculations.
For a rigid and motionless frame, the wave propagation in the porous medium can be described solely with Equation 2.71, where the source term on the right-hand side is set to zero. Additionally making the approximations $\phi \approx 1$ and $K_\mathrm{b} \ll K_\mathrm{s}$ gives

$$\nabla^2 p + \frac{\tilde{\rho}_\mathrm{eq}}{\tilde{K}_\mathrm{eq}} \omega^2 p = 0, \tag{2.79}$$

which can be identified as the classical Helmholtz equation for sound propagation in a dissipative fluid. As the frame is assumed rigid and motionless, it does not participate in the dissipation and its elastic properties do not influence the wave propagation (under the above-mentioned approximations). The propagation of sound in the porous medium can then be fully described by a characteristic impedance $Z_\mathrm{c} = \sqrt{\tilde{\rho}_\mathrm{eq} \tilde{K}_\mathrm{eq}}$ and wavenumber $k_\mathrm{c} = \omega \sqrt{\frac{\tilde{\rho}_\mathrm{eq}}{\tilde{K}_\mathrm{eq}}}$. This is commonly referred to as *equivalent fluid* approach [28]. It may be used for acoustically excited, very heavy and stiff skeleton materials bonded onto a non-vibrating surface [27].
Two less restricted asymptotic simplifications are the *rigid body* and the *limp* hypotheses. These are termed *equivalent fluid* approaches as well because the elastic behaviour is included in modified equivalent dynamic mass densities. The *rigid body* hypothesis assumes that the frame does not deform but can move in rigid body motion. This may occur for very stiff materials with a low density. It can be expressed by a modified equivalent dynamic density [28]. The *limp* hypothesis assumes that the material has no stiffness, i.e. the bulk modulus K_b and shear modulus N are assumed to be zero. This corresponds to soft fibrous materials with high porosity. This case can be expressed by [28]

$$\frac{1}{\tilde{\rho}_\mathrm{eq}^\mathrm{limp}} = \frac{1}{\phi \tilde{\rho}_\mathrm{eq}} + \frac{\gamma^2}{\phi \tilde{\rho}}. \tag{2.80}$$

This model may be used for porous materials which are not directly coupled to a vibrating structure. It may be noted that for $\phi \approx 1$, which is mostly the case for porous absorbers, $\tilde{\rho}_\mathrm{eq}^\mathrm{RB} = \tilde{\rho}_\mathrm{eq}^\mathrm{limp}$. The important difference of these approaches to the motionless skeleton model is that inertial and damping effects in the solid phase are not neglected. The great advantage of these *equivalent fluid* approaches to the full $(\underline{u}, p)$ formulation (Equations 2.70 and 2.71) is that the number of degrees of freedom reduces from four to one (only the pressure is left), which reduces the computational effort (especially important in FEM modelling).

2.2 Modelling of multilayered systems with porous materials using the transfer-matrix-method

The transfer-matrix-method (TMM) is a method used widely in physics to determine how potential fields are changed through different mediums. It allows the characteristics of multiple layers of mediums to be condensed in a single transfer matrix. While

the complexity of the matrix differs greatly depending on which material model is used, the principle is the same.
The modelling of porous materials with TMM can be based on *equivalent fluid* approaches (then the approach is the same as for a regular fluid) or *Biot's theory.*

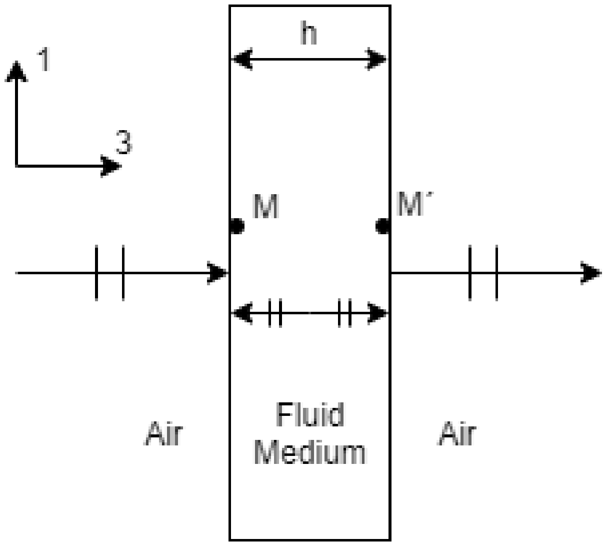

Figure 2.3: Representation of the transfer-matrix-method for a single material in a 2D model.

2.2.1 Fluids

Assuming a fluid model and a plane wave with orthogonal incidence, the model becomes quite simple. A visualisation of the model can be seen in Figure 2.3. Since it is a fluid medium, the wave propagation can be described in terms of pressure and velocity, which in each position corresponds to:

$$p(x_3) = A_\mathrm{i}\mathrm{e}^{-\mathrm{j}k_3x_3} + A_\mathrm{r}\mathrm{e}^{\mathrm{j}k_3x_3}, \tag{2.81}$$

$$v_3^\mathrm{f}(x) = \frac{k}{\rho\omega}\left[A_\mathrm{i}\mathrm{e}^{-\mathrm{j}k_3x_3} - A_\mathrm{r}\mathrm{e}^{\mathrm{j}k_3x_3}\right], \tag{2.82}$$

where A_i and A_r are the two unknown amplitudes of the incident and reflective waves respectively. k_3 is the complex wavenumber calculated from the fluid phase model in incident direction. The state vector for the two positions is defined as:

$$\underline{V}^\mathrm{f}(M) = \begin{bmatrix} p(M) & v^\mathrm{f}(M) \end{bmatrix}^\mathrm{T}.$$

By setting $x = 0$ for position M' and $x = -h$ for M, expressions for the two boundary states can be set. The transfer matrix is then defined as:

$$\underline{V}^\mathrm{f}(M') = \underline{\underline{T}} \cdot \underline{V}^\mathrm{f}(M), \tag{2.83}$$

resulting in the transfer matrix

$$\underline{\underline{T}} = \begin{bmatrix} \cos kh & \mathrm{j}\frac{\omega\rho}{k}\sin kh \\ \mathrm{j}\frac{k}{\omega\rho}\sin kh & \cos kh \end{bmatrix}.$$

2.2.2 Elastic solids

In the case of an elastic solid, there are two kinds of waves: Longitudinal and shear waves. Just as in the fluid case, the boundary states are calculated using both the incident and reflected wave, totalling in four waves that describe the acoustic field in the medium. The state vector for the solid medium consists of four states:

$$\underline{V}^2(M) = \left[v_1^s(M) \quad v_3^s(M) \quad \sigma_{33}^s(M) \quad \sigma_{31}^s(M) \right]^T$$

where $v_1^s(M)$ is the velocity in the radial direction and $v_3^s(M)$ the velocity through the medium, which are all derived from longitudinal and shear waves. $\sigma_{33}^s(M)$ and $\sigma_{31}^s(M)$ are the normal and tangential stresses at position M, resulting in a 4×4 transfer matrix. While the concept of solving Equation 2.83 is the same, the solution becomes much more complicated. The complete derivation is presented by J. Allard and N. Attala in [2].

2.2.3 Poroelastic materials

Looking at a poroelastic medium, the model becomes even more intricate. The acoustic field can be described by one structural and one fluid compressional wave, as well as one structural shear wave. Just as the for the solid medium, the state vector for position M contains velocity in radial and normal direction as well as the normal and tangential stresses in the structure. This is combined with the fluid, resulting in two more states: The fluid velocity $v_3^f(M)$ in the normal direction and the normal stress tensor $\sigma_{33}^f(M)$ in the fluid [2]

$$\underline{V}^p(M) = \left[v_1^s(M) \quad v_3^s(M) \quad v_3^f(M) \quad \sigma_{33}^s(M) \quad \sigma_{31}^s(M) \quad \sigma_{33}^f(M) \right]^T .$$

2.2.4 Multiple layers

The TMM can be extrapolated for multiple layers, since each layer only adds one unknown parameter as well as one equation, generating a single transfer matrix

$$\underline{V}^{\mathrm{f}}(M'_{\mathrm{n}}) = \underline{\underline{T}} \cdot \underline{V}^{\mathrm{f}}(M_0), \tag{2.84}$$

where $\underline{\underline{T}} = \underline{\underline{T_1 T_2 ... T_n}}$. If there is an interface of layers of different nature, such as an elastic solid layer on a fluid layer, the continuity is ensured by an interface matrix. A detailed derivation can be found in [2].
An approach that improves the numerical stability of the computation has been presented by O. Dazel *et al.* [29].[3]

2.3 Finite element modelling of poroelastic materials

FEM modelling of poroelastic materials is based on either simple impedance techniques, *equivalent fluid* approaches or *Biot's theory*. For multi-layered systems containing porous media, it is generally necessary to use the more sophisticated approaches

[3] This is the approach used in AlphaCell from version 11.0 on.

based on *Biot's theory* [26]. In finite-element implementations the mixed displacement-pressure formulation (Equations 2.70 and 2.71) is preferred over Biot's original formulation (Equations 2.59 and 2.60). This reduces the computational effort, since the number of degrees of freedom per node reduces from six to four (accounting for three displacement components of the solid phase and the pressure of the fluid phase). Further advantages are that the stiffness matrix associated with the solid phase does not depend on the frequency and that the coupling to acoustic and other poroelastic media is handled naturally, without essential boundary conditions [26].

2.3.1 Weak integral formulation

The finite element implementation of *Biot's theory* is based on the weak integral formulation of Equations 2.70 and 2.71 [26] [30]:

$$\begin{aligned}\int_\Omega \underline{\underline{\hat{\sigma}}}^{\mathrm{s}}(\underline{u}) : \underline{\underline{\epsilon}}^{\mathrm{s}}(\delta\underline{u})\,\mathrm{d}\Omega - \omega^2 \int_\Omega \tilde{\rho}\underline{u}\cdot\delta\underline{u}\,\mathrm{d}\Omega - \int_\Omega \tilde{\gamma}\underline{\nabla}p\cdot\delta\underline{u}\,\mathrm{d}\Omega \\ - \int_\Gamma [\underline{\underline{\hat{\sigma}}}^{\mathrm{s}}\cdot\underline{n}]\cdot\delta\underline{u}\,\mathrm{d}S = 0\ \forall(\delta\underline{u}),\end{aligned} \tag{2.85}$$

$$\begin{aligned}\int_\Omega \left[\frac{\phi^2}{\omega^2\tilde{\rho}_{22}}\underline{\nabla}p\cdot\underline{\nabla}\delta p - \frac{\phi^2}{\tilde{R}}p\,\delta p\right]\mathrm{d}\Omega - \int_\Omega \tilde{\gamma}\underline{\nabla}\delta p\cdot\underline{u}\,\mathrm{d}\Omega \\ + \int_\Gamma \left[\tilde{\gamma}u_{\mathrm{n}} - \frac{\phi^2}{\tilde{\rho}_{22}\omega^2}\frac{\partial p}{\partial n}\right]\delta p\,\mathrm{d}S = 0\ \forall(\delta p),\end{aligned} \tag{2.86}$$

where Ω and Γ refer to the poroelastic domain and its boundary surface. The admissible variations of the solid phase displacement vector $\underline{u}$ and the interstitial fluid pressure p are denoted $\delta\underline{u}$ and δp. Subscript n denotes the normal component of a vector and $\underline{n}$ is the unit external normal vector of the boundary surface Γ. $\underline{\underline{\epsilon}}^{\mathrm{s}}$ is the strain tensor of the solid phase.
In order to apply boundary conditions, it is instructive to rewrite Equations 2.85 and 2.86 as boundary integrals. The boundary integral of the solid phase is given as [30]

$$I_1 = -\int_\Gamma (\underline{\underline{\sigma}}^t\cdot\underline{n})\cdot\delta\underline{u}\,\mathrm{d}S - \int_\Gamma \phi\left(1+\frac{\tilde{Q}}{\tilde{R}}\right)p\,\delta u_{\mathrm{n}}\,\mathrm{d}S, \tag{2.87}$$

where $\tilde{Q}$ and $\tilde{R}$ are given by Equations 2.55 and 2.56 and $\underline{\underline{\sigma}}^t$ is the total stress tensor of the material (fluid and solid). This integral represents the work done on the solid phase by external forces.
The boundary integral of the fluid phase is given as [30]

$$I_2 = -\int_\Gamma \phi\left(1+\frac{\tilde{Q}}{\tilde{R}}\right)u_{\mathrm{n}}\delta p\,\mathrm{d}S - \int_\Gamma \phi(U_{\mathrm{n}} - u_{\mathrm{n}})\delta p\,\mathrm{d}S, \tag{2.88}$$

where U_{n} is the fluid phase displacement vector, which is related to the pressure gradient with [26]

$$\underline{U} = \frac{\phi}{\tilde{\rho}_{22}\omega^2}\underline{\nabla}p - \frac{\tilde{\rho}_{12}}{\tilde{\rho}_{22}}\underline{u}. \tag{2.89}$$

This integral represents the work done on the fluid phase by external forces. A detailed description of the boundary conditions that apply for different kinds of excitation, support and coupling is given in [30].

2.3.2 Numerical implementation

It is assumed that within a finite element the solid phase displacement vector and the pressure can be represented in matrix form as

$$\begin{aligned} \underline{u}^e &= [N_\mathrm{s}]\{u_\mathrm{n}\}^e, \\ p^e &= [N_\mathrm{f}]\{p_\mathrm{n}\}^e, \end{aligned} \tag{2.90}$$

where $[N_\mathrm{s}]$ and $[N_\mathrm{f}]$ are the shape-functions of element "e", used to approximate the solid-phase displacement vector and interstitial pressure, and $\{u_\mathrm{n}\}^e$ and $\{p_\mathrm{n}\}^e$ are the nodal displacement and pressure variables. Inserting this into Equations 2.85 and 2.86 gives [26]

$$\int_\Omega \underline{\underline{\hat{\sigma}}}^\mathrm{s}(\underline{u}) : \underline{\underline{\epsilon}}^\mathrm{s}(\delta \underline{u})\,\mathrm{d}\Omega \Rightarrow \langle \delta u_\mathrm{n} \rangle\,[K]\{u_\mathrm{n}\} \tag{2.91}$$

$$\int_\Omega \tilde{\rho}\underline{u} \cdot \delta \underline{u}\,\mathrm{d}\Omega \Rightarrow \langle \delta u_\mathrm{n} \rangle\,[\tilde{M}]\{u_\mathrm{n}\} \tag{2.92}$$

$$\int_\Omega \tilde{\gamma}\underline{\nabla} p \cdot \delta \underline{u}\,\mathrm{d}S \Rightarrow \langle \delta u_\mathrm{n} \rangle\,[\tilde{C}]\{p_\mathrm{n}\} \tag{2.93}$$

and

$$\int_\Omega \frac{\phi^2}{\tilde{\rho}_{22}}\underline{\nabla} p \cdot \underline{\nabla} \delta p\,\mathrm{d}\Omega \Rightarrow \langle \delta p_\mathrm{n} \rangle\,[\tilde{H}]\{p_\mathrm{n}\} \tag{2.94}$$

$$\int_\Omega \frac{\phi^2}{\tilde{R}} p\,\delta p\,\mathrm{d}\Omega \Rightarrow \langle \delta p_\mathrm{n} \rangle\,[\tilde{Q}]\{p_\mathrm{n}\} \tag{2.95}$$

$$\int_\Omega \tilde{\gamma}\underline{\nabla} \delta p \cdot \underline{u}\,\mathrm{d}S \Rightarrow \langle \delta p_\mathrm{n} \rangle\,[\tilde{C}]^T\{u_\mathrm{n}\} \tag{2.96}$$

In these equations, $\{\}$ denotes a vector and $\langle\rangle$ its transpose. Using this, the weak integral mixed displacement-pressure formulation can be written in the following form (classical form for a fluid-structure coupled system):

$$\begin{pmatrix} [K] - \omega^2[\tilde{M}] & -[\tilde{C}] \\ -\omega^2[\tilde{C}]^\mathrm{T} & [\tilde{H}] - \omega^2[\tilde{Q}] \end{pmatrix} \begin{Bmatrix} u_\mathrm{n} \\ p_\mathrm{n} \end{Bmatrix} = \begin{Bmatrix} F_\mathrm{s} \\ F_\mathrm{p} \end{Bmatrix}, \tag{2.97}$$

where $[\tilde{M}]$ and $[K]$ represent the equivalent mass and stiffness matrices for the solid phase, $[\tilde{H}]$ and $[\tilde{Q}]$ the equivalent kinetic and compression energy matrices for the fluid phase and $[\tilde{C}]$ the volume coupling matrix between the solid phase displacement and the fluid phase pressure variables. $\begin{Bmatrix} F_\mathrm{s} \\ F_\mathrm{p} \end{Bmatrix}$ is the loading vector for the poroelastic medium and depends on the excitation. Solving System 2.97 gives the nodal displacements of the solid phase and the nodal pressures of the fluid phase.

2.3.2.1 Meshing criteria

Finite-element implementations of *Biot's theory* typically use linear or quadratic elements. Classical mesh criteria used for modal techniques and elastic domains are, however, not strictly applicable because of the existence of different wavelength scales and the highly dissipative nature of the domains. It has been shown that the classical mesh criterion of six linear elements per wavelength is insufficient for describing 3D deformations. In some applications, as many as 12 linear elements for the smallest *Biot wavelength* may be required for convergence [2].

3
Absorption

This thesis project aims to accurately model the sound transmission loss of multi-layer systems including poroelastic materials in FEM. Since it has not been possible to measure the sound transmission loss of the materials of interest, there is no data available for validating the simulation results. There have, however, been carried out measurements of the sound absorption coefficient of the samples of interest in a Kundt's tube by an external company[1] and by the authors of this report (Appendix D). This data, along with the results from TMM, is used as a reference for the FEM results.

It is initially assumed that a correct description of the multi-layer sample in an FEM model used for calculating the absorption coefficient also yields valid results in an FEM model used for calculating the sound transmission loss, although the sound absorption and transmission properties of a material are not entirely determined by the same mechanisms. For example, the sound absorption is governed by the amount of dissipated energy by visco-thermal effects within the material. This usually is less relevant for the sound transmission properties of a material, which are mainly governed by the deformation energy. Despite these insecurities, it is expected that the absorption model allows for determining the correct boundary conditions, necessary mesh size and correct modelling approaches for the different layers, which can then be used in the setup of the transmission loss model.

In the following, the noise shield under investigation is described in Section 3.1. Then, the methodology of the FEM and TMM modelling is described in Section 3.2. Finally, Section 3.3 combines the results and conclusions which are drawn from these simulations.

3.1 Noise shield under investigation

The noise shield of interest is composed of five layers. It consists of two layers of felt with different compression grades which are separated by a thin resistive screen interlayer. On both sides of this configuration, a thin screen is added. In the actual noise shield which is used for encapsulation, this basic configuration is compressed to different degrees, resulting in a change of thickness and compression grade of the felt materials over the area. Four different versions of this basic configuration, with different compression grades of the two felt materials, have been characterised by an external

[1] Matelys – Research Lab. Internal Data: Engineering Report ER-677017.

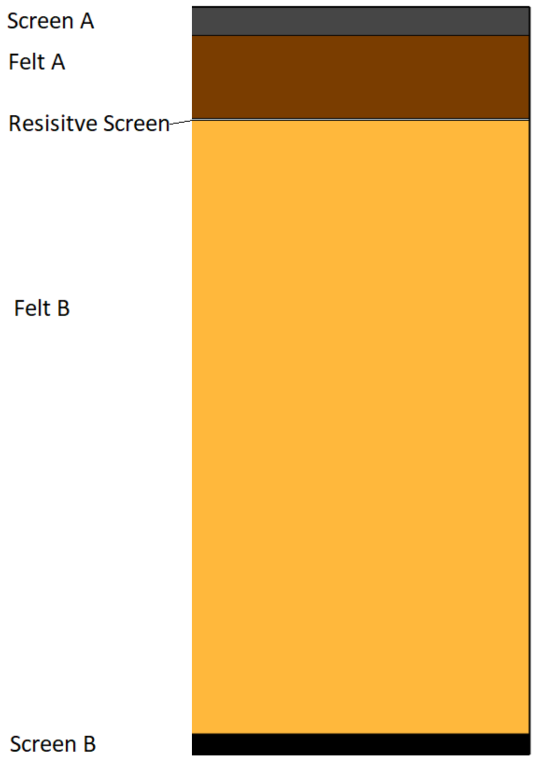

Figure 3.1: Structure of multi-layer sound absorber.

company.[2] The measured plane incidence absorption coefficients, as well as the characterised material parameters (acoustic and elastic parameters for the felt materials, only acoustic parameters for the screens and the resistive screen) are available.[3]

3.2 Methodology

Given the complexity of a multi-layer sound absorber, the characteristics of each component and the interactions between the different components need to be understood to achieve a valid model of the whole system. Therefore, any model should be tested incrementally, adding one component at a time. In this study, this is done in parallel using two software applications: Actran (version 2020) by Free Field Technologies for the FEM simulations and AlphaCell (version 12.0) by Matelys – Research Lab for the TMM simulations. In this way, the capabilities of each method/software can be evaluated, finding equivalent ways of simulating the same model. Comparing the results obtained by the two methods can reveal their limitations and highlight unrealistic assumptions, ruling out some potential models. Furthermore, insights into the physics can be gained by having different modelling perspectives on the same object.

Generally, this thesis work follows the approach of increasing the model complexity

[2] Matelys – Research Lab.
[3] Internal data: Engineering Report ER-677017 or see Appenix F.

step wise. It is started with calculating the sound absorption coefficient for normal plane wave sound incidence for simple configurations:

1. Felt only:
   - A single layer of felt B against a rigid backing.
2. Felt-screen combination:
   - Model of the felt against a rigid backing with screen A added in the incident direction. This model is also analysed with the screen and the felt in flipped order to determine the influence of the screen when located in between the felt and a rigid backing.
3. Resistive screen interlayer:
   - In this model, a thin resistive screen is modelled in between two layers of felt B.

These models allow for separately investigating the interactions between the screens and the felts as well as the resistive screen and the felts. The calculations of the absorption coefficient are done both in AlphaCell and in Actran (using a 2D Kundt's tube model). Based on the results of these simulations, different models of the full system are created in AlphaCell and Actran. These results are compared to the measured results, ruling out any models that might be consistent, but unrealistic.

The most accurate modelling approaches are then investigated further by creating 3D models in FEM. These are required for investigating the sound transmission loss of the system for diffuse sound incidence.

3.2.1 FEM: Model setup

This section describes the setup of the different FEM models. The sound absorption coefficient for normal plane wave sound incidence can be calculated using 2D or 3D models in Actran. The advantage of using 2D models is that they only require a fraction of the number of calculations, since the number of nodes is reduced significantly. However, this method can only be applied to symmetric models, which rules out investigations of asymmetric structures or structures under non-normal or diffuse sound incidence. The 2D simulations are used to evaluate the interaction between the different layers and to compare the FEM and TMM results to the measurement results. The 3D modelling is then used to check whether the 2D and 3D models behave in the same way for normally incident plane waves.

3.2.1.1 Plane wave normal incidence in 2D

The FEM model, seen in Figure 3.2, is set up as an air-filled tube at the end of which the sample under test is placed against a rigid backing. The edges of the sample are given sliding boundary conditions, removing the impact of structural modes, which allows the comparison to the TMM model. The mesh size is defined according to Table 3.1, fulfilling the 12 nodes per smallest wavelength criterion (compare Section 2.3.2.1) for most layers at an upper-frequency limit of 2 kHz. The density in the y-direction is higher than required and is mainly set to allow for modelling of the thin resistive screen. For the air-filled tube, a node density of 7 elements per wavelength can be considered sufficient, a criterion which is excelled by the chosen mesh. The number of nodes per smallest wavelength with the chosen mesh is shown in Table 3.2. Because of the low estimated Young's modulus ($E = 10^{-4}$ Pa) of the resistive screen[4] the node density in the x-direction is very low, which is not seen as critical, since for this model there is only one wave propagating in y-direction.

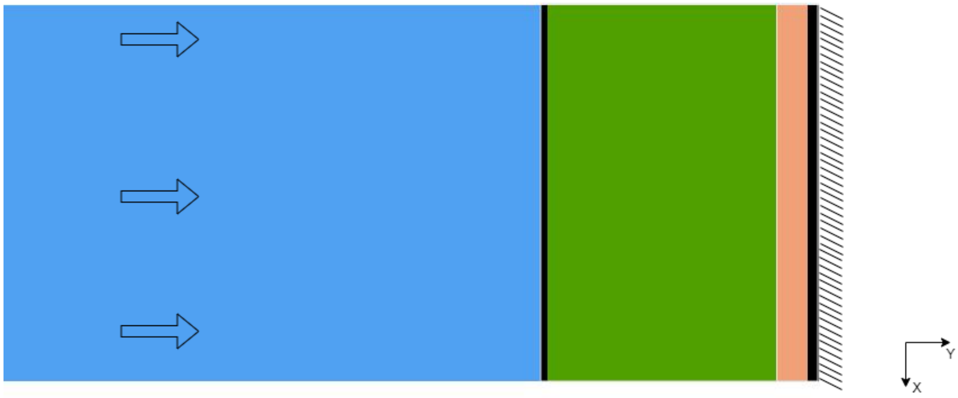

Figure 3.2: 2D model of sample at the end of the tube. Blue: Air, Black: Screens, White: Resistive screen (thin line between green and orange layers), Green/Orange: Felts.

Table 3.1: Mesh size of 2D FEM model. The wave is propagating in y-direction.

layer	mesh size:	x	y
sample		0.5 mm	0.1 mm
tube		0.5 mm	10 mm

Table 3.2: Number of nodes per smallest wavelength (shear wave) at 2 kHz for the different layers.

layer	nodes per wavelength:	x	y
screen B		12.0	60.0
screen A		12.1	60.4
felt B		12.8	63.8
felt A		9.1	45.5
resistive screen		2.0	10.1
air		343	17.2

The incident and reflected powers are calculated by the use of a modal duct component at the opposite end of the tube from where the sample is placed. This component allows for defining a plane incident wave in the direction towards the sample while letting the reflected wave, which is coming back from the sample, pass without being reflected again, thereby simulating a tube of infinite extend for the wave propagating

[4]Further details in Section 3.3.

away from the sample. The absorption coefficient α is calculated from the incident power W_{in} and the reflected power W_{ref} as

$$\alpha = \frac{W_{\text{in}} - W_{\text{ref}}}{W_{\text{in}}} = \frac{W_{\text{diss}}}{W_{\text{in}}}. \tag{3.1}$$

3.2.1.2 Plane wave normal incidence in 3D

The process of modelling the absorption for plane waves in 3D is nearly identical to the process in 2D. In 3D, the tube is modelled as a square instead, though due to the sliding boundary conditions, the approximation as an infinite plate is still valid and should generate the same or similar results as a 2D model. Unlike the 2D model, the 3D model is divided up in two topologies with a connecting interface. One topology represents the air and one the sample.

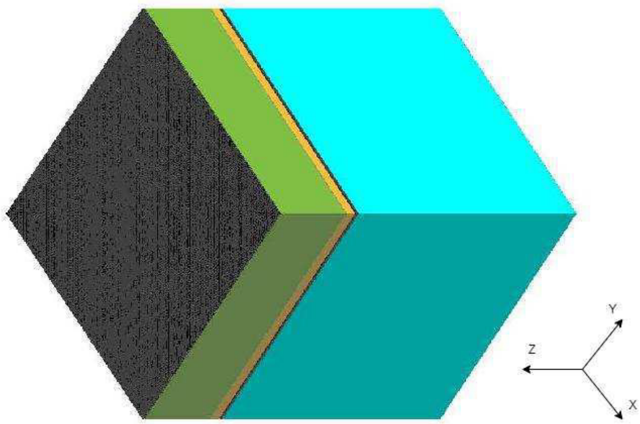

Figure 3.3: 3D model of sample at the end of a tube. Blue: Air, Black: Screens, White: Resistive screen, Green/Orange: Felts.

Due to the additional dimension, the number of required nodes increases exponentially, making it difficult to fulfil the demand of 12 elements per smallest wavelength. For softer materials, such as felts, foams, etc., the number of required elements quickly increases. This results in a model which is too large, even for dedicated simulation servers. To simulate the frequency range up to 2 kHz, the propagation speed in the material is increased by increasing Young's modulus of all materials by a factor of ten. This results in longer wavelengths, which allows for a coarser mesh. The used mesh and achieved number of elements per smallest wavelength are presented in Table 3.3 and 3.4.

Table 3.3: Mesh size in the mesh for the different layers.

layer	mesh size:	x	y	z
screen B		1.4 mm	1.4 mm	1.0 mm
screen A		1.4 mm	1.4 mm	1.4 mm
felt B		1.4 mm	1.4 mm	1.4 mm
felt A		1.4 mm	1.4 mm	1.4 mm
resistive screen		1.4 mm	1.4 mm	0.1 mm
air		20.0 mm	20.0 mm	20.0 mm

Table 3.4: Number of nodes per smallest wavelength at 2 kHz for the different layers (with increased Young's moduli). The normally incident plane wave is propagating in z-direction.

layer	nodes per wavelength:	x	y	z
screen B		13.6	13.6	19.0
screen A		13.7	13.7	13.7
felt B		14.4	14.4	14.4
felt A		10.3	10.3	10.3
resistive screen		2.3	2.3	32.1
air		8.6	8.6	8.6

3.2.1.3 Available components

In the FEM model, each layer of the sample is modelled as a component, describing how and which of the states of each node should be calculated. The components relevant for this study are listed below:

1. Poroelastic, based on *Biot's theory*:
   These components make use of both elastic and acoustic properties. The applied fluid phase model depends on the number of given parameters, with the options JCA, JCAL and JCAPL.
   - U-P: Four degrees of freedom as described in Section 2.1.3.3. Consideration of all elastic properties.
   - Lumped: This corresponds to the *limp equivalent fluid* model with one degree-of-freedom as described in Section 2.1.3.4. Only the density is used of the solid phase parameters.
2. Porous material with motionless skeleton:
   - Rigid: This enables the use of the JCA, JCAL and JCAPL models with a rigid and motionless skeleton.
   - DBM: Delany-Bazley-Miki model as described in Section 2.1.2.2.
3. 2D Solids:
   - Thin shell: 2D component with elastic and mass characteristics, bearing only bending motion (thin plate theory).
   - Perforated plate: 2D component adding visco-thermal effects to an elastic solid material.
4. 3D Solids:

- Solid: 3D component with elastic and mass characteristics, bearing full compression, bending and shearing motion.

3.2.2 TMM: Model setup

The TMM models are simulated using AlphaCell, for which the fundamental principles are described in Section 2.2. AlphaCell hosts a wider range of ways to model each layer. Specifically, it allows for combining each fluid phase model with each solid phase model, by the use of *Biot's theory* (compare Section 2.1.3.3). Thereby, it offers more flexibility. The following models are used in this work (the material parameters which are used in the different models are specified in Table B.1):

- Fluid phase:
  - Delany-Bazley-Miki
  - Miki
  - JCA
  - JCAL
  - JCAPL
  - Perforated Plate Circular
  - Screen
- Solid phase:
  - Elastic (isotropic)
  - Bonded septum: This creates a limp impervious layer.

In the TMM simulations, the systems are inherently considered to be of infinite extent. There are, however, different finite-size-correction models implemented which correct the sound radiation efficiency for a finite-size sample. There are a number of different excitation models available, of which the plane wave incidence and diffuse incidence are used in this study.

3.2.3 Investigated systems

This section describes the investigated systems, for which the simulation results are shown in Section 3.3.

3.2.3.1 Plane wave normal incidence (2D models)

Single layer of felt B: A model composed of a single layer of felt B against a rigid backing is used to determine the influence of the choice of fluid phase model. The felt is modelled with a rigid and motionless skeleton in order to investigate the fluid phase model only. The shape of the absorption coefficient curve is related to the *Biot wavelength* of the compressional wave in the *equivalent fluid*. It is also investigated, how big the influence of applying different elastic models is. The results are shown in Section 3.3.1.1 and Section 3.3.1.2.

Resistive screen interlayer: The interaction between the felt B material and a resistive screen interlayer is investigated using a model composed of two layers of felt B of equal thickness separated by a thin layer of the resistive screen against a rigid backing. The felts are modelled as poroelastic with a JCAL model for the fluid phase. Different modelling approaches for the resistive screen are compared. As before in the FEM calculations, the material is meshed with an element size of 0.1 mm in the y-direction. This results in only two nodes along the width of the resistive screen, one on each surface, when the width of the resistive screen is included in the mesh (as the case when modelled as a porous material or solid). Since the fluid phase parameters of the resistive screen have been measured, it can either be modelled as impervious or porous. At first, it is investigated how the elastic parameters of the resistive screen should be estimated. These material data has not been measured and has, therefore, to be estimated in order to use certain modelling approaches such as poroelastic or elastic solid. Then, the differences between seven different TMM modelling approaches and five different FEM modelling approaches for the resistive screen interlayer are investigated (compare Table 3.5). The results are shown in Section 3.3.1.3.

Table 3.5: Investigated modelling approaches for the resistive screen when used as interlayer between two felt materials. The TMM models are written in red and the FEM models in blue.

	elastic	limp
impervious	• elastic solid • thin shell • solid	• bonded septum • limp porous with impervious boundary conditions
permeable	• elastic porous • elastic screen • elastic perforated plate • porous UP • perforated plate	• limp porous • limp screen • limp porous

By adding small air gaps on both sides of the resistive screen interlayer, the influence of elastic coupling between both felts through the resistive screen is investigated. For the poroelastic model of the resistive screen, the influences of different porosity values are compared between the TMM and FEM simulations.

Resistive screen interlayer as perforated plate at a distance from a rigid backing: The behaviour of the resistive screen alone, when modelled as a perforated plate at a distance from a rigid backing, is investigated in FEM and TMM. The resistive screen is modelled with the estimated elastic properties $E = 10^4$ Pa and $\nu = 0.3$. The density and acoustic parameters are based on measurements. The shape of the absorption curve is investigated under consideration of the Helmholtz-resonator type of configuration. The results are shown in Section 3.3.1.4.

Felt-screen multi-layer system: The interaction between a felt and an added screen layer is investigated by the addition of a thin screen to the previously investigated felt B material. The elastic parameters of the screen are estimated. The same estimated values as for the previously described resistive screen interlayer are used. This system is investigated in both orders of felt and screen. This is meant to investigate two things:

1. How different means of modelling the screen influence the shape of the absorption curve when the **felt** is modelled as poroelastic.
2. How different means of modelling the felt influence the shape of the absorption curve when the **screen** is modelled as a perforated plate.

Full noise shield model: Finally, the full system as shown in Figure 3.1 is modelled in two different configurations (A and B), using seven different models in FEM and TMM (Table 3.6). The results are compared to the measured data to determine the modelling approaches which offer the best match to the measured data. The choice of the seven different models is informed by the experiences gained in the analysis of the previously described models. The results are shown in Section 3.3.1.6.

Table 3.6: Different modelling approaches for the full noise shield as planned. A revised version, based on the modelling results, can be found in Table 3.8.

	screen	felt	resistive screen	*comment*
v1	poroelastic	poroelastic	poroelastic	*highest number of DOFs*
v2	porous limp	poroelastic	porous limp	*based only on measured data*
v3	perforated	poroelastic	elastic solid	
v4	perforated	porous limp	elastic solid	*lowest number of DOFs*
v5	perforated	poroelastic	poroelastic	
v6	poroelastic	poroelastic	elastic solid	
v7	porous limp	poroelastic	elastic solid	

3.2.3.2 Plane wave normal incidence (3D models)

The transition to 3D is investigated by making the same plane wave incidence simulation but for a 3D model. In this case, the complexity of the model is not increased step wise as for the 2D equivalent. Instead, only the complete system is modelled, using the combinations of components determined to provide the best results in 2D (compare Section 3.3.1.6). The width of the sample, as well as each side in the cubic air volume, is 10 cm . The resulting absorption coefficients can be seen in Section 3.3.2.

3.2.4 Measurements

Measurements of the sound absorption coefficient for normal plane wave sound incidence in a Kundt's tube with different samples were carried out by the authors of this report at Chalmers. The results, however, differ from the results of the measurements which have been carried out by Matelys – Research Lab[5] and are not used for the validation of the simulation results. More details on these measurements, including theory, implementation and results, can be found in Appendix D.

[5]Internal data: Engineering report ER-677017.

3.3 Results

In this section, the results from the absorption coefficient calculations are shown. It is begun with the absorption coefficient for normal plane incident waves in 2D with simple systems. The complexity is increased step wise by adding additional layers. From the simulation results obtained for the full noise shield model the most accurate modelling approaches are determined by comparing the results to measurements. It is then checked whether 3D FEM models give the same results for normal plane wave incidence as 2D models.

3.3.1 Plane wave normal incidence (2D models)

3.3.1.1 The different fluid phase models

This model is composed of a single layer of felt against a rigid backing, as described in Section 3.2.3.1. In Figure 3.4 the results of TMM and 2D FEM calculations, obtained for the absorption coefficient of a single layer of felt B for plane sound incidence, are compared for different fluid phase models. The differences between the different models are $\Delta\alpha \leq 0.069$ in the frequency range 40 Hz to 4 kHz.[6] The frequency, for which the highest absorption is calculated (TMM results), ranges from 2 kHz with the Miki model, to 2.5 kHz with the Delany-Bazley-Miki model. The results obtained from the TMM and FEM calculations are similar but not identical.
The comparison of the results obtained from the different fluid phase models shows that, for this material, the flow resistivity alone is not sufficient to accurately describe the absorptive behaviour. The introduction of additional material parameters increases the accuracy, which might be desired in some cases.
Physically, for a porous material of this thickness backed by a rigid wall, it is classically expected that the absorption coefficient reaches values of $\alpha \approx 1$ for $f \geq f_{\lambda_{\mathrm{air}}/4}$ where $f_{\lambda_{\mathrm{air}}/4}$ (about 2.8 kHz in this case) is the first frequency for which the first velocity maximum in air, which occurs at a quarter wavelength distance from the rigid wall, is located within the material. The simulated results show, however, that the modelled absorption maximum is already reached below, rather than above that frequency. More accurately than considering the wavelength in air would be considering the wavelength of the compressional waves in the porous material (compare Section 2.1.3.2). With the JCAL model, the compressional wave with the larger wavelength (*solid wave*) has a wavelength of $\lambda_{\mathrm{comp},2} = 121.2$ mm (which corresponds to four times the thickness of the material) at $f_{\lambda/4_{\mathrm{comp},2}} = 1.9$ kHz (compare Figure 3.5). The first absorption maximum with the JCAL model occurs at 2.36 kHz, so for a frequency at which the first velocity maximum lies within the material. This shows, that by using the *Biot wavelengths* the shape of the absorption coefficient can be predicted more accurately than by using the wavelength in air.

[6] Maximum of the differences between the smallest and highest values at each frequency.

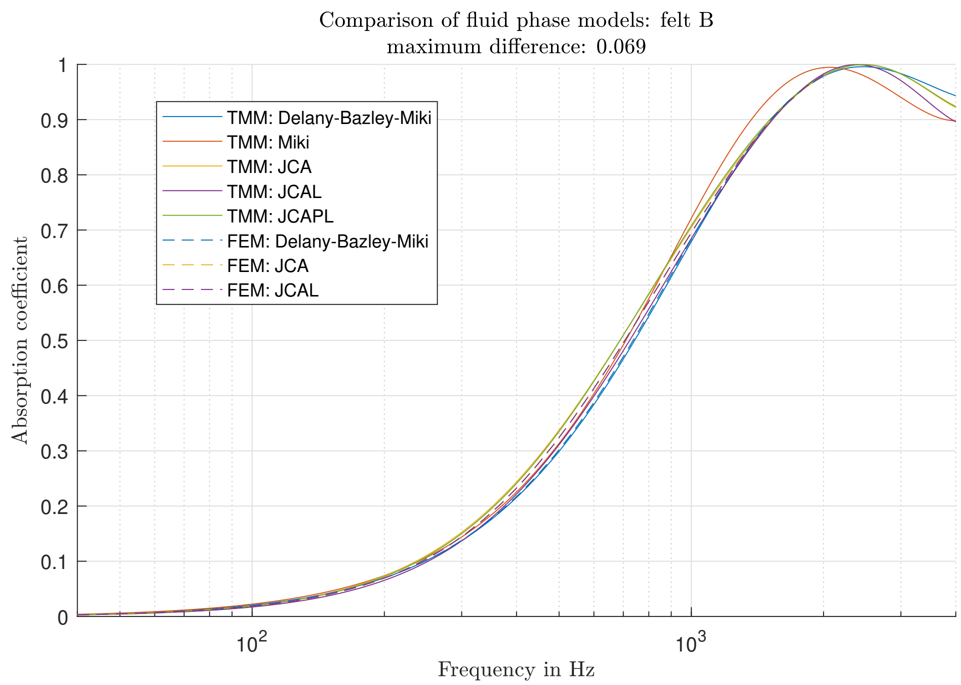

Figure 3.4: Calculated absorption coefficients for a single layer of felt for plane sound incidence with different fluid phase models in TMM and FEM. The elastic properties of the skeleton are not taken into account.

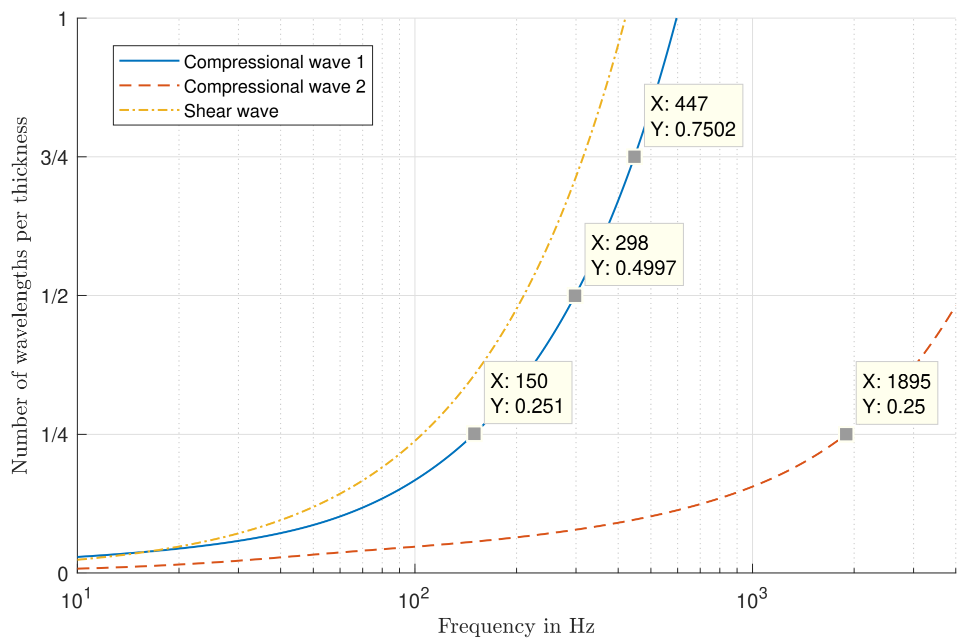

Figure 3.5: Calculated *Biot wavelengths* for the thick felt. The phase decoupling frequency for this material is 36.6 Hz. Above this frequency the waves propagating in the fluid and the skeleton are not coupled (compare Section 2.1.3.2). Compressional wave 1 is the *fluid wave* and compressional wave 2 the *solid wave.*

3.3.1.2 Poroelastic modelling of a single felt

For the same system, different means of considering the elastic properties of the material are compared in Figure 3.6, using the JCAL model to describe the dissipation in the fluid phase. There can be observed an excellent agreement between the FEM and TMM results (the deviations are $\Delta\alpha \leq 0.016$ for the elastic, limp and motionless skeleton models). Furthermore, it can be observed that for a single layer of this specific porous material the elastic properties are of minor importance. Neglecting the elastic properties saves computation time in the FEM calculations while not significantly affecting the results.

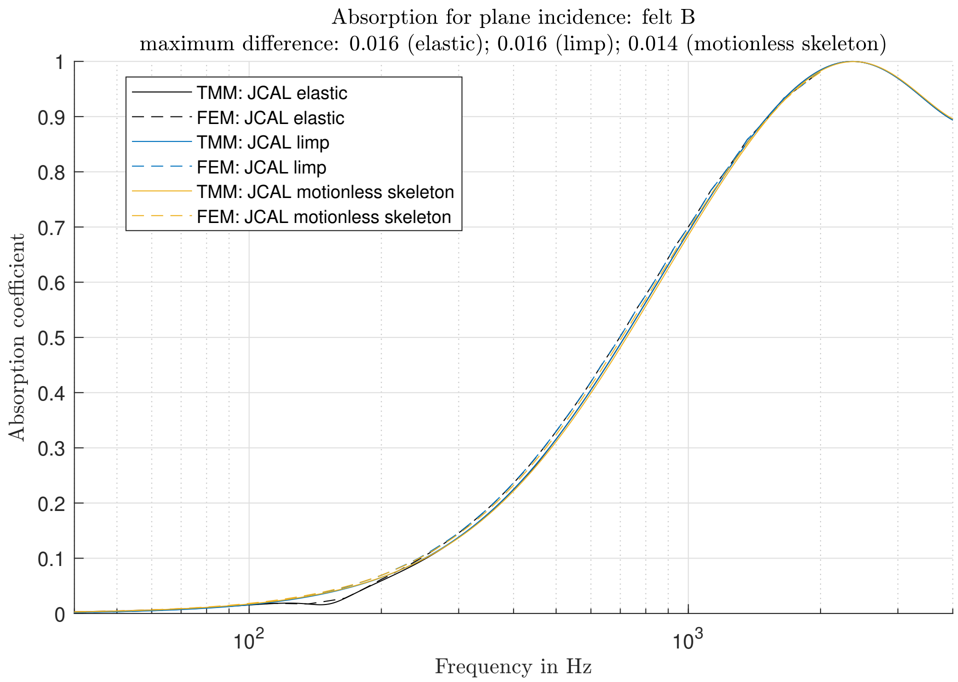

Figure 3.6: Comparison between the TMM and FEM results for the absorption coefficient for a single layer of felt with plane sound incidence.

Note, however, that for different materials, which exhibit more elastic effects, the results can differ much between the different modelling approaches, as shown in Section C.2.

3.3.1.3 Felt-screen-felt multi-layer system

The investigated system is composed of two felts, separated by a resistive screen as described in Section 3.2.3.1. For certain modelling approaches the elasticity of the resistive screen is required. Since the Young's modulus of the resistive screen has not been measured, it has to be estimated. The stiffness of the resistive screen is expected to be negligible, which is why a very low Young's modulus of $E = 10^3$ Pa is used as a starting point. In Figure 3.7 it can be seen that when increasing the Young's modulus by a factor of ten the result does not change (apart from little numerical deviations) for the FEM simulation, while it changes significantly for the TMM simulation. For $E = 10^4$ Pa the results of the TMM and FEM calculations match to each other, while they do not match for $E = 10^3$ Pa. Because of the better correspondence between the FEM and TMM simulations when modelling the resistive screen with a Young's modulus of $E = 10^4$ Pa this has been used for further calculations. For this Young's modulus, the results obtained from the TMM calculations when modelling the resistive screen as elastic solid are almost identical to the results obtained when modelling it as a bonded septum, which shows that for this Young's modulus the stiffness of the material, as intended, does not affect the results.

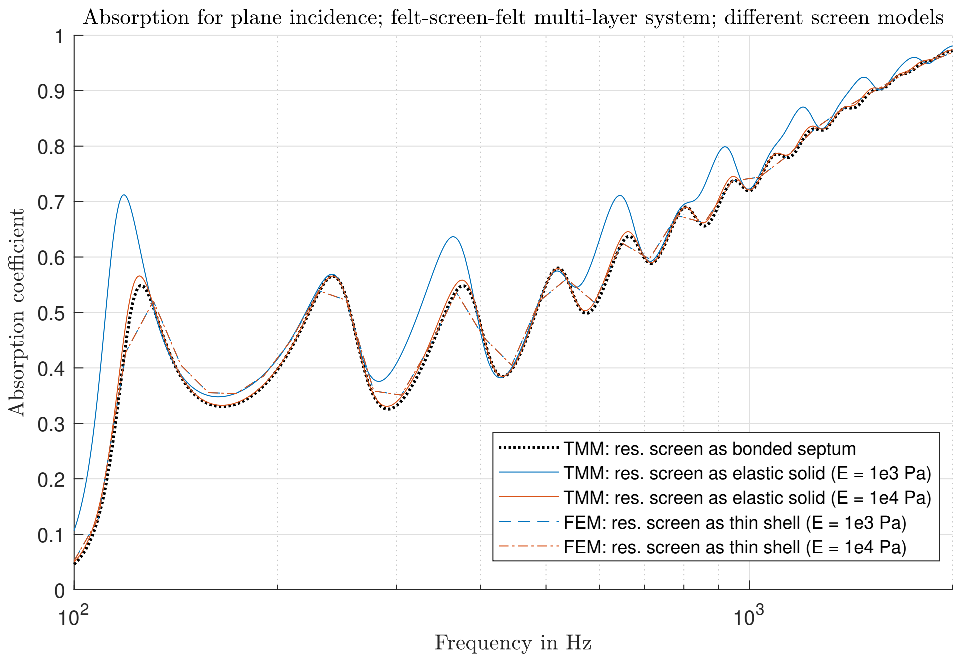

Figure 3.7: Calculated absorption coefficient of a multi-layer system composed of two felts, separated by a thin resistive screen. The resistive screen has been modelled with different estimated Young's moduli.

The dips in the absorption coefficient occur at 150 Hz, 300 Hz, 450 Hz, etc.. As it can be seen from Figure 3.5, these are the frequencies where quarter-wavelength resonances for the *fluid wave* in the felt occur. The resonances at 1/4, 3/4 etc. are resonances in the facing felt and the resonances at 2/4, 4/4 etc. are resonances in the backing felt. This behaviour is explained more in detail in Section C.3. Whether resonances lead to a dip or a peak in the absorption coefficient depends on the nature of the material. In this case, resonances in the fluid phase in one of the two felts lead to dips in the absorption coefficient. In terms of the peaks, comparing the results for different Young's moduli of the resistive screen shows that only every second peak in the absorption coefficient is influenced by this Young's modulus. The reason for this is unclear.

For the same multi-layer system, as a next step, different approaches for modelling the resistive screen are compared. In the results of the different TMM and FEM modelling approaches it can be observed that the results can be separated into two distinct categories (compare Figure 3.8, an overview is given in Table 3.7).

Within the two categories, there can be observed a good correspondence between the

FEM and TMM results. For the models that fall into the second category, there is accounted for visco-thermal dissipation in the resistive screen, which is not the case for the models falling into the first category. There are, however, some ambiguities between the FEM and TMM results for certain modelling approaches. For example, for the FEM model the shape of the calculated absorption coefficient when modelling the resistive screen as an elastic perforated plate falls into the first category, giving almost identical results as when modelling it as a thin shell, although this model should account for visco-thermal dissipations in the resistive screen. In the TMM simulations, considering the resistive screen as an elastic perforated plate gives identical results to the calculation as an elastic screen, as expected. Another ambiguity is found when modelling the resistive screen as poroelastic, which falls into the first category for FEM and the second category for TMM.

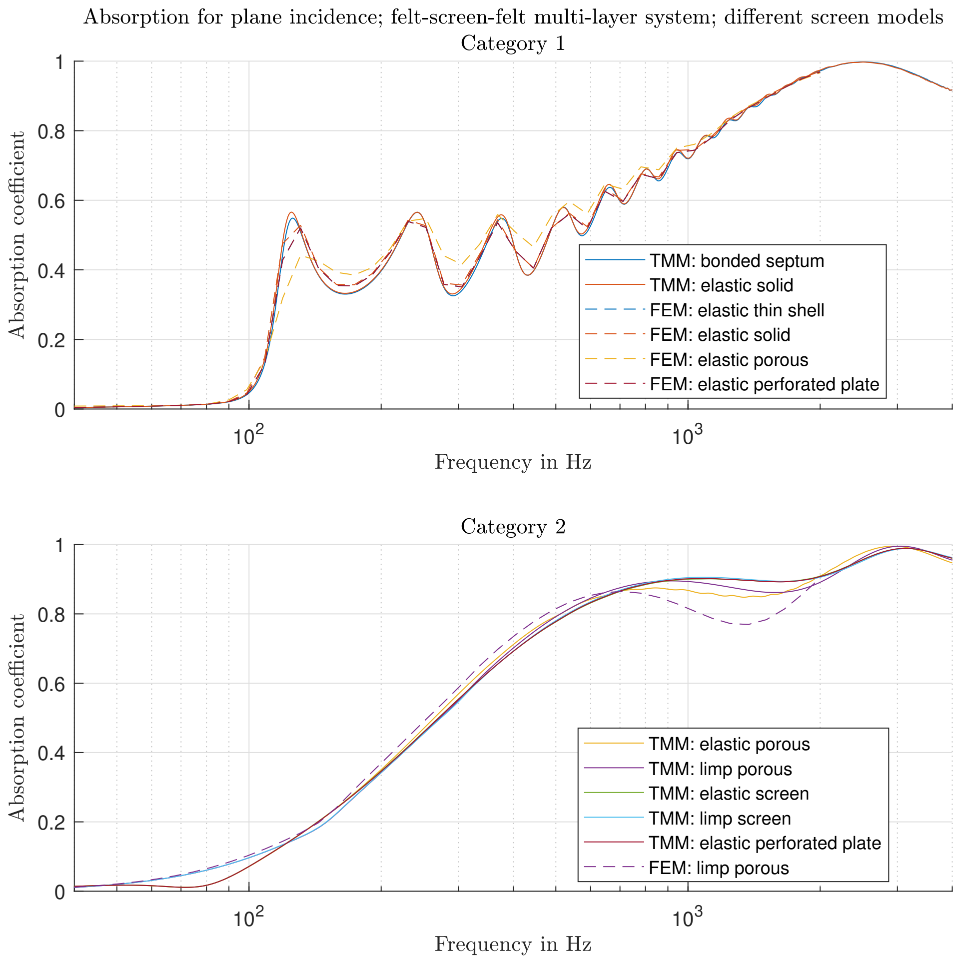

Figure 3.8: Calculated absorption coefficient of a multi-layer system composed of two felts, separated by a thin resistive screen. The felts are modelled as poroelastic. Different modelling approaches for the resistive screen are compared. The results fall within two distinct categories.

In order to further investigate the apparent ambiguities, specifically for the case of modelling the resistive screen as a perforated plate, the effect of inserting a 0.1 mm air gap on both sides of the resistive screen is investigated, the results of which are shown in Figure 3.9. It can be observed that, in contrast to the configuration without air gap, the modelling of the resistive screen as a perforated plate yields the same results in the FEM and TMM calculations when an air gap is added on both sides of the resistive screen.[7] Further investigations, not shown here for the sake of conciseness, reveal that when the elastic coupling is eliminated by modelling the felts as limp, the calculated absorption coefficient curves also take the shape of the second category.

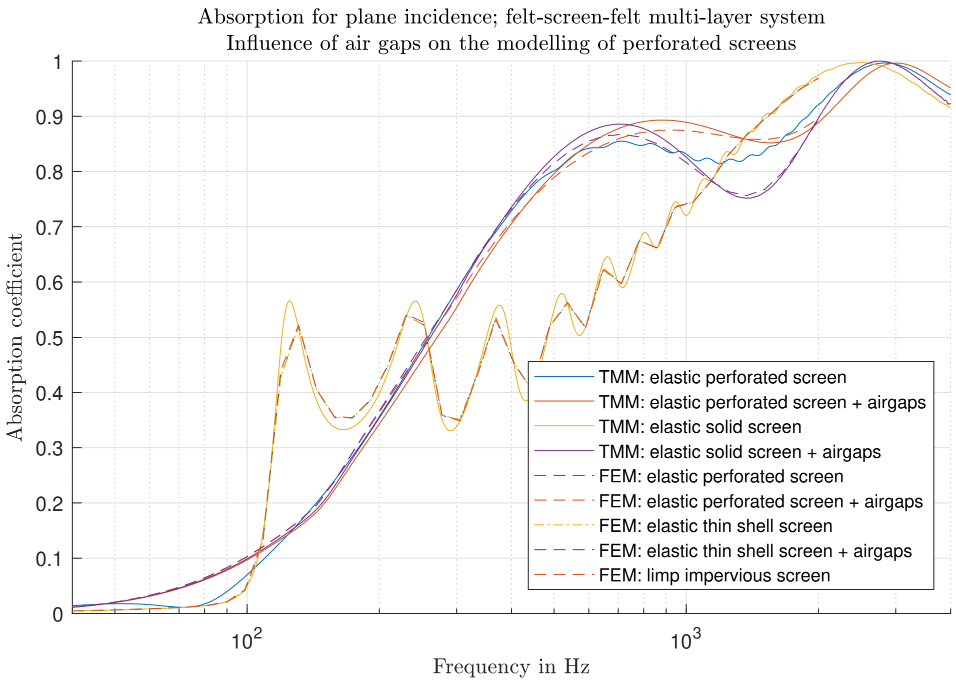

Figure 3.9: Calculated absorption coefficient of a multi-layer system composed of two felts, separated by a thin resistive screen. The felts are modelled as poroelastic. Different modelling approaches for the resistive screen are compared. The influence of adding a 0.1 mm air gap on both sides of the resistive screen is investigated.

The results of the conducted felt-screen-felt investigations are summarised in Table 3.7. Again, it shows that most modelling approaches follow the expected behaviour (models that include visco-thermal dissipation fall into the second category), except for the FEM models where the resistive screen is modelled as poroelastic or elastic perforated plate.

The behaviour of the poroelastic model is investigated further by modelling the resistive screen with different porosities (without changing other parameters, which only makes the result valid for investigating the modelling, not for describing real materials).

[7] This indicates that in the used FEM software (Actran 2020) the interface continuity equations for the perforated plate model are not correctly handled.

Table 3.7: Summary of Figure 3.8 and Figure 3.9. Comparison of different resistive screen models. The felts are modelled as poroelastic.

resistive screen model	method	visco-thermal dissipation	elastic dissipation	category
bonded septum	TMM			1
elastic solid	TMM		x	1
elastic solid with air gaps	TMM	x	x	2
porous elastic	TMM	x	x	2
porous limp	TMM	x		2
screen elastic	TMM	x	x	2
screen limp	TMM	x		2
perforated plate elastic	TMM	x	x	2
perforated plate elastic with air gaps	TMM	x	x	2
thin shell	FEM		x	1
thin shell with air gaps	FEM	x	x	2
solid	FEM		x	1
porous elastic	FEM	x	x	1
perforated plate elastic	FEM	x	x	1
perforated plate elastic with air gaps	FEM	x	x	2
porous limp	FEM	x		2
porous limp (impervious surfaces)	FEM			1

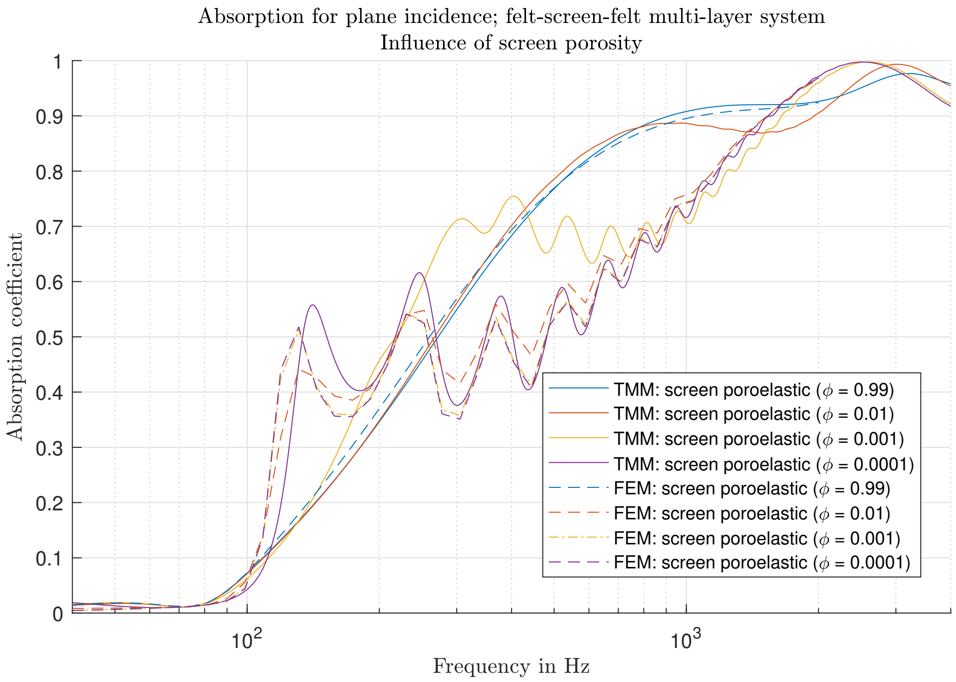

Figure 3.10: Calculated absorption coefficient of a multi-layer system composed of two felts separated by a thin resistive screen. Both the felts and the resistive screen are modelled as poroelastic. The influence of different porosity values in the FEM and TMM simulations is compared.

The theoretically expected behaviour is that the resulting absorption coefficient curve for high porosities becomes similar to the case where the two felts are just separated by an air gap, while for very low porosities it becomes similar to the case of modelling the resistive screen as an elastic solid. In other terms, the contribution of visco-thermal dissipation should increase for higher porosities. This expectation is confirmed by the results shown in Figure 3.10. However, it can be observed that in the FEM simulation the transition from a permeable to an impervious behaviour of the resistive screen happens already (in the wide range) between $\phi = 0.99$ and $\phi = 0.1$, while it happens later, between $\phi = 0.01$ and $\phi = 0.0001$, in the TMM simulation. This explains why the results of the FEM and TMM simulations shown in Figure 3.8 look so different when the resistive screen is modelled as poroelastic. The characterised porosity of the resistive screen (see Table F.1) leads to a modelled behaviour on the borderline between a rather permeable or rather impervious resistive screen, where the FEM simulation, in this case, is on the impervious and the TMM simulation on the permeable side. This suggests that, depending on which behaviour is deemed more physically reasonable, the porosity might have to be adapted in one or the other model when modelling the resistive screen as poroelastic.

3.3.1.4 Perforated resistive screen at a distance from a rigid backing

The investigated system is a resistive screen modelled as a perforated plate in front of an air gap backed by a rigid wall, as described in Section 3.2.3.1. The results from the FEM and TMM calculations are compared in Figure 3.11 for two different resistive screen thicknesses. It can be observed that the general shapes of the calculated absorption coefficient curves are the same for the FEM and TMM calculations (in contrast to the previously presented felt-screen-felt system) and that the resonance is predicted at similar frequencies. However, the value of the calculated absorption coefficient at the resonance frequency differs ($\Delta\alpha = 0.16$) between the FEM and TMM simulations for the 0.1 mm resistive screen. These results indicate that the problem in the perforated plate model (Actran 2020) only exists for coupling to porous materials.

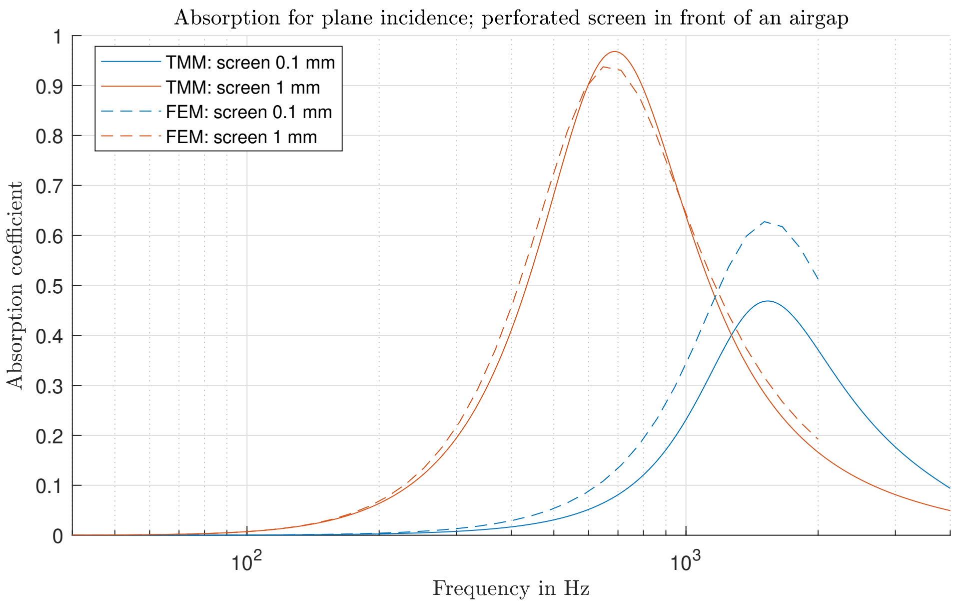

Figure 3.11: Absorption coefficient for plane sound incidence for a resistive screen modelled as perforated plate in front of an air gap backed by a rigid wall.

Physically, the resonance frequencies can be explained by considering the perforated resistive screen in combination with the air gap as a Helmholtz resonator. Based on the equations presented in Appendix A.1, the Helmholtz resonance frequencies of the resistive screens are calculated at 742 Hz and 1.44 kHz, which matches to the simulated absorption coefficient curves.

3.3.1.5 Felt-screen multi-layer system

The investigated system is a felt layer with an added screen layer as described in Section 3.2.3.1. The results of the TMM and FEM simulations (Figure 3.12) show that the characteristic shape of the absorption curve of the felt is maintained when the screen is added and only slightly shifted to lower frequencies. The upper part of Figure 3.12 compares different models for the screen when the felt is modelled as poroelastic. It shows that, as long as the screen is modelled as permeable, the exact modelling approach does not have a huge influence (the maximum difference between the different FEM models is 0.042 and 0.041 between the different TMM models in the frequency range 40 Hz to 4 kHz). This holds even when the screen is modelled with a motionless skeleton. The low influence of the screen, in this case, is caused by the fact that its airflow resistance is about eight times lower than that of the felt. The lower part of Figure 3.12 compares different elastic models for the felt when the screen is modelled as an elastic perforated plate. It shows that also the elastic modelling of the felt is of minor importance in this simple two-layer system.

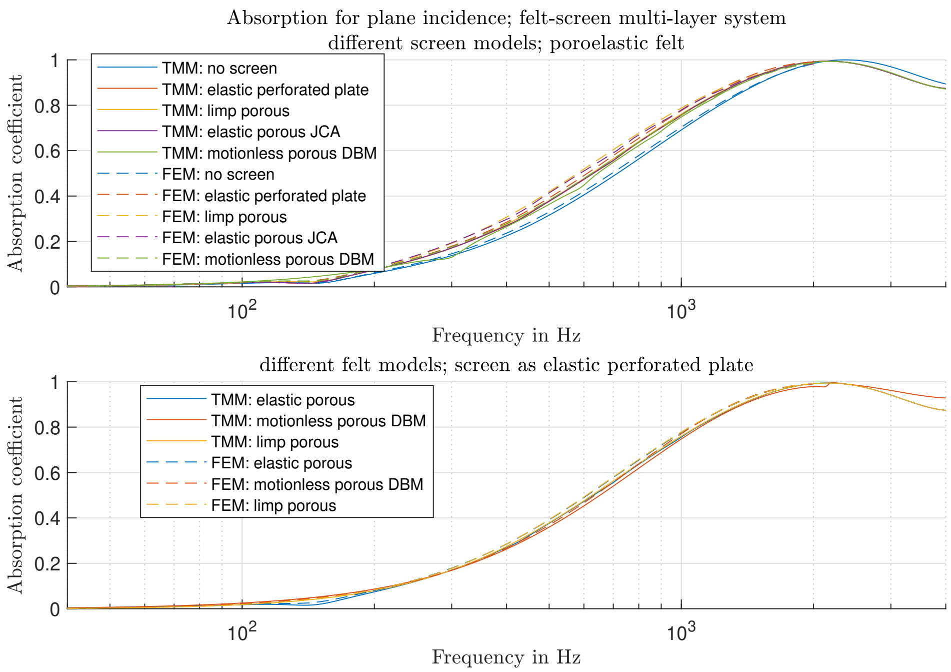

Figure 3.12: Absorption coefficient for plane sound incidence for a felt covered by a thin screen. Different modelling approaches for the felt and the screen are compared. The felt has an air flow resistance which is about eight times higher than the air flow resistance of the screen.

When switching the order of the screen and the felt, so that the screen is on the side facing the rigid backing, the deviations between the different modelling approaches are even smaller (compare Figure 3.13). In this case, the screen can also be neglected completely without significantly changing the results (the maximum difference between the mean of the models including the screen to the modelling without the screen is $\Delta\alpha_{\max} = 0.012$ in the frequency range 40 Hz to 2 kHz for the FEM models and $\Delta\alpha_{\max} = 0.026$ in the frequency range 40 Hz to 4 kHz for the TMM models). The maximum difference between the mean of the different FEM results to the mean of the different TMM results in the frequency range 40 Hz to 2 kHz is $\Delta\alpha_{\max} = 0.007$.

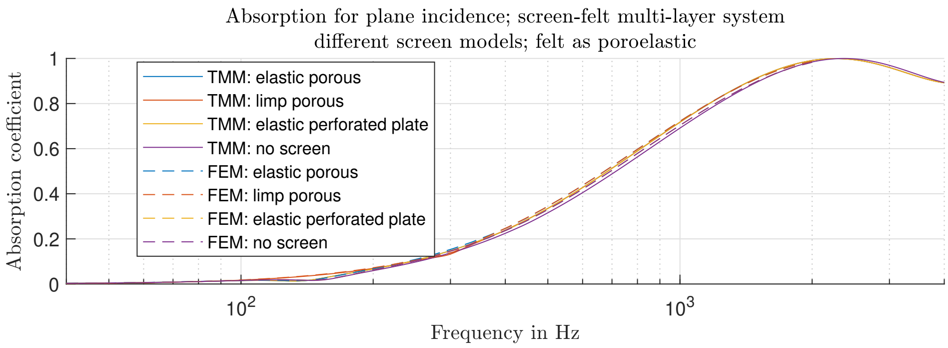

Figure 3.13: Absorption coefficient for plane sound incidence for a felt, separated from a rigid backing by a thin screen. Different modelling approaches for the screen are compared.

3.3.1.6 Full system

The FEM and TMM results with seven different modelling approaches as described in Section 3.2.3.1 are compared to the measured sound absorption coefficient in Figure 3.17. The results are summarised in Table 3.8. In the first model, it shows that when the resistive screen is modelled as poroelastic in TMM the open porosity ϕ has to be decreased to achieve a better match to the FEM results and the measurements (Figure 3.14). This matches the previously made observations about the behaviour of the poroelastic resistive screen models (compare Figure 3.10). The second model uses the exact material data which has been characterised, i.e. there are no elastic properties estimated for the resistive screen and the felts. It shows that the FEM and TMM results for this model are similar but the measured behaviour is not accurately represented (compare Figure 3.17). The third, fourth and fifth model, which make use of elastic perforated plates for modelling the screens, show that the FEM implementation of the elastic perforated plate model does not work as expected[8] and can, therefore, not be used (compare Figure 3.17). For the sixth model it shows that, when the resistive screen is modelled as elastic shell in FEM, the calculated sound absorption coefficient strongly deviates from the TMM results and the measurements above 1 kHz (compare Figure 3.15). Modelling the resistive screen as a limp porous material with impervious surfaces solved that problem and gives results almost identical to the TMM results, for which it does not matter whether the resistive screen is modelled as an elastic solid or bonded septum. By changing the Young's moduli of the two

[8] In Actran 2020.

screens ($E_{\text{screen:A}} = 3.5 \cdot 10^4$ Pa, $E_{\text{screen:B}} = 5.2 \cdot 10^4$ Pa)[9] the peaks in the absorption coefficient (side A) can be matched closer to the measurements. In the seventh model, where the screens are modelled as porous limp, the peaks in the absorption coefficient at low frequencies (side A) do not occur at the measured frequencies, which shows that the frequencies at which these peaks occur are influenced by the elasticity of the screens (compare Figure 3.16).[10] However, there can be observed an excellent match between the FEM and the TMM results, and the modelled behaviour at higher frequencies matches similarly well to the measurements as for the sixth model. Furthermore, it can be observed that when the screens are modelled as limp it has, in contrast to the sixth model, no influence whether the resistive screen is modelled as an elastic shell or as limp porous material with impervious surfaces in FEM.

This leaves the first, the sixth and the seventh model as candidates for further investigations. Generally, it can be noted that the overall behaviour of the absorption coefficient is well captured by the models. The absorption coefficient peaks at low frequencies are calculated much higher than measured but these peaks mostly occur outside of the frequency range, for which the measurements are valid (≥ 250 Hz). The peaks at higher frequencies (side A) strongly depend on the mounting conditions and are difficult to predict.

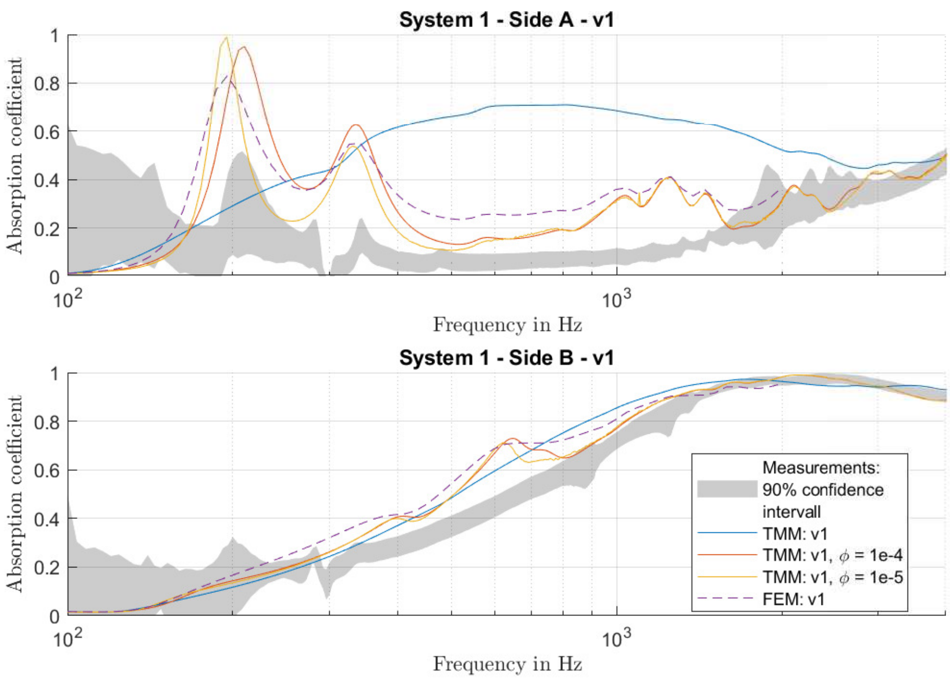

Figure 3.14: Full system, model 1. Adjusting the porosity value in the TMM model gives a better fit to the FEM results and the measured data. The measurements are valid above 250 Hz.

[9]Using these Young's moduli, the 12 elements per wavelength criterion in FEM is fulfilled with an element size of 0.5 mm.

[10]It has to be noted here that the mentioned peaks occur outside of the frequency range for which the measurements are valid.

Table 3.8: Evaluation of different modelling approaches for the full system (compare Figure 3.17).

	screen	felt	resistive screen	comment
v1	poroelastic	poroelastic	poroelastic	Needs adjustment (decrease) of porosity in TMM, i.e. a poroelastic modelling of the resistive screen is possible when the porosity is very low.
~~v2~~	~~porous limp~~	~~poroelastic~~	~~porous limp~~	Does not fit the measured data (due to limp modelling of resistive screen).
~~v3~~	~~perforated~~	~~poroelastic~~	~~elastic solid~~	Bug with perforated plate objects in Actran (in Actran 2020 perforated plate objects do not behave correctly when coupled to poroelastic materials).
~~v4~~	~~perforated~~	~~porous limp~~	~~elastic solid~~	"
~~v5~~	~~perforated~~	~~poroelastic~~	~~poroelastic~~	"
v6	poroelastic	poroelastic	limp impervious (FEM)	Works with adjustment of resistive screen modelling (limp porous with impervious surfaces instead of elastic solid).
v7	porous limp	poroelastic	elastic solid	Gives wrong resonances (at low frequencies), also works with limp impervious modelling of resistive screen.

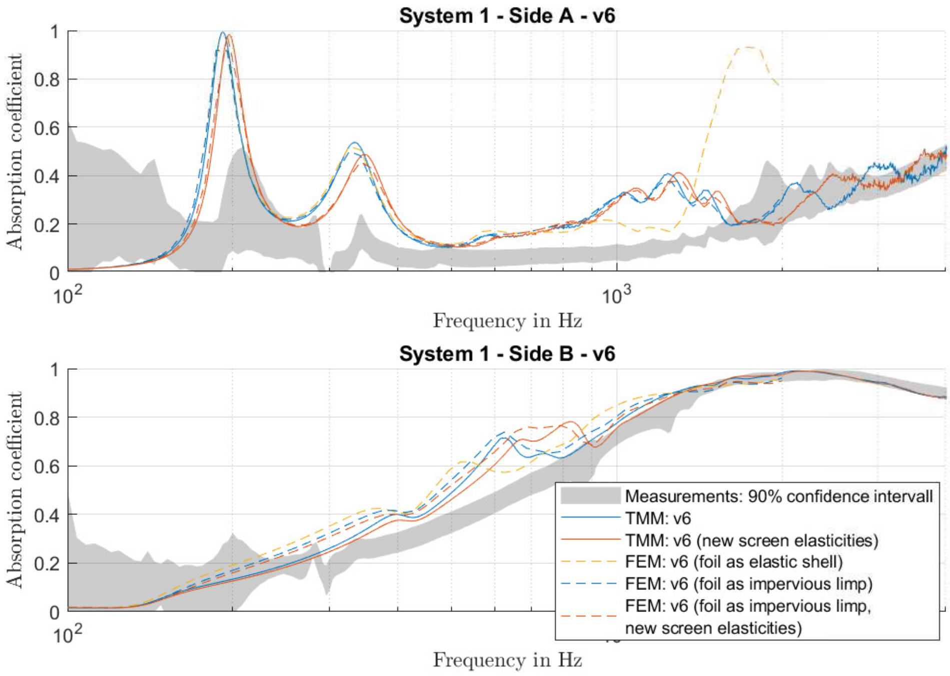

Figure 3.15: Full system, model 6. Modelling the resistive screen as limp porous material with impervious surfaces matches the FEM to the TMM results. The measurements are valid above 250 Hz.

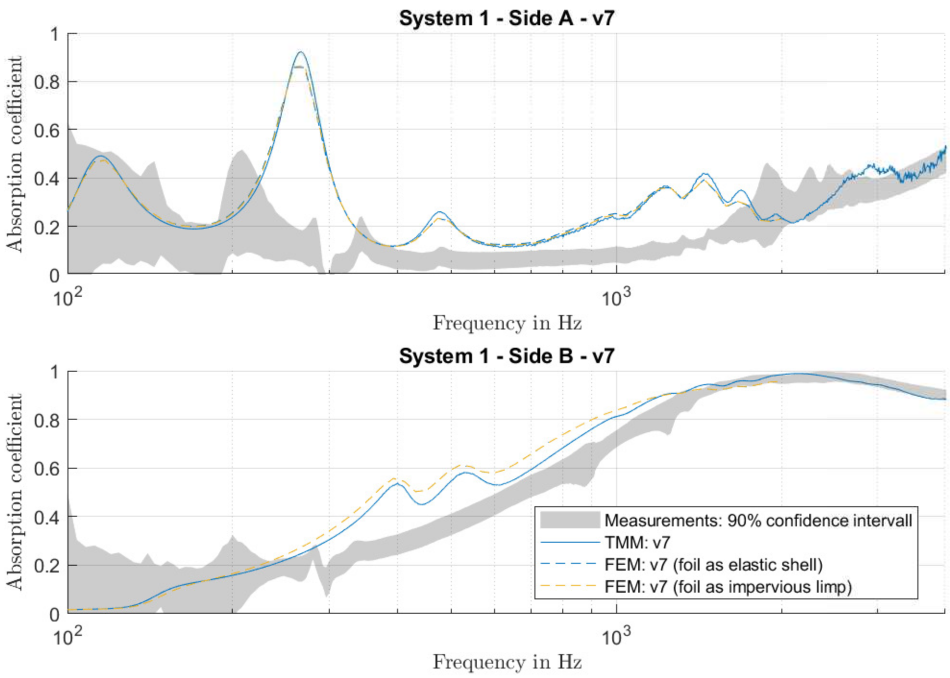

Figure 3.16: Full system, model 7. When the screens are modelled as limp it does not have an influence whether the resistive screen is modelled as elastic shell or as impervious limp porous material in FEM. The measurements are valid above 250 Hz.

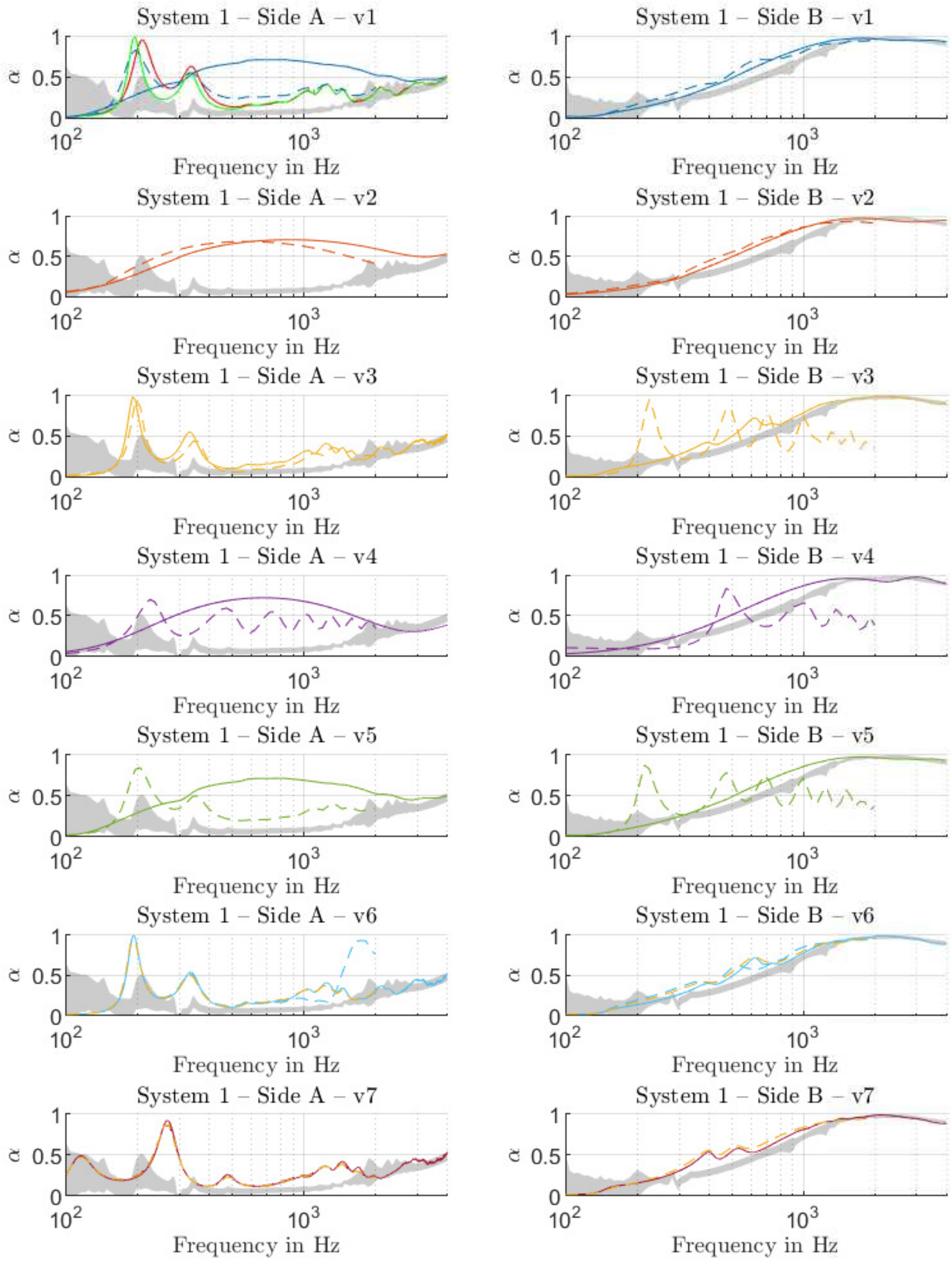

Figure 3.17: System 1, all modelling approaches (compare Table 3.6). The measurements are valid above 250 Hz. The dashed lines represent the FEM results, the solid lines the TMM results. Additional lines are specified in Figure 3.14, 3.15 and 3.16.

3.3.2 Plane wave normal incidence (3D models with increased Young's modulus)

As described in Section 3.2.1.2, the Young's modulus of all materials has to be increased by a factor of ten in order to achieve a sufficiently high number of elements per wavelength at 2 kHz with the available computational power. With the original material parameters, the resulting number of degrees-of-freedom (using a small 0.01 m^2 sample) is too high to be calculated even by a dedicated simulation server (requiring too much memory space; this issue is discussed more in detail in Chapter 4). The results of the TMM and FEM simulations with the increased Young's moduli are shown in Figure 3.18 together with the measured data. It can be observed that for models v1 and v6, for which there is observed a good agreement between the FEM and TMM results in the 2D model with the original Young's moduli, the results match worse for the 3D model with the increased Young's moduli due to a shift of the resonance peaks in frequency. This shift does not occur for model v7. The reason for this is unclear. Apart from these resonance peaks, the measured behaviour is, however, still well captured by the 3D models with increased Young's moduli, especially at high frequencies.

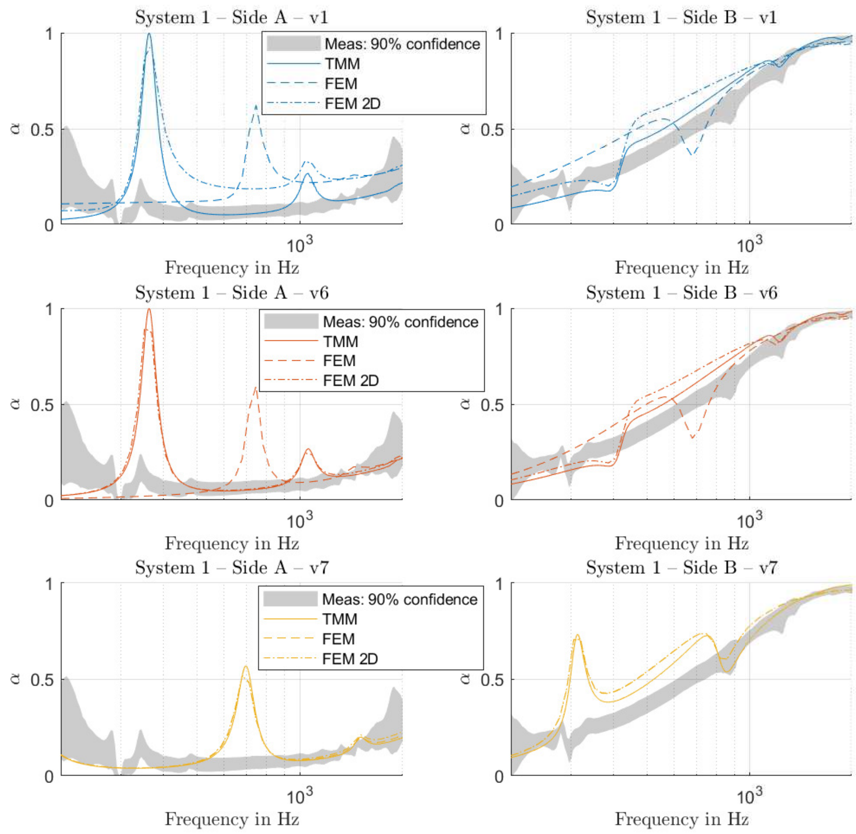

Figure 3.18: Full system, modelling approaches v1, v6 and v7 (compare Table 3.6). The measurements are valid above 250 Hz. The Young's moduli of all materials have been increased by a factor of ten, in both the TMM and FEM simulations.

4
Transmission

The modelling of the sound transmission loss of the multi-layer noise shield is based on the results obtained in the modelling of the sound absorption for normally incident plane waves. The absorption modelling allowed the identification of the most accurate modelling approaches for the single layers, as well as the modelling approaches for the complete multi-layer noise shield system which give the best match to the TMM simulations and measurements. These results are used in the setup of the transmission models. Since there is no measured data available for the transmission loss, the FEM simulation results can only be compared to the results of the TMM simulations for validation. The transmission loss of the complete system is calculated for normally incident plane waves in 2D and 3D models and for a diffuse incident sound field in 3D models. Mesh size sensitivity studies are added for the 2D plane wave case and the 3D diffuse incidence case.

4.1 Methodology

This section describes the methodology of the FEM model setup. The TMM setup is essentially the same as described in Section 3.2.2 (apart from calculating the transmission loss instead of the absorption coefficient) and not repeated here. The only investigated system is the full noise shield model, with different modelling approaches as listed in Table 3.8.

4.1.1 FEM: Model setup

This section describes the FEM model setup for normally incident plane waves in 2D and 3D and a diffuse incident sound field in 3D.

4.1.1.1 Plane wave normal incidence in 2D

The transmission model for plane wave normal incidence in 2D is set up in a similar way as described for the 2D plane wave normal incidence absorption model in Section 3.2.1.1. Instead of terminating the sample by a rigid backing, an air-filled tube with the same dimensions as the incidence tube is placed on the other side of the sample. At the end of this tube, an additional modal duct component is defined, which lets the wave transmitted through the sample propagate without being reflected at the end of the tube, thereby simulating a tube of infinite extend for the wave propagating away from the sample. The transmission loss is calculated from the incident power of the modal

Figure 4.1: FEM model simulating transmission from plane wave incidence in a 2D geometry.

duct component in the first tube and the incident power of the modal duct component in the second tube as

$$TL = 10\log\left(\frac{W_{\text{inc}_{\text{tube},1}}}{W_{\text{inc}_{\text{tube},2}}}\right)\ \text{dB} = 10\log\left(\frac{W_{\text{inc}}}{W_{\text{trans}}}\right)\ \text{dB}. \tag{4.1}$$

The edges of the sample are given sliding boundary conditions, thereby simulating a material of infinite extend.
The chosen mesh size is shown in Table 4.1. With this mesh, the number of nodes per wavelength listed in Table 4.2 is reached. All layers except the resistive screen easily fulfil the 12 elements per wavelength criterion. The results are shown in Section 4.2.1.

Table 4.1: Mesh size in the 2D plane wave normal incidence transmission model. The normally incident plane wave is propagating in y-direction.

	mesh size:	x	y
tube		0.1 mm	10 mm
sample		0.1 mm	0.1 mm

Table 4.2: Number of nodes per smallest wavelength at 2 kHz for the different layers. The normally incident plane wave is propagating in y-direction.

layer	nodes per wavelength:	x	y
screen B		60.1	60.1
screen A		60.4	60.4
felt B		63.8	63.8
felt A		45.5	45.5
resistive screen		10.1	10.1
air		1715	17.2

4.1.1.2 Plane wave normal incidence in 3D

As for the absorption models, the 3D model (Figure 4.2) for plane wave transmission is almost identical to its 2D counterpart. Just as the absorption model, the lengths of the

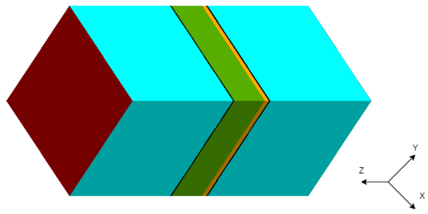

Figure 4.2: FEM model simulating transmission from plane wave incidence in a 3D geometry.

air volumes are the same as the width of the sample (10 cm). Utilising the same sliding boundary conditions and modal duct components, the model is designed to generate as similar results to the 2D model as possible. Like for the absorption model, the nodal density required to fulfil the 12 elements per smallest wavelength criterion with the original material parameters cannot be implemented due to insufficient memory on the calculation server. By applying the same solution of increasing the Young's modulus, models can be simulated up to 2 kHz while avoiding numerical issues.

The chosen mesh size is the same as for the 3D absorption model which can be seen in Table 3.3. The number of nodes per smallest wavelength is shown in Table 3.4. The results are shown in Section 4.2.3.

4.1.1.3 Diffuse incidence in 3D

The 3D transmission model for diffuse sound incidence is different from its normal incident plane wave counterpart. For diffuse incidence, modal duct components cannot be used. The air components are expanded to be significantly wider than the sample and their outer shells are modelled as infinite fluid elements, simulating free field radiation. On the infinite fluid domain on the incidence side a "Sample Random Diffuse Field"-boundary condition is defined to create the diffuse incident sound field. This allows the user to specify the number of angles (parallels) of incidence of the sound field from a spherical sector with its centre in the middle of the sample surface. The angle and radius of the sector are also specified by the user. The settings chosen for this model are 16 parallels spread over a maximum angle of 80° (around the axis parallel to the sample normal vector) and a radius about ten times longer than the width of the sample. The transmission loss is calculated similarly to the plane wave incidence with Equation 4.1. The incident power W_{inc} is defined as the power flow through the incident surface of the sample, with the same size as the sample. The transmitted power W_{trans} is defined as the power flow going out through the infinite fluid domain on the radiating side.
For the diffuse transmission model (Figure 4.3), the original parameters of each material are used, as well as the version with increased Young's moduli. The chosen mesh size is shown in Table 4.3. The resulting numbers of nodes per smallest wavelength

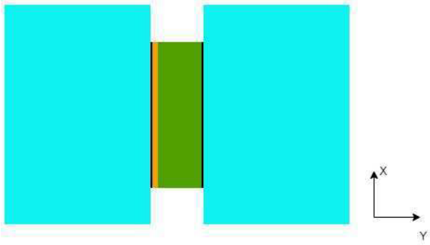

Figure 4.3: FEM model simulating transmission from diffuse incidence in a 3D geometry.

at 2 kHz are listed in Table 4.4 for the original material data and Table 4.5 for the version with increased Young's moduli. The results are shown in Section 4.2.5. The mesh size sensitivity study is done for the model with increased Young's moduli since for the smallest possible node distance of 1 mm the 12 elements per smallest wavelength criterion is not fulfilled with the original material data. In the mesh size sensitivity study the node distances 20 mm, 15 mm, 10 mm, 8 mm, 6 mm, 4 mm, 2 mm and 1 mm are used.

Table 4.3: Mesh size for the different layers. The normal of the sample surface is parallel to the z-axis. The ø column indicates the length of the diagonal in the 3D cuboids.

layer	mesh size: x	y	z	ø
screen B	1.0 mm	1.0 mm	1.0 mm	1.7 mm
screen A	1.0 mm	1.0 mm	1.0 mm	1.7 mm
felt B	1.0 mm	1.0 mm	1.0 mm	1.7 mm
felt A	1.0 mm	1.0 mm	1.0 mm	1.7 mm
resistive screen	1.0 mm	1.0 mm	0.1 mm	1.4 mm
air	20.0 mm	20.0 mm	20.0 mm	34.6 mm

Table 4.4: Number of nodes per smallest wavelength at 2 kHz for the different layers (**with original Young's moduli**). The normal of the sample surface is parallel to the z-axis. The ø column indicates the number of nodes along the length of the diagonal in the 3D cuboids.

layer	nodes per wavelength: x	y	z	ø
screen B	6.0	6.0	6.0	3.5
screen A	6.0	6.0	6.0	3.6
felt B	6.4	6.4	6.4	3.8
felt A	4.5	4.5	4.5	2.7
resistive screen	1.0	1.0	10.1	0.7
air	8.6	8.6	8.6	5.0

Table 4.5: Number of nodes per smallest wavelength at 2 kHz for the different layers (**with increased Young's moduli**). The normal of the sample surface is parallel to the z-axis. The ø column indicates the number of nodes along the length of the diagonal in the 3D cuboids.

layer	nodes per wavelength: x	y	z	ø
screen B	19.0	19.0	19.0	11.2
screen A	19.1	19.1	19.1	11.2
felt B	20.2	20.2	20.2	11.9
felt A	14.4	14.4	14.4	8.5
resistive screen	3.2	3.2	32.1	2.3
air	8.6	8.6	8.6	5.0

4.1.2 Measurements

Extensive preparations to measure the diffuse sound transmission loss of the noise shield in the reverberation room at Chalmers were made. These measurements could not be carried out due to *force majeure*. A detailed planning of the required double wall construction for these measurements can be found in Appendix E.

4.2 Results

In this section, the results of the sound transmission loss simulations are presented.

4.2.1 Plane wave normal incidence (2D models)

The transmission loss for plane wave normal incidence has been calculated for the models v1, v2, v6 and v7 as specified in Table 3.8 with the model setup described in Section 4.1.1.1.[1] Please note that model v1 in this and the following investigations is always modelled with a decreased porosity in the TMM simulations ($\phi = 10^{-5}$, as determined from the results shown in Figure 3.14) unless indicated otherwise. The results are shown in Figure 4.4 and 4.5. It can be seen that model v2, which has been ruled out for the absorption coefficient calculation because of its poor match to the measured data, also behaves differently than the other three models in the transmission case. Under the assumption that models which yield valid results for the absorption coefficient (which is the case for models v1, v6 and v7 – but not v2) also yield valid results for the transmission loss, this suggests that model v2 is not suitable for modelling the sound transmission loss. This indicates that also for modelling the sound transmission loss the inclusion of visco-thermal dissipation in the resistive screen is to be avoided. For the remaining three approaches, it can be seen that for none of them the TMM and FEM results match perfectly but the general shape of the transmission loss curves is well predicted. The best fit is observed for model v7. In model v6 the TMM and FEM results match very well from 500 Hz upwards while there are higher deviations at low frequencies. For model v1 it can be observed that in congruence with the

[1]The perforated plate models v3, v4 and v5 were not investigated again due to the previously described erroneous results obtained from the perforated plate elements in Actran 2020.

results of the absorption simulations, the porosity value in the TMM model has to be decreased to match to the FEM simulations. The obtained results have to be evaluated under consideration of the results presented in Section 3.3.1.6. These show that also for the absorption the best match between the FEM and TMM results can be observed for model v7 which, however, does not match as well to the measurements as model v6 below 300 Hz. As a reminder (compare Table 3.8), the difference between models v6 and v7 is that in model v6 the elasticity of the screens is included, while the screens are modelled as limp in model v7. This causes that for model v7 the frequencies at which the prominent peaks in the absorption coefficient at low frequencies appear do not match to the measured data as well as for model v6.[2] Since this does not seem to be relevant for the sound transmission loss (compare Figure 4.4), model v7 is chosen for further analyses because of the better agreement between the TMM and FEM results and because of the reduced amount of degrees-of-freedom in the FEM model when modelling the screens as limp.

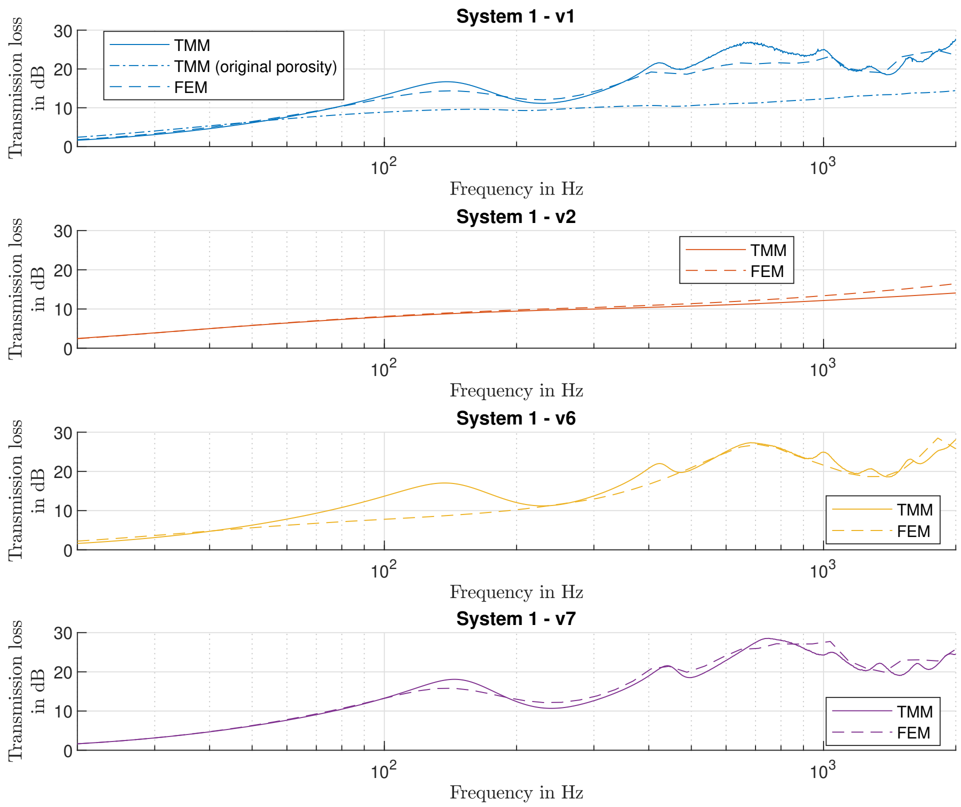

Figure 4.4: Transmission loss for plane wave normal incidence in 2D FEM models compared to TMM results. The version numbers v1 - v7 correspond to the models specified in Table 3.8.

[2]Note that, strictly speaking, these peaks appear in a frequency range where the measured data is not valid.

Figure 4.5 shows that the deviations between the different FEM models are higher than between the different TMM models. The values predicted by both methods are in about the same range but at single frequencies there occur differences of up to 10 dB. Since there is no measured data for the transmission loss available, these results cannot be experimentally validated. It shows, however, that, depending on the hypotheses of the modelling approach, the results can be quite different. In the FEM results, it seems like the differences decrease with increasing frequency. The larger differences at low frequencies could be due to local elastic resonance effects.

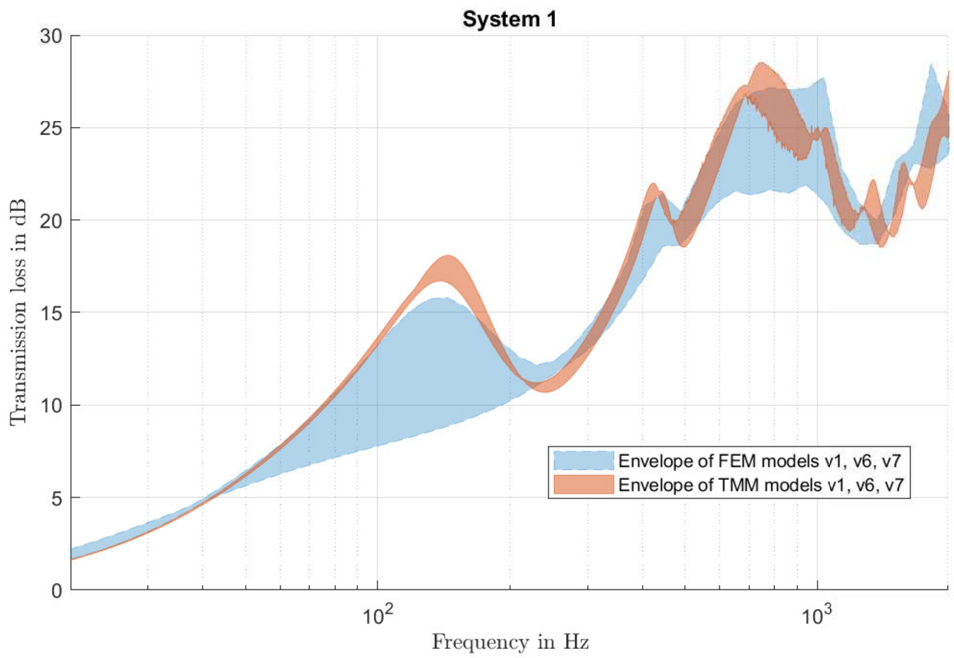

Figure 4.5: Transmission loss for plane wave normal incidence in 2D FEM models compared to TMM results. This plot shows the envelope of the curves shown in Figure 4.4. Please note that the observed differences are only due to different hypotheses in the different models and not due to different material parameters or similar.

4.2.2 Mesh size sensitivity study for plane wave normal incidence (2D models)

The transmission loss for plane wave normal incidence is calculated for model v7 (Table 3.8) with different mesh sizes. The mesh size is generally the same for all layers but the mesh size of the individual layers is bounded by their thickness, i.e. there are at least two nodes per layer (one on each surface). The results obtained for the transmission loss for different mesh sizes (between 0.1 mm and 25 mm) are shown in Figure 4.6. The mean and maximum deviations to the result obtained with the finest chosen mesh size are listed in Table 4.6.

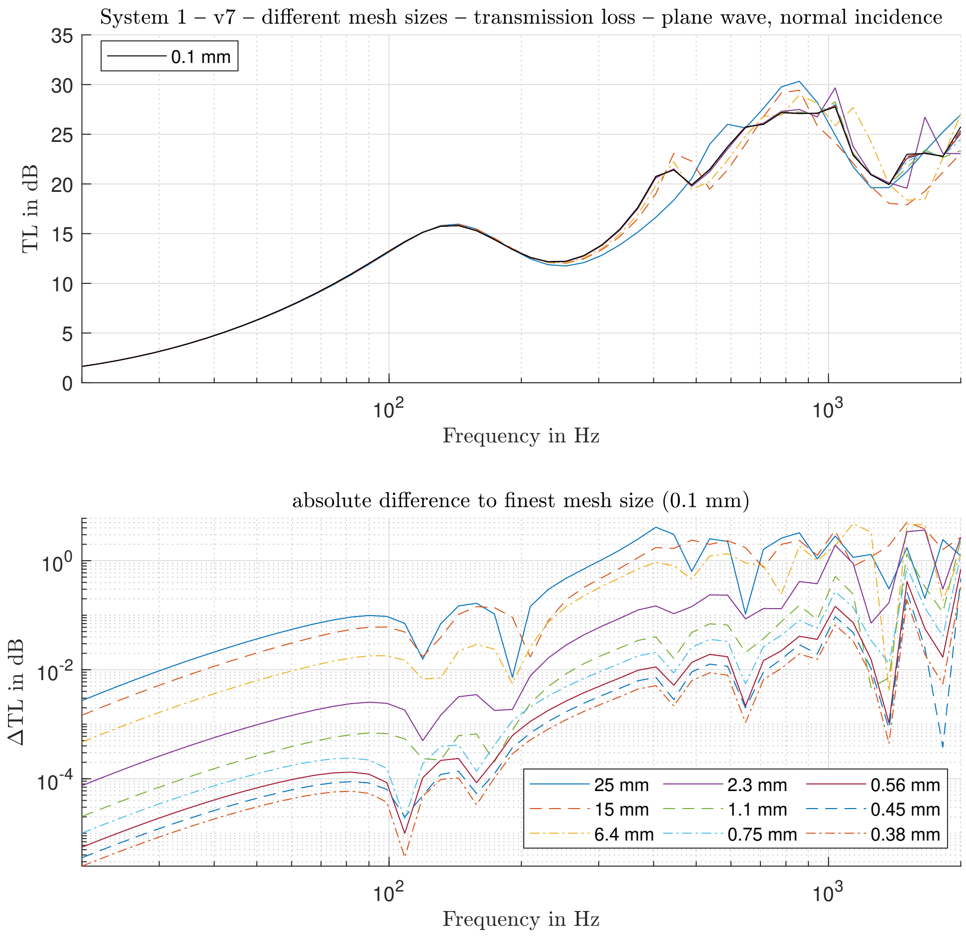

Figure 4.6: Transmission loss for normally incident plane waves with model v7, using different mesh sizes.

Table 4.6: Deviation of the transmission loss for different mesh sizes from the finest mesh size (0.1 mm). Compare Figure 4.6.

mesh size	mean deviation (in dB)	maximum deviation (in dB)
25 mm	0.81	4.12
15 mm	0.86	5.09
6.4 mm	0.65	4.81
2.3 mm	0.31	3.65
1.1 mm	0.11	2.39
0.75 mm	0.06	1.26
0.56 mm	0.03	0.69
0.45 mm	0.02	0.47
0.38 mm	0.01	0.33

As expected, the deviation of the calculated transmission loss to the result obtained with the finest chosen mesh size (0.1 mm) generally increases with increasing mesh size. As the result with a mesh size of 0.38 mm is still different from the result at 0.1 mm, it shows that at this resolution the model has not fully converged. However, the maximum deviation from the finest resolution is below 1 dB for mesh sizes of 0.56 mm and lower. To determine the deciding factors for the convergence behaviour and to determine, which number of elements per wavelength can be considered as sufficient, the number of elements per wavelength is plotted as a function of the frequency and the mesh size in Figure 4.7 and 4.8 for the two felts. The horizontal lines in these plots indicate the actual mesh size along with the thickness, which is different from the defined mesh size when the thickness is smaller than the defined mesh size. In this analysis, only the mesh size along the thickness is considered because this is the main propagation direction for normally incident plane waves. Furthermore, because of dealing with normally incident plane waves, the influence of the shear wave is expected to be negligible.

As an example of an analysis, the behaviour with the biggest mesh size (25 mm) is investigated. For this mesh size, it can be observed that the first frequency at which the deviation from the result with 0.1 mm mesh size exceeds 1 dB is around 300 Hz. The number of elements per wavelength shown in Figure 4.7 and 4.8 is represented in a clearer form just for this mesh size in Figure 4.9.[3] The numbers of elements per wavelength at 300 Hz are given in Table 4.7. It is interesting to note that the shear wave is described almost as accurately as the fast compressional wave.

Table 4.7: Number of elements per wavelength in propagation direction of the normally incident plane wave at 300 Hz for mesh sizes of 25 mm in felt B and 4.1 mm in felt A, respectively. Compare Figure 4.9.

	felt A	felt B
shear wave	7.4	1.7
compressional wave 1	10.7	2.4
compressional wave 2	29.3	15.5

When assuming that the shear wave is of negligible importance in this case, it can be observed that the remaining numbers of elements per wavelength are in a range which is probably sufficient, apart from the compressional wave in felt B. The low resolution for the first compressional wave in felt B is probably the reason why the model starts to break down at this frequency with this mesh size.

Going up slightly higher in frequency, to 400 Hz, where the errors are higher but still in the same clearly defined order as for 300 Hz (compare Figure 4.6), it is investigated, which numbers of elements per wavelength for the two compressional waves lead to which deviations in the calculated transmission loss from the result with the finest mesh size (Table 4.8).

[3] Please observe that for felt A a mesh size of 4.1 mm instead of 25 mm is investigated due to the thickness of this layer which is prohibiting bigger mesh sizes in the propagation direction of the normally incident plane wave, which is investigated here.

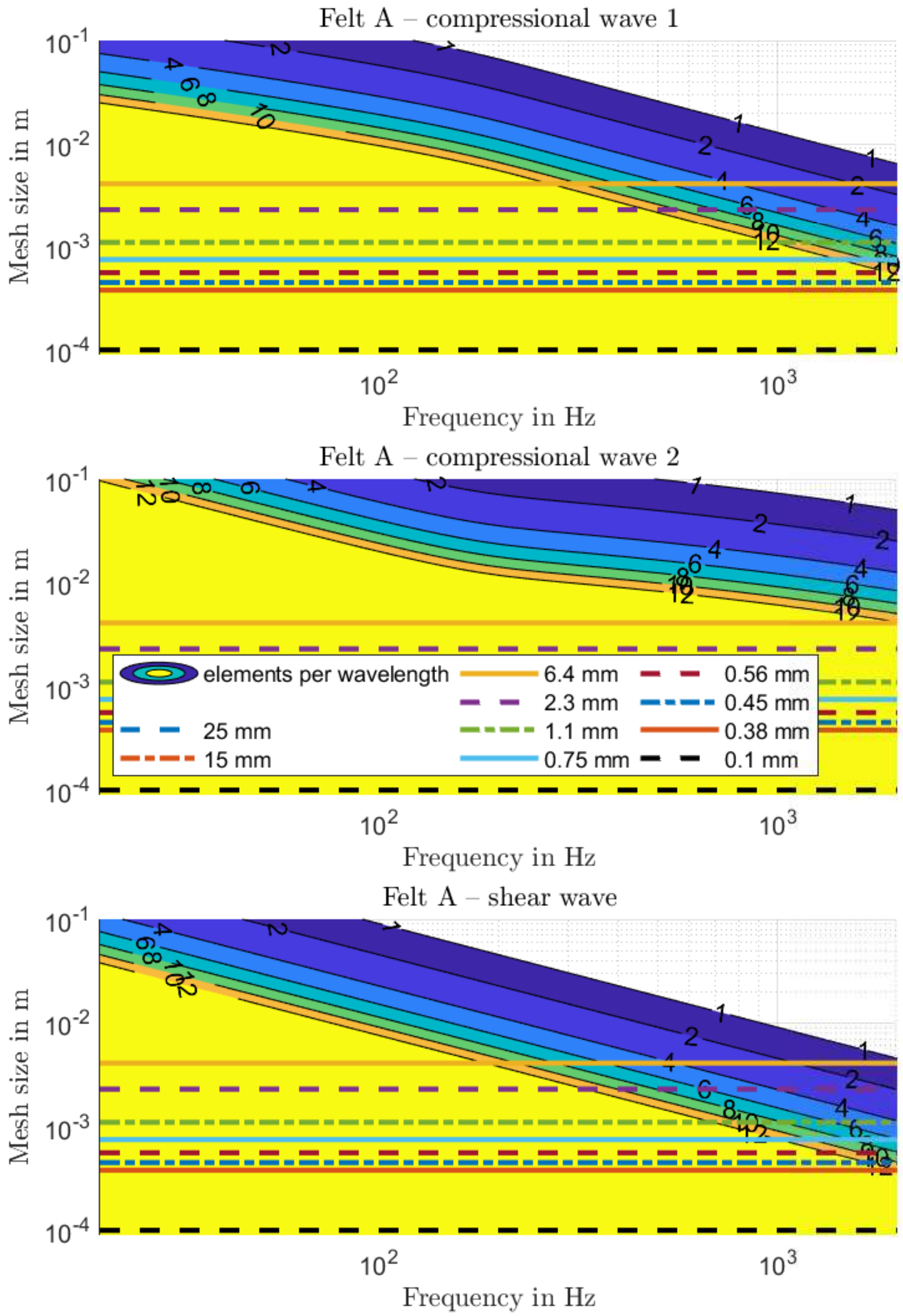

Figure 4.7: Number of elements per wavelength (along the propagation direction of the normal incident plane wave) for different mesh sizes for **felt A**. The lines indicate the effective mesh sizes.

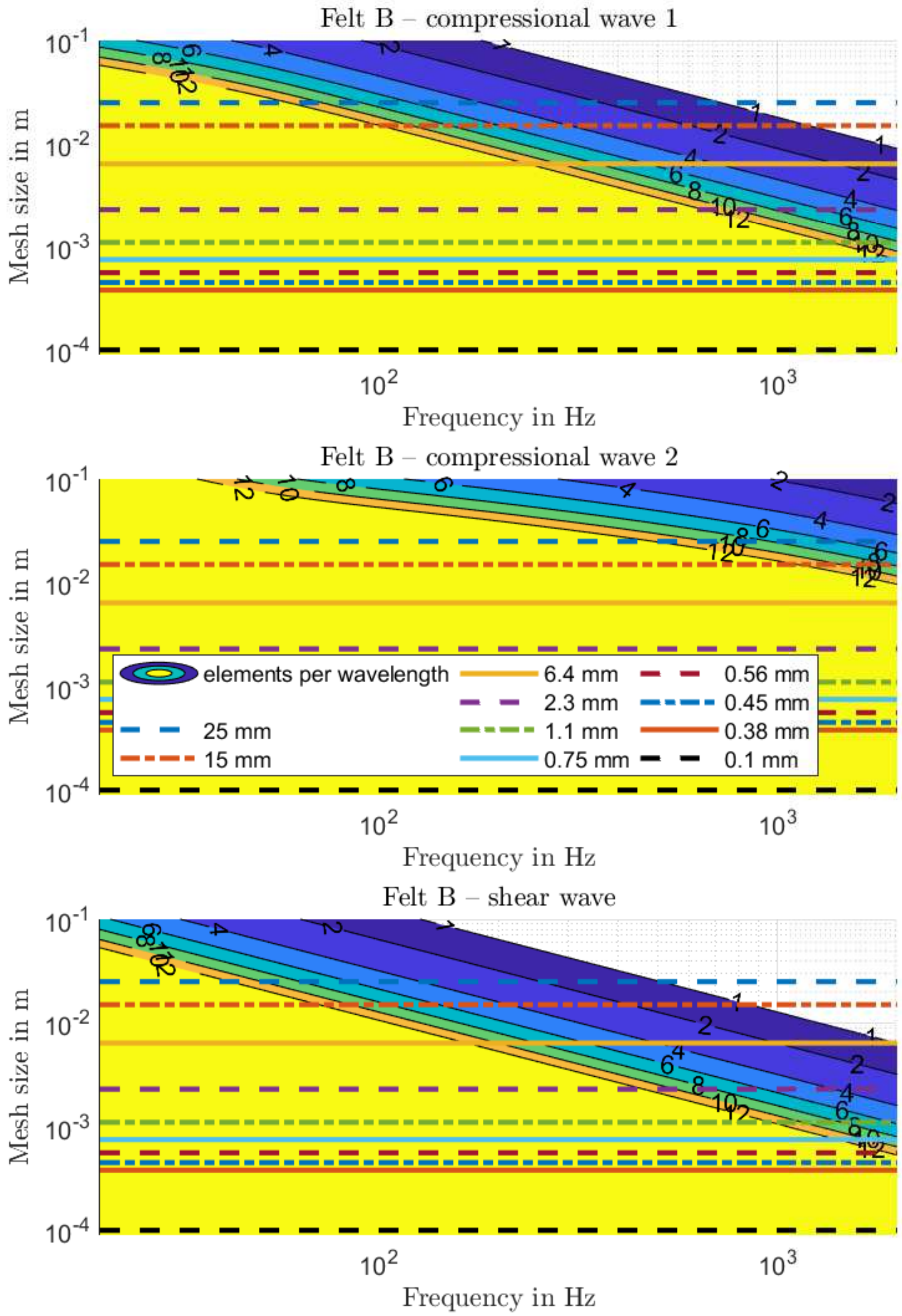

Figure 4.8: Number of elements per wavelength (along the propagation direction of the normal incident plane wave) for different mesh sizes for **felt B**. The lines indicate the effective mesh sizes.

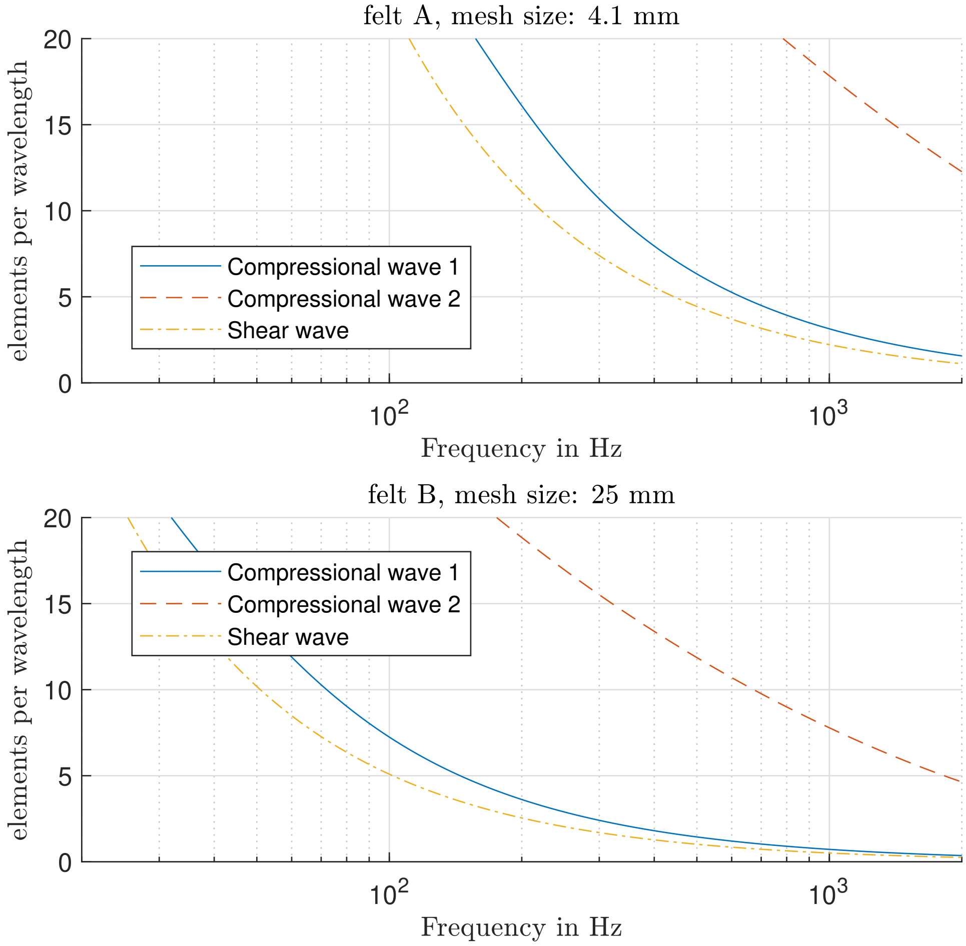

Figure 4.9: Number of elements per wavelength in propagation direction of the normally incident plane wave for a defined mesh size of 25 mm. This can be seen as a cut through Figure 4.7 and 4.8 for this specific mesh size. The speeds of sound in the two felts are shown in Figure C.1.

Table 4.8 shows a study on the error at 400 Hz for different mesh sizes, depending on the number of elements per wavelength for the two compressional waves in felt A and felt B. For the three coarsest meshes it shows that the resolution of the first compressional wave (*fluid wave*) in felt B is mostly responsible for the high errors. Once the two compressional waves in both felts are meshed with at least 7 elements per wavelength, the error becomes smaller than 1 dB. Since this observation matches to the common criteria which are usually used in FEM modelling (6 or 7 elements per wavelength for convergence), it is concluded that these criteria are also valid in this case, although it is stated in [2] that 6 elements per wavelength are not sufficient for poroelastic materials and that (in special cases) up to 12 elements may be needed for convergence (compare Section 2.3.2.1). In addition to this, it can also be noted that, as expected, in this case for normally incident plane waves the shear wave is of minor importance, as an error below 1 dB is already reached when the shear wave in felt B is still captured with less than 5 elements per wavelength.

Table 4.8: Number of elements per wavelength (in propagation direction of the normally incident plane wave) and resulting error (deviation from the calculated transmission loss with a mesh size of 0.1 mm) at 400 Hz for the three different wave types in the two felts. Compare Figure 4.6, 4.7 and 4.8. The mesh size values given in brackets specify the value for felt A, when different from the value for felt B.

wave type	mesh size	elements / wavelength felt A	elements / wavelength felt B	error
compressional 1		7.8	1.8	
compressional 2	25 mm (4.1 mm)	26.3	13.3	4.12 dB
shear		5.5	1.3	
compressional 1		7.8	3.0	
compressional 2	15 mm (4.1 mm)	26.3	22.2	1.74 dB
shear		5.5	2.1	
compressional 1		7.8	7.0	
compressional 2	6.4 mm (4.1 mm)	26.3	52.0	0.93 dB
shear		5.5	4.9	
compressional 1		14.0	19.4	
compressional 2	2.3 mm	46.8	144.6	0.15 dB
shear		9.8	13.7	
compressional 1		29.3	40.5	
compressional 2	1.1 mm	97.9	302.5	0.04 dB
shear		20.4	28.6	

4.2.3 Plane wave normal incidence (3D models with increased Young's modulus)

As for the 3D absorption models, the 3D transmission models are created with an increased Young's modulus for all layers (factor of ten). The TMM and FEM results for normally incident plane waves are shown in Figure 4.10. It can be seen that, as for the 3D absorption, the FEM and TMM results match best for model v7 (compare Table 3.8). Figure 4.11 shows the differences between the different modelling approaches. For both FEM and TMM the differences between the three different modelling approaches exceed 10 dB at 2 kHz. This, again, shows that the general shape of the transmission loss is predicted in the same way for all models but there can be large differences in the predicted values depending on the hypotheses which are made in the modelling.

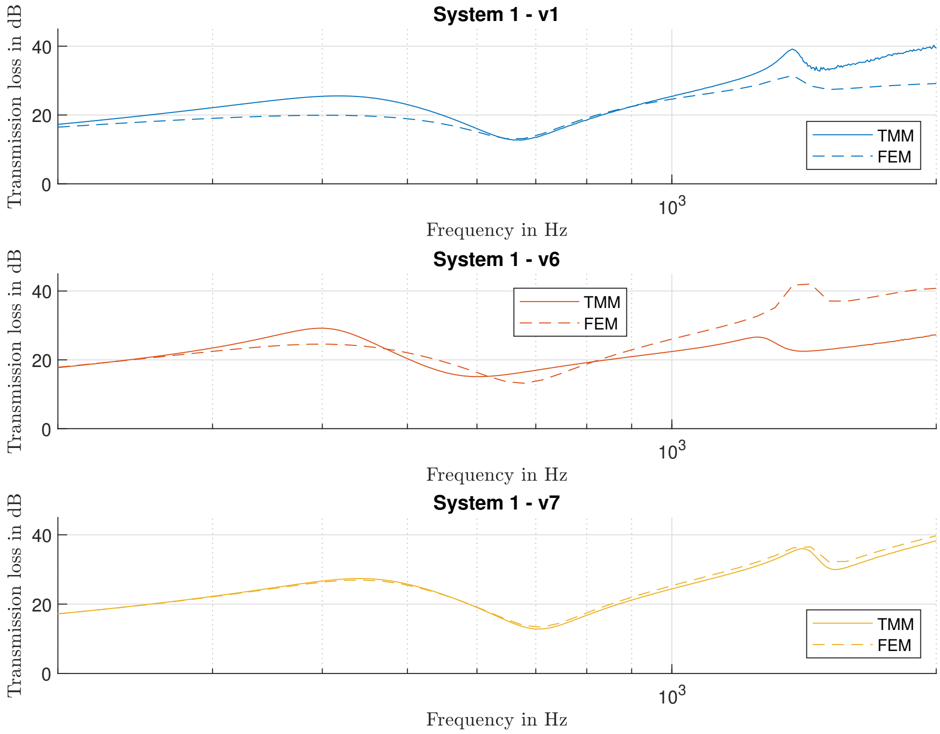

Figure 4.10: Transmission loss for plane wave normal incidence in 3D FEM models compared to TMM results. The version numbers v1 - v7 correspond to the models specified in Table 3.8. Models with **increased Young's moduli**.

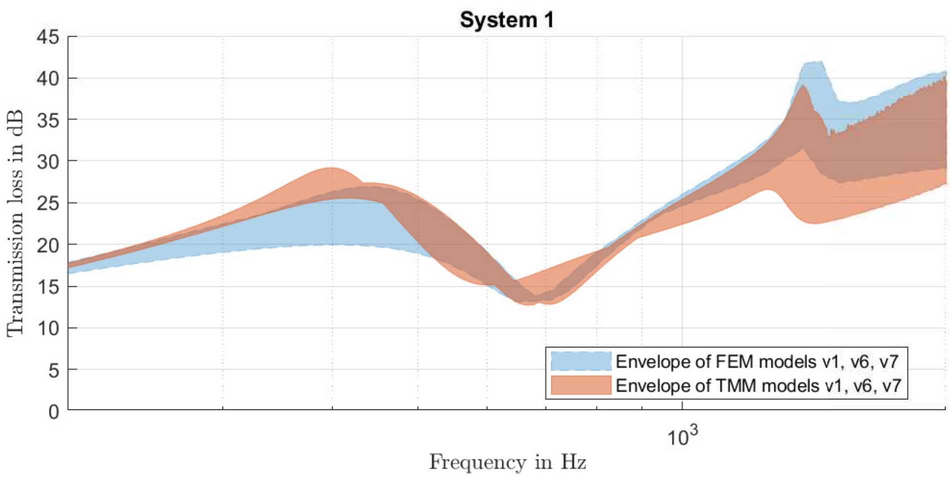

Figure 4.11: Transmission loss for plane wave normal incidence in 3D FEM models compared to TMM results. This plot shows the envelope of the curves shown in Figure 4.10. Please note that the observed differences are only due to different hypotheses in the different models and not due to different material parameters or similar. Models with **increased Young's moduli**.

4.2.4 Diffuse incidence (3D models with original material data)

The calculated transmission loss for TMM and FEM for a 3D model (version with original material data) under diffuse sound incidence (0° - 80°, eliminating grazing incidence) is shown in Figure 4.12 for model versions v1, v6 and v7. Figure 4.13 shows the envelope of the plots in Figure 4.12.

It can be observed that the transmission loss at low frequencies in the FEM result is higher than for the TMM model, due to the finite size (0.01 m^2) of the FEM model. By applying a Bonfiglio finite-size-correction (compare [31]) in the TMM model, it can be accounted for the reduced radiation efficiency at low frequencies. This is assumed to have an influence up to the lowest critical frequency in the system, since above that the radiation efficiency will be close to 1 for both the finite- and infinite-size versions. This finite-size-correction can, however, not account for the influence of the finite-size on the vibrational behaviour, which explains the difference between the FEM and TMM results at low frequencies. At higher frequencies the FEM results become almost identical to the TMM results without finite-size-correction. The highest difference between the different FEM models is 6 dB at 700 Hz.

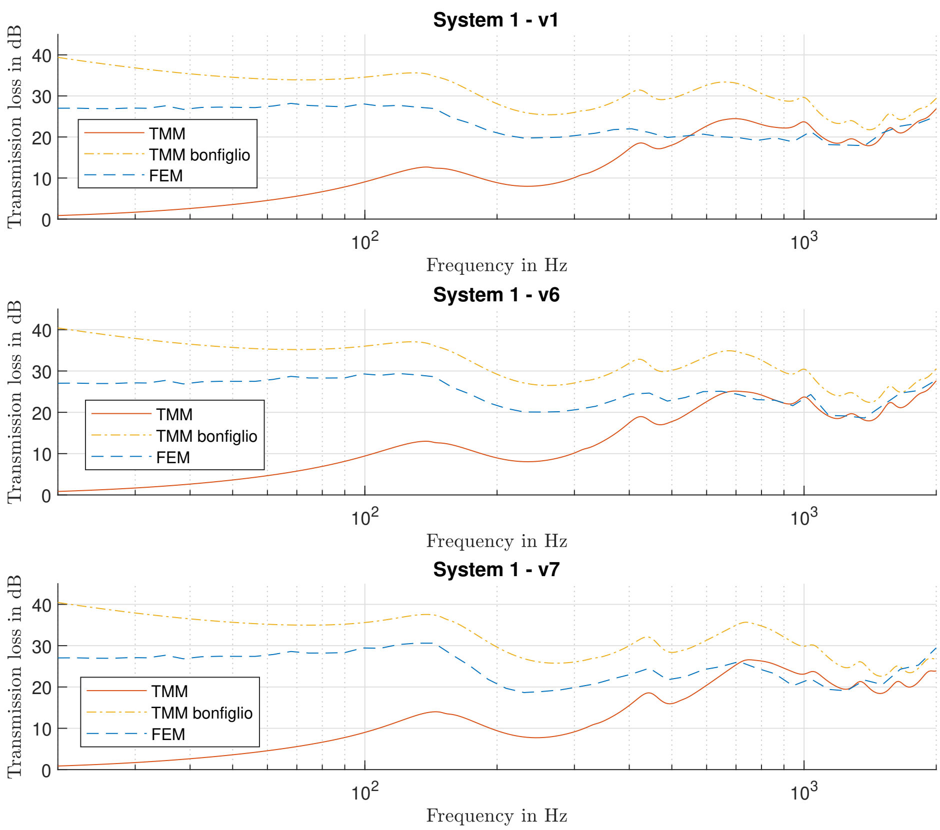

Figure 4.12: Transmission loss for diffuse incidence (0° - 80°) in 3D FEM models compared to TMM results with and without Bonfiglio finite-size-correction. The version numbers v1 - v7 correspond to the models specified in Table 3.8.

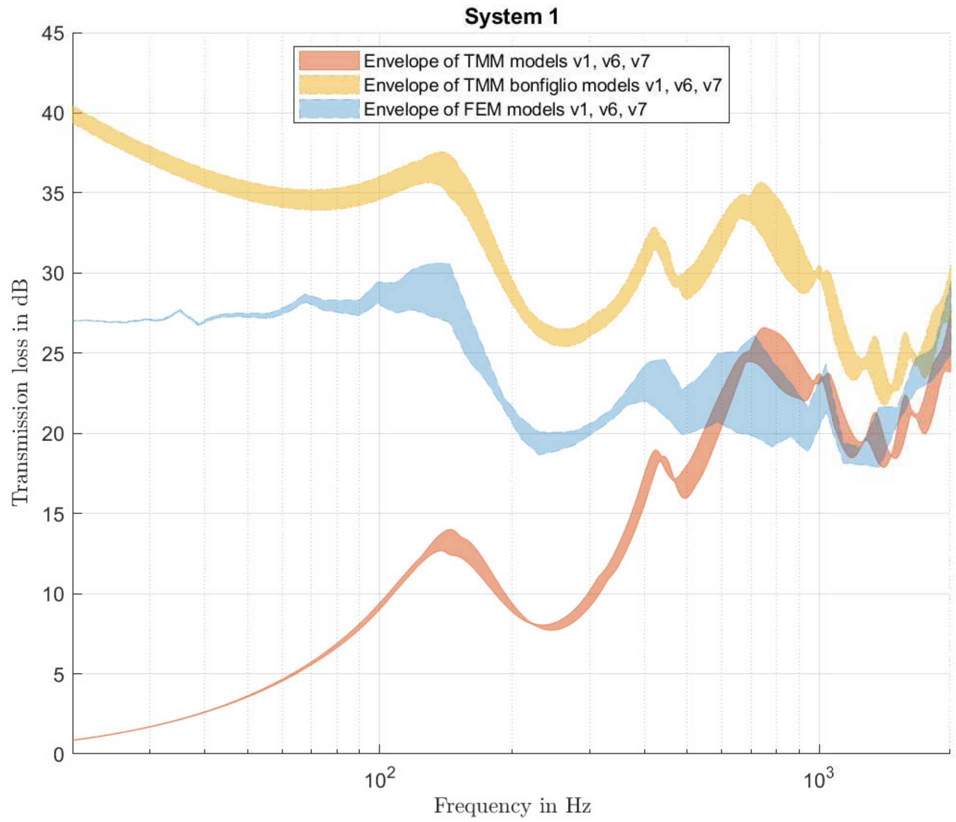

Figure 4.13: Transmission loss for diffuse incidence (0° - 80°) in 3D FEM models compared to TMM results with and without Bonfiglio finite-size-correction. This plot shows the envelope of the curves shown in Figure 4.12. Please note that the observed differences are only due to different hypotheses in the different models and not due to different material parameters or similar.

4.2.5 Diffuse incidence (3D models with increased Young's modulus)

The calculated transmission loss for TMM and FEM for a 3D model (version with increased Young's moduli) under diffuse sound incidence (0° - 80°, eliminating grazing incidence) is shown in Figure 4.14 for model versions v1, v6 and v7. Figure 4.15 shows the envelope of the plots in Figure 4.14.

The shape of the calculated transmission loss is different from the one obtained with the original material data but similar observations can be made. Above 700 Hz, with decreasing influence of finite-size effects, the TMM and FEM results are almost identical, especially for models v6 and v7. For model v1 the calculated transmission loss at the upper limit of the investigated frequency range is 10 dB lower in the FEM results than in the TMM results. Figure 4.14 shows that the different FEM models have very little deviations at low frequencies where the transmission loss is mostly governed by the size of the sample. At higher frequencies, the deviations exceed 10 dB.

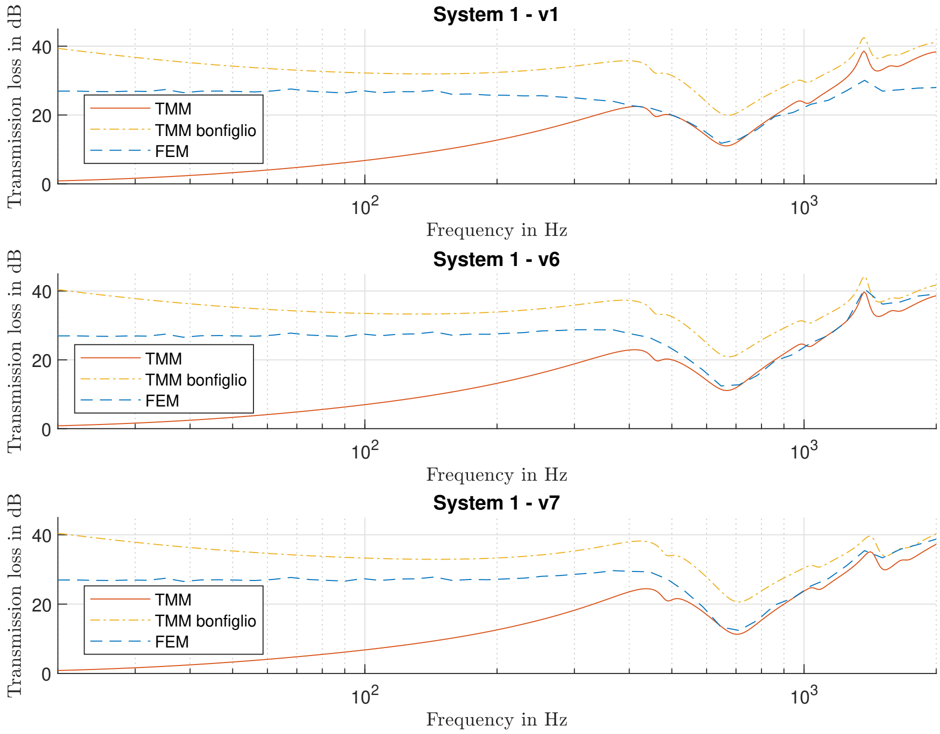

Figure 4.14: Transmission loss for diffuse incidence (0° - 80°) in 3D FEM models compared to TMM results with and without Bonfiglio finite-size-correction. The version numbers v1 - v7 correspond to the models specified in Table 3.8. Models with **increased Young's moduli**.

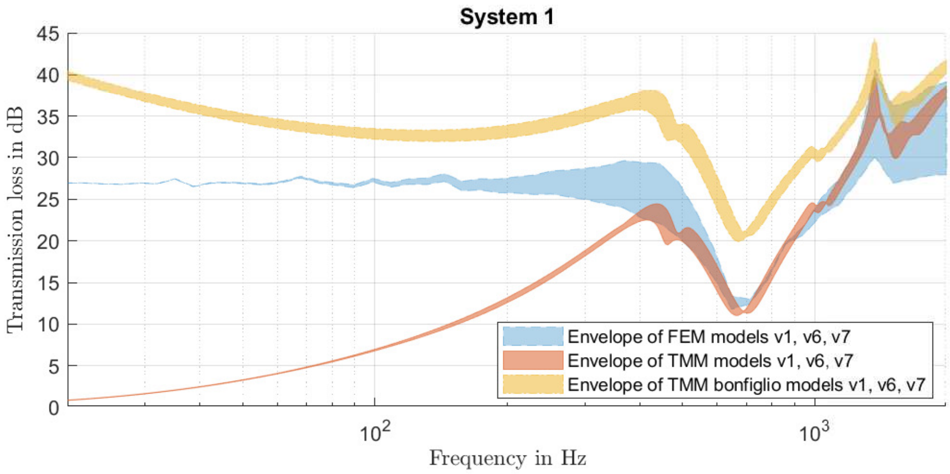

Figure 4.15: Transmission loss for diffuse incidence (0° - 80°) in 3D FEM models compared to TMM results with and without Bonfiglio finite-size-correction. This plot shows the envelope of the curves shown in Figure 4.14. Please note that the observed differences are only due to different hypotheses in the different models and not due to different material parameters or similar. Models with **increased Young's moduli**.

4.2.6 Influence of parameter variation

Figure 4.16 shows a comparison of the calculated transmission losses with original and increased Young's moduli. Figure 4.17 shows the difference between the calculated transmission losses. It can be seen that there is a very good agreement between the TMM, TMM Bonfiglio and FEM predictions on the effect of changing the Young's moduli for model v6 and a good agreement for model v7. The agreement for model v1 is worse. Since it has already been shown earlier that poroelastic modelling of the resistive screen (as in model v1) leads to differences between the different modelling approaches, this result is not unexpected.

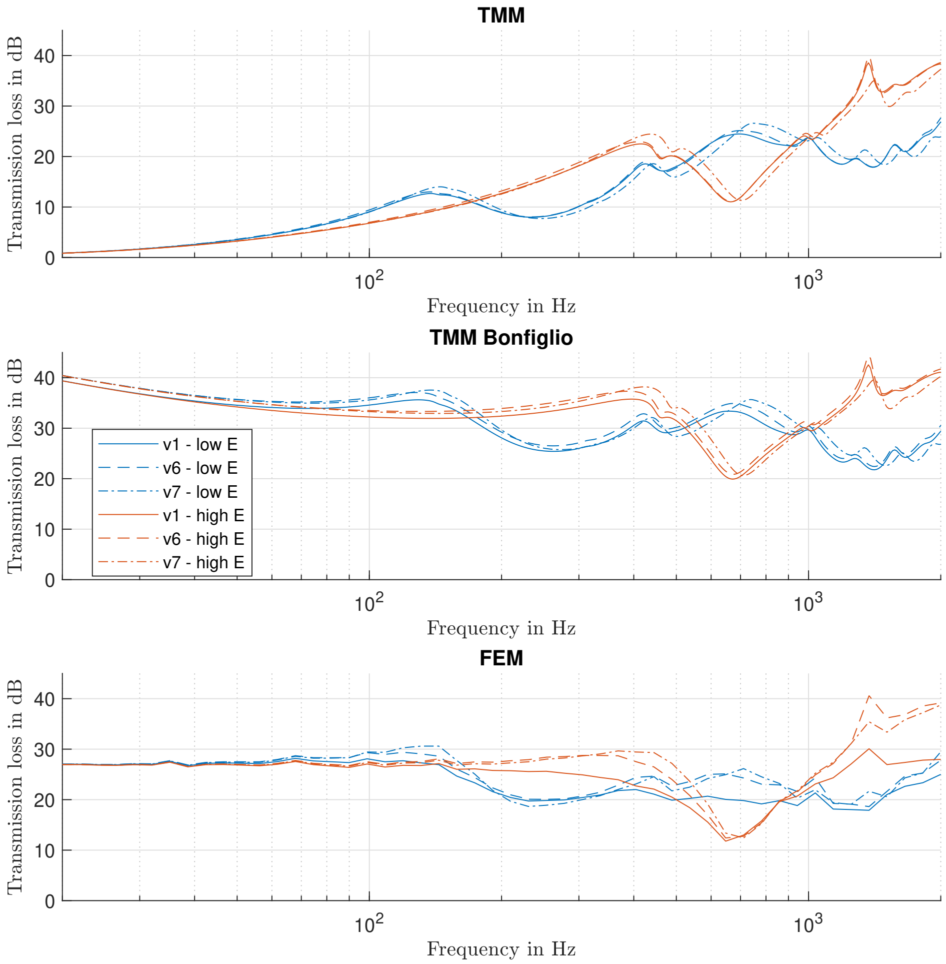

Figure 4.16: Comparison of calculated transmission losses with original (low E) and increased (high E) Young's moduli.

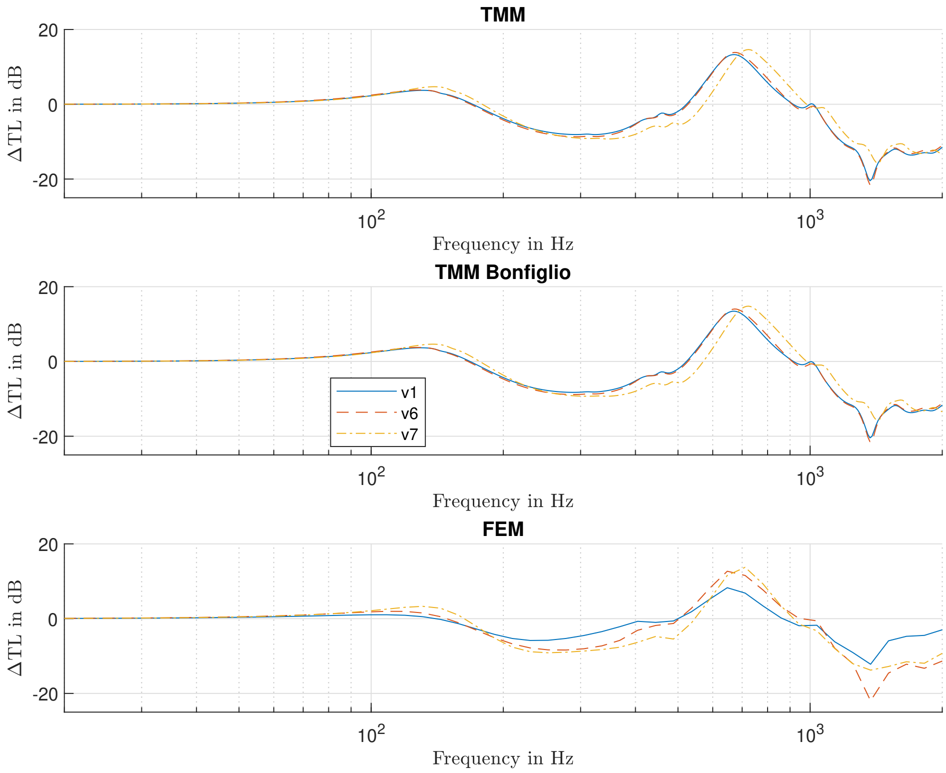

Figure 4.17: Difference between the calculated transmission losses with original and increased Young's moduli.

4.2.7 Mesh size sensitivity study for diffuse sound incidence (3D models with increased Young's modulus)

The transmission loss for diffuse incidence (0° - 80°) has been calculated for model v7 (Table 3.8) with different mesh sizes. For the sensitivity study, the version with increased Young's moduli is used. The distances between the nodes within the sample are generally defined to be the same in all three dimensions and for all layers. However, since the distance between the nodes along the thickness of the individual layers cannot be bigger than the thickness of the individual layers, the maximum node distance in this direction has an upper limit. For defined node distances bigger than the thickness of individual layers this results in a cuboid rather than a cubic arrangement of the nodes in the mesh. The diagonal mesh size is dependent on the layer and calculated as the diagonal of these cuboids (and, therefore, up to a factor of $\sqrt{3}$ larger than the defined node distance).[4] The results obtained for the transmission loss for different defined node distances (between 1 mm and 20 mm) are shown in Figure 4.18. The mean and maximum deviations to the result obtained with the smallest chosen node distance are listed in Table 4.9.

[4]These considerations are in contrast to the investigation carried out for normally incidence plane waves in 2D, where only the mesh size along the thickness is considered.

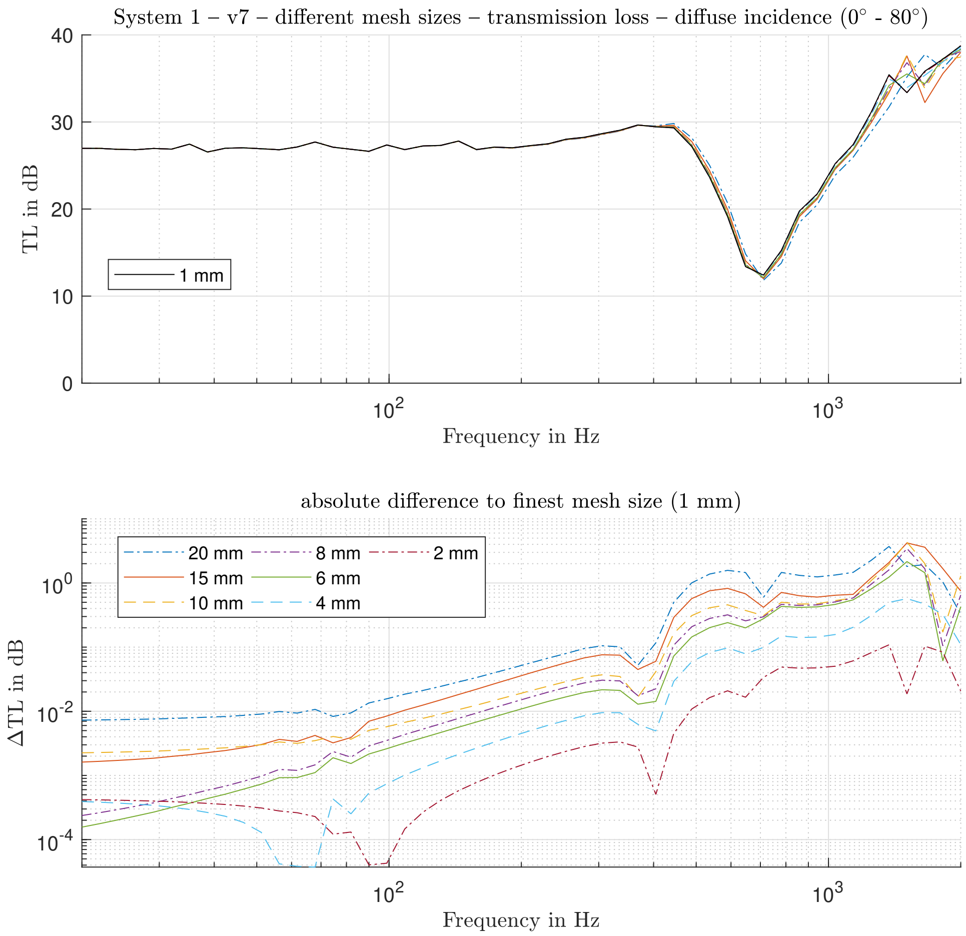

Figure 4.18: Transmission loss for diffuse incidence (0° - 80°) with model v7 (**increased Young's moduli**), using different mesh sizes.

Table 4.9: Deviation of the transmission loss for different defined mesh sizes from the finest mesh size (1 mm) in the range from 20 Hz to 2 kHz. Compare Figure 4.18.

mesh size	mean deviation (in dB)	maximum deviation (in dB)
20 mm	0.51	3.71
15 mm	0.42	4.21
10 mm	0.32	4.33
8 mm	0.25	3.45
6 mm	0.19	2.15
4 mm	0.07	0.57
2 mm	0.02	0.12

From Figure 4.18 it can be seen that the calculated transmission loss follows the same shape for all investigated mesh sizes but the deviations between the results obtained with different mesh sizes are higher at higher frequencies. Table 4.9 shows that the deviations between the mesh sizes 1 mm and 2 mm are ≤ 0.12 dB (0.02 dB in average) in the frequency range from 20 Hz to 2 kHz which indicates that at this mesh size the results have sufficiently converged. This legitimates the use of the results with 1 mm mesh size as reference. As expected, the deviations from this reference result are generally increasing with increasing mesh size and increasing frequency. Figure 4.19 and 4.20 provide more detailed information about the number of elements per wavelength in the two felts at each frequency and for each mesh size. The legend entries in Figure 4.19 and 4.20 refer to the defined distance between the nodes[5] while the associated lines in the plot show the diagonal mesh size (diagonal of the cuboid grid).

Similarly as for the convergence study with the normally incident plane wave in 2D, it is also in this case investigated more in detail, what number of elements per wavelength for the different wave types are required to achieve which error. As a reminder, in the 2D study shear waves are considered as negligible and only the mesh size in the propagation direction of the normally incident plane wave is considered. In contrast to that, in the 3D study with a diffuse incident sound field, all three wave types and the mesh size in all three dimensions is considered. Based on the results shown in Figure 4.18 a frequency of 1.25 kHz is chosen for this example analysis. The numbers of elements per wavelength for the different mesh sizes are listed in Table 4.10.

Table 4.10: Number of elements per wavelength and resulting error (deviation from the calculated transmission loss with a mesh size of 1 mm) at 1.25 kHz for the three different wave types in the two felts with **increased Young's moduli**. Compare Figure 4.18, 4.19 and 4.20. The given mesh sizes are the diagonal mesh size for felt A and felt B and the defined distance between the nodes in the cuboid grid (in brackets). The normal of the sample surface is parallel to the z-axis. The ø columns represent the number of elements per wavelength along the diagonals of the cuboid grid.

wave type	mesh size	elements / wavelength felt A			felt B		error
		x/y	z	ø	x/y/z	ø	
compressional 1		1.66	8.1	1.16	2.28	1.32	
compressional 2	28.6 mm / 34.6 mm / (20 mm)	3.19	15.58	2.24	8.32	4.80	2.25 dB
shear		1.15	5.61	0.81	1.61	0.93	
compressional 1		2.22	8.1	1.54	3.05	1.76	
compressional 2	21.6 mm / 26 mm / (15 mm)	4.26	15.58	2.96	11.1	6.41	1.20 dB
shear		1.53	5.61	1.07	2.15	1.24	
compressional 1		3.32	8.1	2.26	4.57	2.64	
compressional 2	14.7 mm / 17.3 mm / (10 mm)	6.39	15.58	4.34	16.64	9.61	1.10 dB
shear		2.30	5.61	1.56	3.22	1.86	
compressional 1		4.15	8.1	2.76	5.71	3.30	
compressional 2	12 mm / 13.9 mm / (8 mm)	7.99	15.58	5.31	20.81	12.01	0.95 dB
shear		2.88	5.61	1.91	4.03	2.33	
compressional 1		5.54	8.1	3.53	7.62	4.40	
compressional 2	9.4 mm / 10.4 mm / (6 mm)	10.65	15.58	6.77	27.74	16.02	0.80 dB
shear		3.84	5.61	2.44	5.37	3.10	
compressional 1		8.31	8.31	4.80	11.42	6.59	
compressional 2	6.9 mm / 6.9 mm / (4 mm)	15.97	15.97	9.22	41.61	24.02	0.31 dB
shear		5.75	5.75	3.32	8.06	4.65	
compressional 1		16.61	16.61	9.59	22.85	13.19	
compressional 2	3.5 mm / 3.5 mm / (2 mm)	31.94	31.94	18.44	83.22	48.05	0.08 dB
shear		11.51	11.51	6.64	16.12	9.31	
compressional 1		33.23	33.23	19.18	45.69	26.38	
compressional 2	1.7 mm / 1.7 mm / (1 mm)	63.88	63.88	36.88	166.44	96.10	/
shear		23.01	23.01	13.29	32.24	18.61	

[5] Where possible, the distance is the same in all three dimensions.

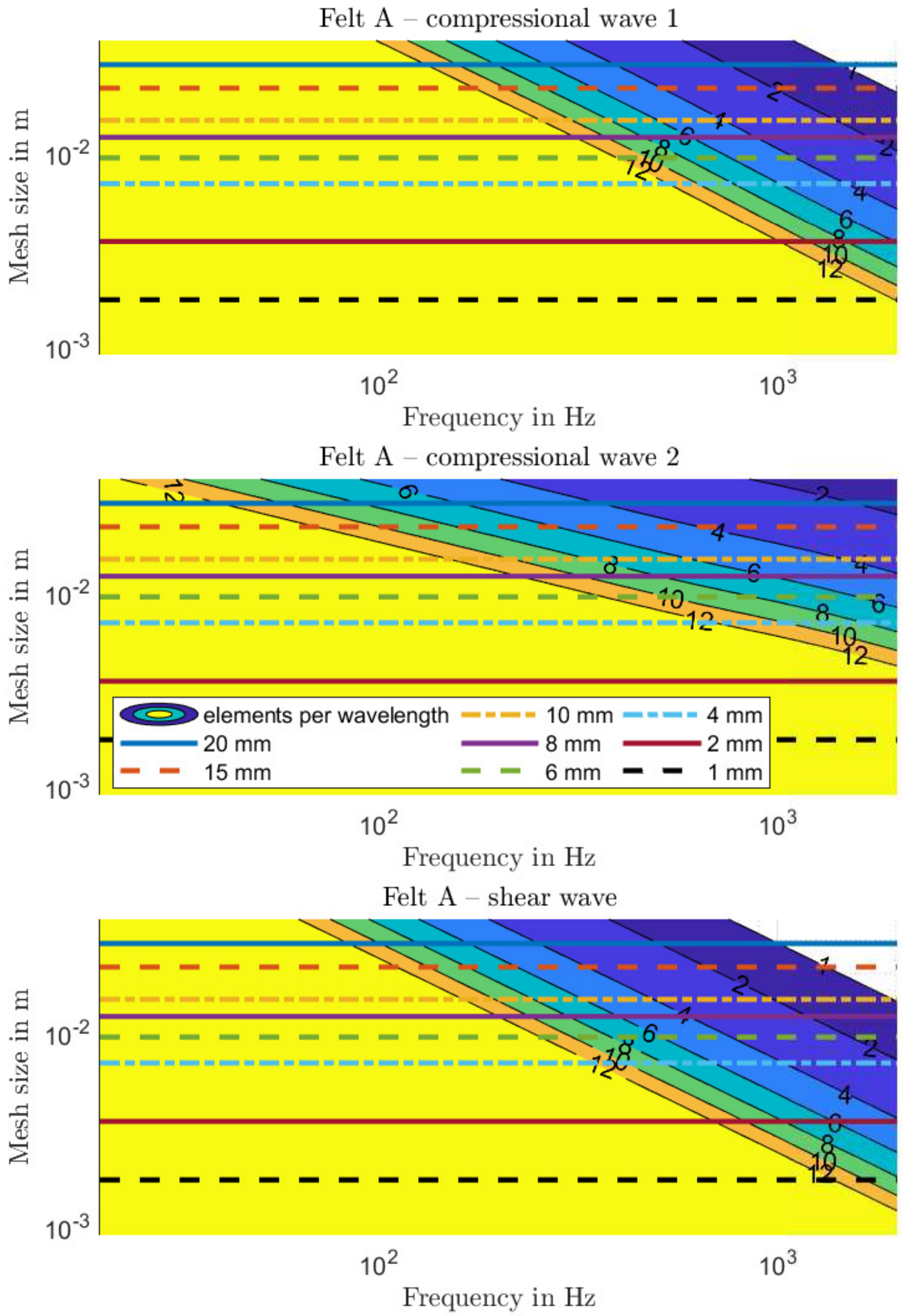

Figure 4.19: Number of elements per wavelength for different mesh sizes for **felt A** (**increased Young's modulus**). The lines indicate the diagonal mesh sizes.

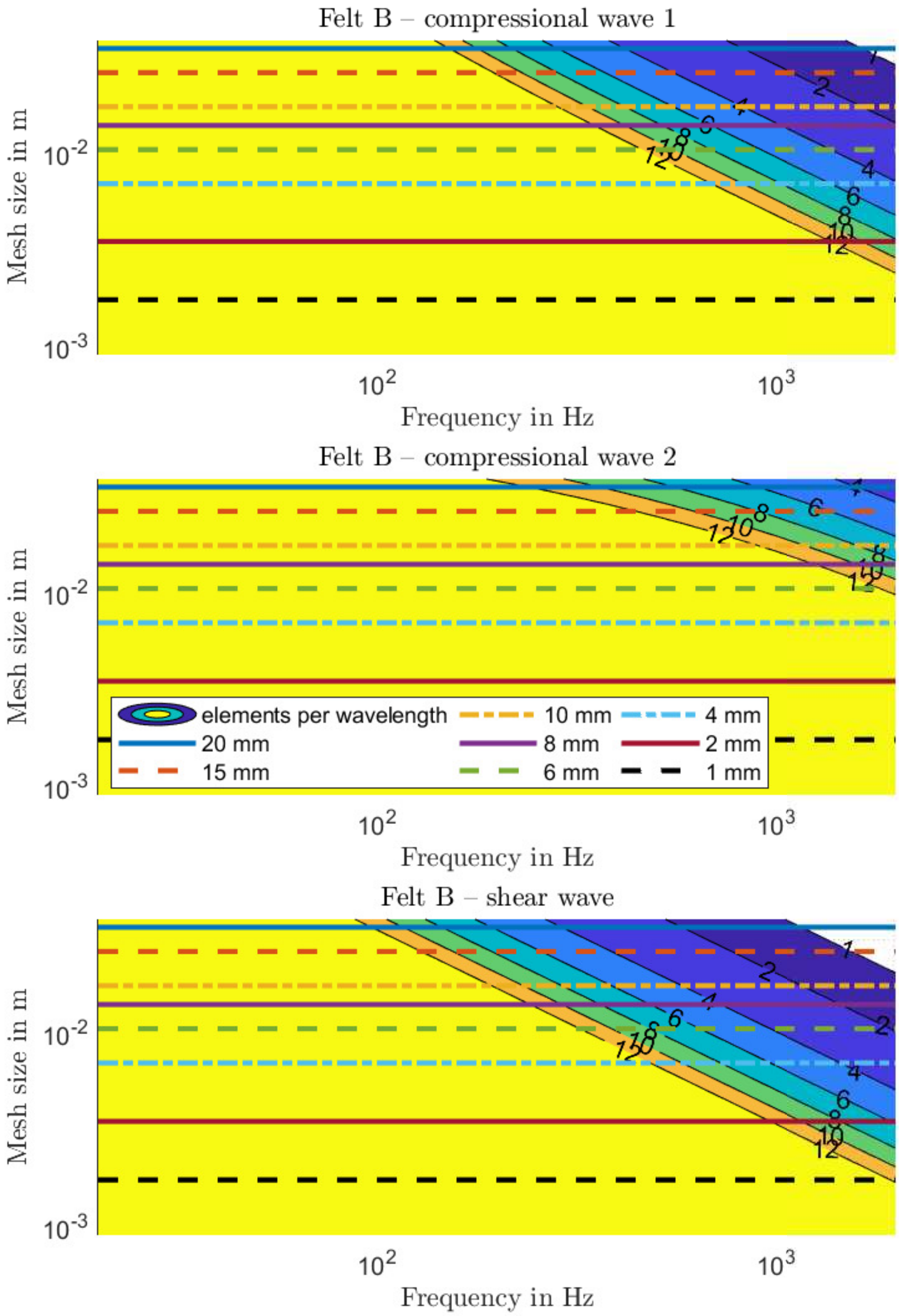

Figure 4.20: Number of elements per wavelength for different mesh sizes for **felt B** (**increased Young's modulus**). The lines indicate the diagonal mesh sizes.

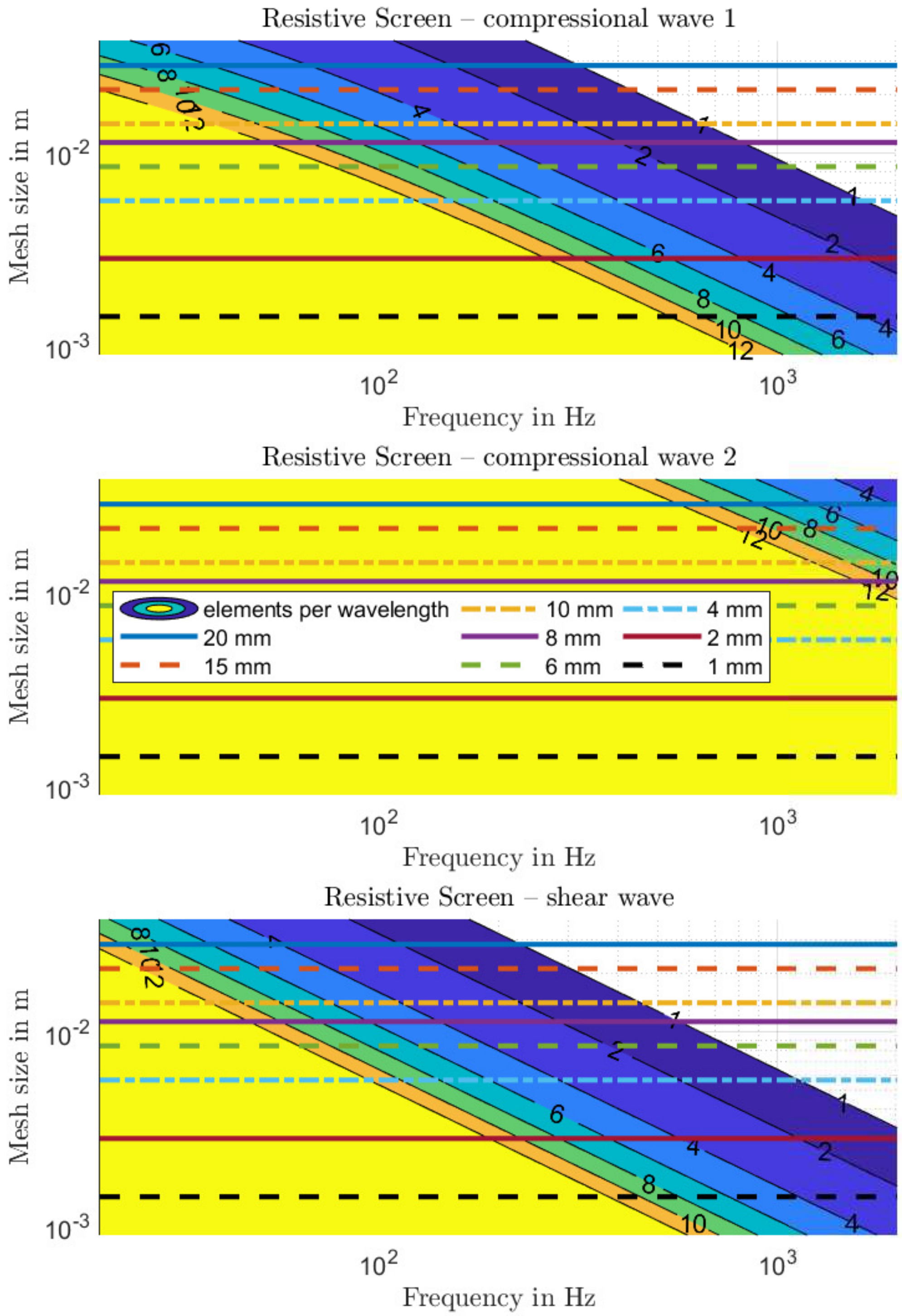

Figure 4.21: Number of elements per wavelength for different mesh sizes for the **resistive screen** (**increased Young's modulus**). The lines indicate the diagonal mesh sizes.

When considering an error ≤ 1 dB as sufficiently small, it can be observed from Table 4.10 that at 1.25 kHz this criterion is reached with a defined node distance of 8 mm. At this mesh size, the 12 elements per wavelength criterion is only fulfilled for some wave types in some dimensions. In fact, only the second compressional wave (*solid wave*) is sampled with more than 6 elements per wavelength in x-, y- and z-direction in both felts. The shear wave is sampled with less than 6 elements in all dimensions and the first compressional wave (*fluid wave*) only reaches above 6 elements per wavelength for felt A in z-direction. With a node distance of 4 mm, for which an error of 0.31 dB is reached, the second compressional wave is sampled with more than 12 elements per wavelength in both felts in all dimensions, the first compressional wave is sampled with more than 8 elements per wavelength in both felts in all dimensions and the shear wave is sampled with almost 6 elements per wavelength in felt A and more than 8 elements per wavelength in felt B. These results indicate that following the general rule of thumb of having at least 6 elements per smallest wavelength also in this case leads to errors significantly below 1 dB. It should be noted that only the two thickest layers of the five-layer assembly are considered here. Figure 4.21 shows that the first compressional and the shear wave in the resistive screen are not sampled with sufficiently high precision according to this criterion with a mesh size of 4 mm at 1.25 kHz. However, it can be assumed that due to the negligible stiffness of the resistive screen the effects of shear waves within the screen are negligible. Since the resistive screen is close to being impervious, also the influence of the first compressional wave (*fluid wave*) is small. The applying engineer should, therefore, evaluate which layers of multi-layer assemblies are of most importance for the overall behaviour (and should be meshed accurately enough), and which layers do not require accurate meshing.

4.2.8 Mesh size sensitivity study for diffuse sound incidence (3D models with original Young's modulus)

For the sake of completeness, the transmission loss has been calculated for the same mesh sizes with the original material data. The results are shown in Figure 4.22. It can be observed that the deviations are higher than in the version with increased Young's modulus, which is expected since the number of nodes per wavelength is smaller. The mean and maximum deviations to the result obtained with the finest mesh size (1 mm), given in Table 4.11, indicate that at the finest mesh size the results have not yet fully converged (the number of elements per wavelength at 2 kHz is given in Table 4.4). This supports the choice of the model with increased Young's moduli for the sensitivity study and shows that with the currently available computational power the modelling of the system with original material data cannot be handled ideally. From Table 4.4 it can be observed that for increasing mesh sizes the mean and maximum deviations initially increase up to a mesh size of 8 mm and then, when the mesh size is further increased, decrease again. This is counter-intuitive and could be explained by a certain "randomness" of the results when the mesh size is much too coarse. From Figure 4.22 it can be observed that in the lower frequency range the errors obtained with the different mesh sizes are in a clear order, which is not the case in the upper part of the investigated frequency range, i.e. there the results are "random" and do not converge.

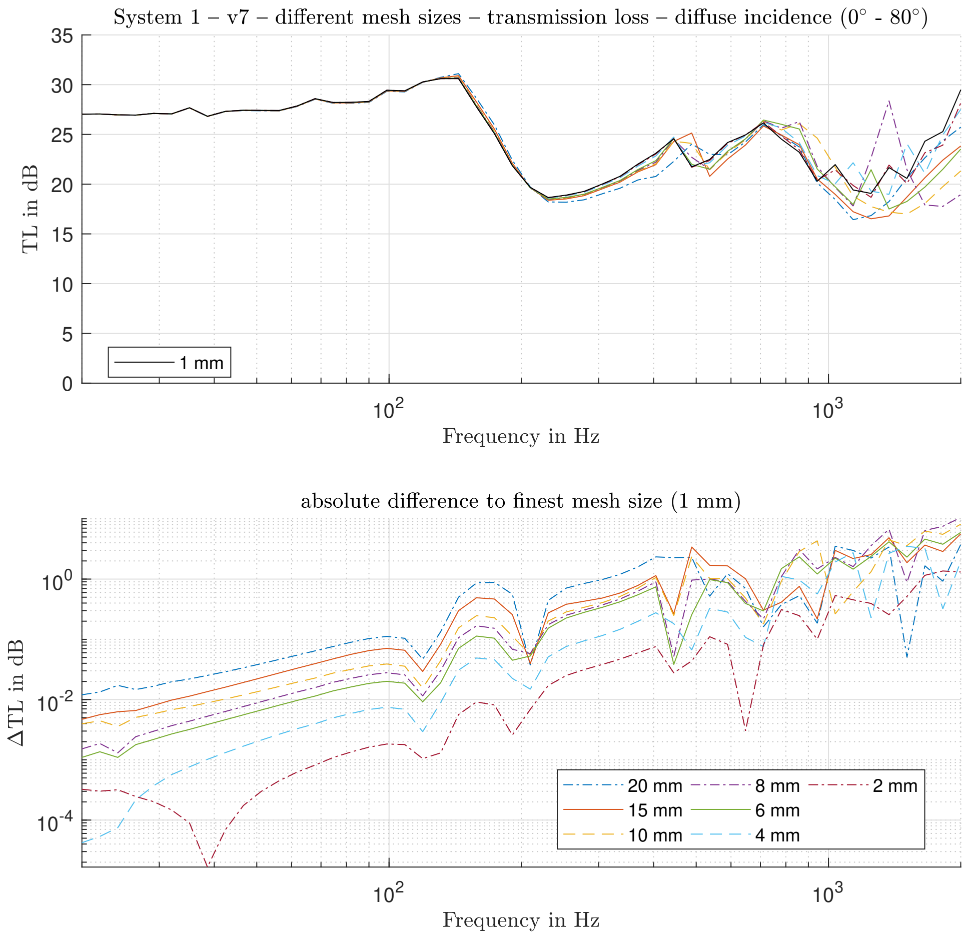

Figure 4.22: Transmission loss for diffuse incidence (0° - 80°) with model v7 (**original material data**), using different mesh sizes.

Table 4.11: Deviation of the transmission loss for different defined mesh sizes from the finest mesh size (1 mm) in the range from 20 Hz to 2 kHz. Compare Figure 4.22.

mesh size	mean deviation (in dB)	maximum deviation (in dB)
20 mm	0.78	3.74
15 mm	0.85	5.64
10 mm	1.00	8.15
8 mm	1.05	10.52
6 mm	0.76	5.95
4 mm	0.43	3.49
2 mm	0.15	1.36

4.2.9 Memory demands

As seen in the previously described sensitivity study, the FEM simulation of poroelastic materials requires a fine mesh size. Though the simulated sample only has an area of 0.01 m^2, the number of elements already ranges in the millions, with most having four degrees-of-freedom. The required memory to run the simulations with the mesh size shown in Table 4.3 is shown in Table 4.12.

Table 4.12: Peak process memory from different simulations variants.

	v1	v6	v7
Peak process memory	40596 MB	40687 MB	38242 MB

Models v1 and v6 use poroelastic components to model the sample, which leads to similar memory requirements. In model v7 the screens are modelled as limp with only one degree-of-freedom, which decreases the memory requirements. Due to the screens only being a small part of the model, this decrease is minor.

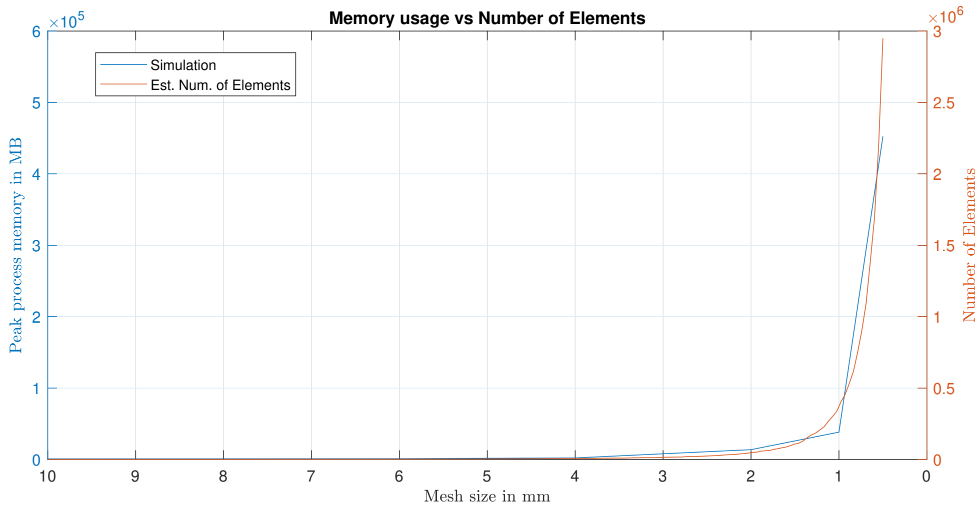

Figure 4.23: Peak memory usage in FEM compared to an estimate of the number of elements in the sensitivity study simulations from Section 4.2.5.

The largest factor in terms of memory usage is the size of the mesh, which can be seen in Figure 4.23. The required memory increases with the number of elements, where the number of elements in a single component can be calculated as $n = (\frac{t_i}{\Delta n}+1)(\frac{L}{\Delta n}+1)^2$, where L is the length of each side, t_i the thickness of the component and Δn the size of each element. This results in an estimated required memory of $M(\Delta n) \propto \frac{1}{\Delta n^3}$. As seen in Figure 4.23, a simulation using the original parameters and staying within the 1 dB error criteria up to 2 kHz, according to the sensitivity study in Table 4.6, would require a peak memory usage of 45 GB, which, while not impossible to run, is impractical. As a reminder, the simulated sample only has an area of 0.01 m^2.
It is worth noting that there is an exponential relation between wavelength and frequency, which is hinted in Figure 3.5, resulting in an even higher memory cost for each gain in the frequency range.

5

Discussion

The simulations of the absorption coefficient have been useful to understand the interaction between different layers in the investigated multi-layer assembly. By testing seven different modelling approaches for the complete five-layer assembly, comparing the FEM results to the results from TMM simulations and measurements, the models with the best match to measured data and the best match between FEM and TMM calculations could be identified. Particularly, it was found that the resistive screen needs to be modelled as impervious (or with a very low porosity), that the elastic properties of the felts need to be included in the model and that the elastic properties of the screens need to be included as well – if the resonances at low frequencies in the absorption coefficient (where the measured data is not accurate) are of interest. In future implementations, it might be of interest to model the screens as perforated plates, since this allows the use of 2D shell elements instead of 3D volume elements. In the current version of Actran (Actran 2020) this has, however, been found to yield erroneous results.[1]Apart from resonance peaks, which depend on the boundary conditions of the sample and are, therefore, difficult to predict, there has been found a good match of the FEM and TMM results to the measured data for models v1, v6 and v7. The Kundt's tube measurements carried out by the authors of this report (see Appendix D) show some deviations from the data which was provided by Matelys – Research Lab, which is also mostly due to the resonance peaks occurring at different frequencies. It shows, however, that the exact mounting conditions of the sample are of the utmost importance when doing Kundt's tube measurements of poroelastic materials with a significant stiffness.

Comparing the results of the absorption simulations to the results of the transmission simulations, it has been found that models which yield similar results for the sound absorption coefficient (v1, v6 and v7) also yield similar results for the transmission loss, while model v2, which shows a different characteristic in the calculated absorption coefficient, also behaves differently from the other three models in the transmission loss investigation. Due to these observations, it is expected that the calculated transmission loss would also match well to measured data. This, however, needs to be confirmed by measurements, the preparations for which are presented in Appendix E. The calculated sound transmission losses show that the resonance peaks which occur in the absorption coefficient at low frequencies are not relevant for the sound transmission loss. Therefore, model v7 has been identified as the preferred model for characterising the transmission loss of the investigated five-layer noise shield assembly because

[1] In contact with the FFT support it has been confirmed that the perforated plate object is currently not working correctly when coupled to poroelastic materials.

modelling the screens as limp reduces the number of degrees-of-freedom in the FEM model and also reduces the amount of required material data.

The mesh size sensitivity studies for normally incident plane waves in 2D (Section 4.2.2) and diffuse incident sound fields in 3D (Section 4.2.7) have shown that following the classic rule of thumb of sampling with at least 6 or 7 elements per smallest wavelength is sufficient to keep mesh-related errors below 1 dB. Exceptions from this are wave types and material layers which do not have a significant influence on the overall behaviour. In terms of wave types, these are e.g. shear waves in the 2D model for normally incident plane waves. In terms of material layers, these are e.g. the thin resistive screen. It has been shown that sufficiently accurate results are already reached without fulfilling all the mesh size requirements for these layers and wave types. This is because the screens are not expected to deform as such, rather they enable the felt to deform by being impervious and add some mass effects. It is up to the implementing engineer to develop a feeling for which wave types in which layers have a significant influence on the overall behaviour – and should, therefore, be meshed sufficiently fine – and which do not.

That said, it also has to be noted that the FEM simulation of soft poroelastic materials is currently still very much limited by the available computational power and memory resources. The finest investigated mesh size for which the sound transmission loss of the investigated five-layer system (model v7) could still be calculated without exceeding the memory limit of the dedicated simulation server was 0.5 mm, that is for a sample size of 0.01 m^2.[2] This mesh size resulted, however, in a calculation time of around 80 hours per frequency, which is not practical. The transmission loss was, therefore, calculated with a finest mesh size of 1 mm. Table 4.4 shows that with this mesh size the previously described meshing recommendations are not fulfilled at a frequency of 2 kHz when using the original Young's moduli of the materials. When investigating the sound transmission loss through noise shields which are implemented in trucks, the areas of the noise shields which need to be modelled are much larger than 0.01 m^2 and the noise shields are only a part of the complete models. This means that the upper-frequency limit of validity will be much lower than 2 kHz when the mesh size is chosen coarse enough to not exceed the memory limits of the simulation server.
In all the FEM-models in this report, all elements have been described using linear interpolation. Quadratic interpolation is known to lower the number of required elements per wavelength at the cost of higher calculation times. A preliminary investigation was made to investigate the possibility of using quadratic instead of linear elements. It was found that the memory demand which is reduced by using fewer elements is balanced out by the larger calculation effort that is needed per element, resulting in about the same calculation effort for achieving a certain accuracy. This should be investigated more thoroughly.

As lined out, the FEM modelling of soft poroelastic materials with short wavelengths is still very much limited by the computational resources available today. However, it also has to be noted that the differences in the calculated sound transmission loss due to different modelling approaches (only considering approaches which yield similar

[2] For a node distance of 0.4 mm the memory limit was exceeded.

results, i.e. models v1, v6 and v7) at the upper limit of the investigated frequency range exceed 10 dB (for the model with increased Young's moduli, compare Figure 4.15). With the same model, the maximum error due to different mesh sizes (up to 20 mm) only reached 4.3 dB (compare Table 4.9). This does not mean that fulfilling mesh requirements is not important, but it shows that the choice of modelling approach (between several models which essentially yield the same shape for the sound transmission loss) is at least as important as the precision of the mesh.

The generally good agreement between the FEM and TMM results for the sound absorption coefficient and sound transmission loss of the investigated system suggests that when only those measures are of interest, TMM should be used as a faster and computationally more efficient alternative to FEM modelling. However, as soon as systems with more complex structures and finite dimensions or the interaction with the surroundings are of interest, the possibilities of TMM are very limited so that FEM has to be used.

Future work includes the validation of the calculated transmission loss by measurements and the assessment of the transmission properties of systems where the compression grade changes over the area of the sample. Finding means of modelling larger areas of poroelastic materials accurately enough without exceeding the currently available computational resources will increase the usability of the method.

6
Conclusion

The sound absorption coefficient and sound transmission loss of a multi-layer truck noise shield, including felts of different compression grades and a resistive screen, have been calculated in FEM and TMM. Seven approaches for modelling this system have been investigated, three of which have been found to provide a good match between the FEM and TMM results as well as a good match to the measured data for the sound absorption coefficient. For simulating the sound transmission loss, the model with the lowest number of degrees-of-freedom and required material data is recommended. Measurements of the sound transmission loss have been planned but could not be carried out due to *force majeure*. Therefore, a comparison of the calculated sound transmission loss with measured data has not been possible. Mesh size sensitivity studies for normally incident plane waves and diffuse incident sound fields have shown that an accurate FEM modelling of soft poroelastic materials by the use of *Biot's theory* is currently still limited by the available computational resources. A number of 6 to 7 linear elements per wavelength has been found to be sufficient to reduce the error in the sound transmission loss due to the choice of mesh to below 1 dB, though this requirement does not have to be fulfilled for all three wave types in all layers of multi-layer assemblies.

Bibliography

[1] "Acoustics – Laboratory measurement of sound insulation of building elements – Part 2: Measurement of airborne sound insulation (ISO 10140-2:2010)," European Committee For Standardization, Brussels, Standard, Aug. 2010.

[2] J. F. Allard and N. Atalla, *Propagation of Sound in Porous Media: Modelling Sound Absorbing Materials*, 2nd ed. John Wiley & Sons, Ltd, 2009.

[3] M. R. Stinson, "The propagation of plane sound waves in narrow and wide circular tubes, and generalization to uniform tubes of arbitrary cross-sectional shape," *The Journal of the Acoustical Society of America*, vol. 89, no. 2, pp. 550 – 558, 1991.

[4] A. de Bruijn and J. Janssen, "Reciprocity and the zwikker-kosten equations for porous sound absorbing materials," 11 2017.

[5] L. L. Beranek, "Acoustic Impedance of Porous Materials," *Journal of the Acoustical Society of America*, vol. 13, no. 3, pp. 248–260, 1942.

[6] Luc Jaouen. Open Porosity. Accessed: 2020-02-03. [Online]. Available: http://apmr.matelys.com/Parameters/OpenPorosity.html

[7] H. Darcy, "Détermination des lois d'écoulement de l'eau à travers le sable," *Les fontaines publiques de la ville de Dijon*, 1856.

[8] M. K. HUBBERT, "DARCY'S LAW AND THE FIELD EQUATIONS OF THE FLOW OF UNDERGROUND FLUIDS," *International Association of Scientific Hydrology. Bulletin*, vol. 2, no. 1, pp. 23–59, 1957. [Online]. Available: https://doi.org/10.1080/02626665709493062

[9] Luc Jaouen. Static air flow resistivity. Accessed: 2020-02-03. [Online]. Available: http://apmr.matelys.com/Parameters/StaticAirFlowResistivity.html

[10] ——, "High frequency limit of the tortuosity," accessed: 2020-02-03. [Online]. Available: http://apmr.matelys.com/Parameters/HFLimitOfTortuosity.html

[11] D. L. Johnson, J. Koplik, and R. Dashen, "Theory of dynamic permeability and tortuosity in fluid saturated porous media," *Journal of Fluid Mechanics*, vol. 176, pp. 379–402, 1987.

[12] Luc Jaouen. Viscous Charateristic Length. Accessed 2020-02-03. [Online]. Available: http://apmr.matelys.com/Parameters/ViscousCharacteristicLength.html

[13] Y. Champoux and J. F. Allard, "Dynamic tortuosity and bulk modulus in air-saturated porous media," *Journal of Applied Physics*, vol. 70, no. 4, pp. 1975–1979, 1991.

[14] Luc Jaouen. Static Thermal Permeability. Accessed: 2020-02-03. [Online]. Available: http://apmr.matelys.com/Parameters/StaticThermalPermeability.html

[15] D. Lafarge, P. Lemarinier, J. F. Allard, and V. Tarnow, "Dynamic compressibility of air in porous structures at audible frequencies," *The Journal of the Acoustical Society of America*, vol. 102, no. 4, pp. 1995–2006, 1997.

[16] A. Cortis, "Dynamic Acoustic Parameters of Porous Media. a theoretical, numerical and experimental investigation," Delft, The Netherlands, 2002.

[17] M. E. Delany and E. N. Bazley, "Acoustical properties of fibrous absorbent materials," *Applied Acoustics*, vol. 3, pp. 105 – 116, 1970.

[18] Y. Miki, "Acoustical properties of porous materials - Modifications of Delany-Bazley models," *THE JOURNAL OF THE ACOUSTICAL SOCIETY OF JAPAN*, vol. 1, no. 11, pp. 19–24, 1990. [Online]. Available: https://www.jstage.jst.go.jp/article/ast1980/11/1/11{_}1{_}19/{_}pdf

[19] ——, "Acoustical properties of porous materials - Generalizations of empirical models," *THE JOURNAL OF THE ACOUSTICAL SOCIETY OF JAPAN*, vol. 1, no. 11, pp. 25–28, 1990.

[20] Luc Jaouen. Johnson-Champoux-Allard (JCA) model. [Online]. Available: http://apmr.matelys.com/PropagationModels/MotionlessSkeleton/JohnsonChampouxAllardModel.html

[21] ——. Johnson-Champoux-Allard-Lafarge (JCAL) model. [Online]. Available: http://apmr.matelys.com/PropagationModels/MotionlessSkeleton/JohnsonChampouxAllardLafargeModel.html

[22] S. R. Pride, F. D. Morgan, and A. F. Gangi, "Drag forces of porous-medium acoustics," *Physical Review B*, vol. 47, no. 9, pp. 4964–4978, 1993.

[23] Luc Jaouen. Johnson-Champoux-Allard-Pride-Lafarge (JCAPL) model. [Online]. Available: http://apmr.matelys.com/PropagationModels/MotionlessSkeleton/JohnsonChampouxAllardPrideLafargeModel.html

[24] B. Castagnède, A. Aknine, B. Brouard, and V. Tarnow, "Effects of compression on the sound absorption of fibrous materials," *Applied Acoustics*, vol. 61, no. 2, pp. 173–182, 2000.

[25] N. Atalla and F. Sgard, "Modeling of perforated plates and screens using rigid frame porous models," *Journal of Sound and Vibration*, vol. 303, no. 1-2, pp. 195–208, 2007.

[26] N. Atalla, R. Panneton, and P. Debergue, "A mixed displacement-pressure formulation for poroelastic materials," *The Journal of the Acoustical Society of America*, vol. 104, no. 3, pp. 1444–1452, 1998. [Online]. Available: https://doi.org/10.1121/1.424355

[27] F.-X. Bécot and F. Sgard, "On the use of poroelastic materials for the control of the sound radiated by a cavity backed plate," *The Journal of the Acoustical Society of America*, vol. 120, no. 4, pp. 2055–2066, 2006. [Online]. Available: https://doi.org/10.1121/1.2214134

[28] F.-X. Bécot and L. Jaouen, "An alternative biot's formulation for dissipative porous media with skeleton deformation," *The Journal of the Acoustical Society of America*, vol. 134, p. 4801–4807, 12 2013.

[29] O. Dazel, J.-P. Groby, B. Brouard, and C. Potel, "A stable method to model the acoustic response of multilayered structures," *Journal of Applied Physics*, vol. 113, 02 2013.

[30] P. Debergue, R. Panneton, and N. Atalla, “Boundary conditions for the weak formulation of the mixed (u,p) poroelasticity problem,” *The Journal of the Acoustical Society of America*, vol. 106, no. 5, pp. 2383–2390, 1999. [Online]. Available: https://doi.org/10.1121/1.428075

[31] P. Bonfiglio, F. Pompoli, and R. Lionti, “A reduced-order integral formulation to account for the finite size effect of isotropic square panels using the transfer matrix method,” *The Journal of the Acoustical Society of America*, vol. 139, no. 4, pp. 1773–1783, 2016. [Online]. Available: https://doi.org/10.1121/1.4945717

[32] “Acoustics – Determination of sound absorption coefficient and impedance in impedances tubes – Part 2: Transfer-function method (ISO 10534-2:1998),” European Committee For Standardization, Brussels, Standard, Jun. 2001.

[33] “Acoustics – Laboratory measurement of sound insulation of building elements – Part 5: Requirements for test facilities and equipment (ISO 10140-5:2010),” European Committee For Standardization, Brussels, Standard, Aug. 2010.

[34] “Acoustics – Laboratory measurement of sound insulation of building elements – Part 4: Measurement procedures and requirements (ISO 10140-4:2010),” European Committee For Standardization, Brussels, Standard, Aug. 2010.

A
Additional theory

A.1 Helmholtz resonator

The resonance frequency of a Helmholtz resonator with circular holes can be calculated with

$$f_0 = \frac{c}{2\pi}\sqrt{\frac{S}{V\left(l_\mathrm{h} + \frac{\pi}{2}r\right)}}, \tag{A.1}$$

where r is the radius, l_h is the length, S is the area of the hole. V is the volume connected to each hole and c is the speed of sound in air.
For perforated plates at a distance t from a rigid wall the effective volume for each hole is not the total volume of air in between the plate and the wall but rather just a portion of the volume belonging to each hole. It can be easily derived that the area A corresponding to the effective volume of each hole and the hole area S are related by the porosity ϕ as

$$\phi = \frac{S}{A}. \tag{A.2}$$

Using this expression, the effective volume belonging to each hole can be expressed as a function of the porosity:

$$V = \frac{S \cdot t}{\phi}. \tag{A.3}$$

When porous materials are modelled as perforated plates (assuming straight pores without cross-sectional variations) the perforation radius r is equal to the viscous and thermal characteristic lengths [2]:

$$r = \Lambda = \Lambda'. \tag{A.4}$$

Using these expressions, Equation A.1 can be re-written to calculate the Helmholtz resonance frequency for a layer of porous material at a distance t from a rigid wall as

$$f_0 = \frac{c}{2\pi}\sqrt{\frac{\phi}{t\left(l_\mathrm{h} + \frac{\pi}{2}\Lambda\right)}}. \tag{A.5}$$

B

Fluid phase models: Parameters

Table B.1: Parameters used in the different fluid phase models: Overview.

Model	Required parameters
DB (Delany-Bazley)	• Static air flow resistivity σ
DBM (Delany-Bazley-Miki)	• Static air flow resistivity σ
Miki	• Static air flow resistivity σ • Open porosity ϕ • High frequency limit of the dynamic tortuosity α_∞
JCA	• Static air flow resistivity σ • Open porosity ϕ • High frequency limit of the dynamic tortuosity α_∞ • Viscous characteristic length Λ • Thermal characteristic length Λ'
JCAL	• Static air flow resistivity σ • Open porosity ϕ • High frequency limit of the dynamic tortuosity α_∞ • Viscous characteristic length Λ • Thermal characteristic length Λ' • Thermal static permeability κ'_0
JCAPL	• Static air flow resistivity σ • Open porosity ϕ • High frequency limit of the dynamic tortuosity α_∞ • Viscous characteristic length Λ • Thermal characteristic length Λ' • Thermal static permeability κ'_0 • Static viscous tortuosity $\alpha_{\text{visc.}}$ • Static thermal tortuosity $\alpha_{\text{th.}}$

C
Additional investigations

C.1 Speed of sound in the felts

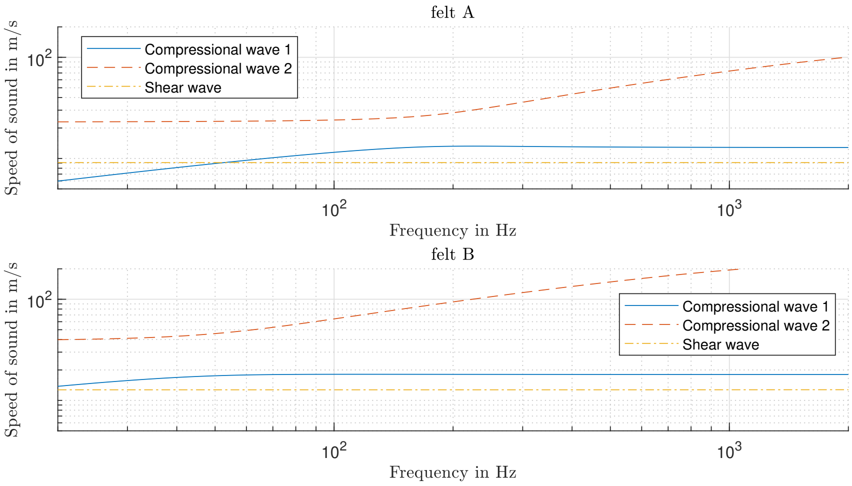

Figure C.1: Speed of sound in the two felts (with **original Young's moduli**).

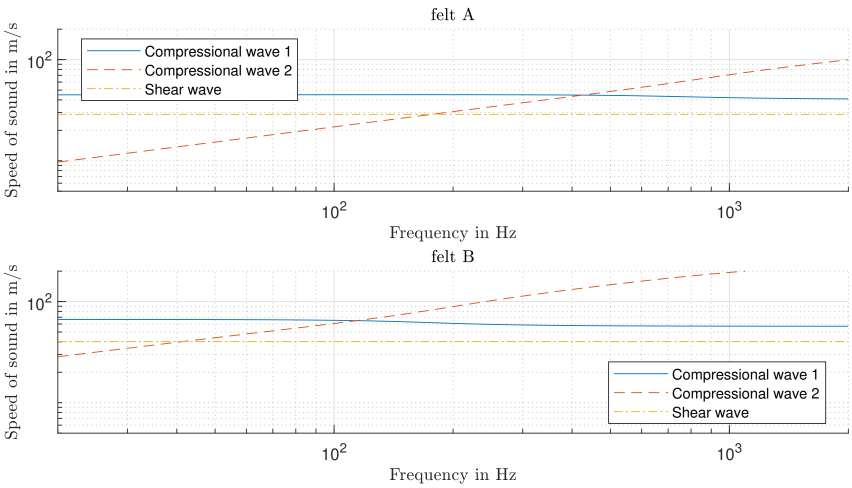

Figure C.2: Speed of sound in the two felts (with **increased Young's moduli**).

C.2 Elastic modelling of single layer of porous material

In contrast to the results shown in Figure 3.6 for the absorption coefficient of a single layer of felt for normally incident plane waves, there can be observed differences between the different approaches of modelling the elastic behaviour for materials which exhibit more elastic properties, as it is shown in Figure C.3.

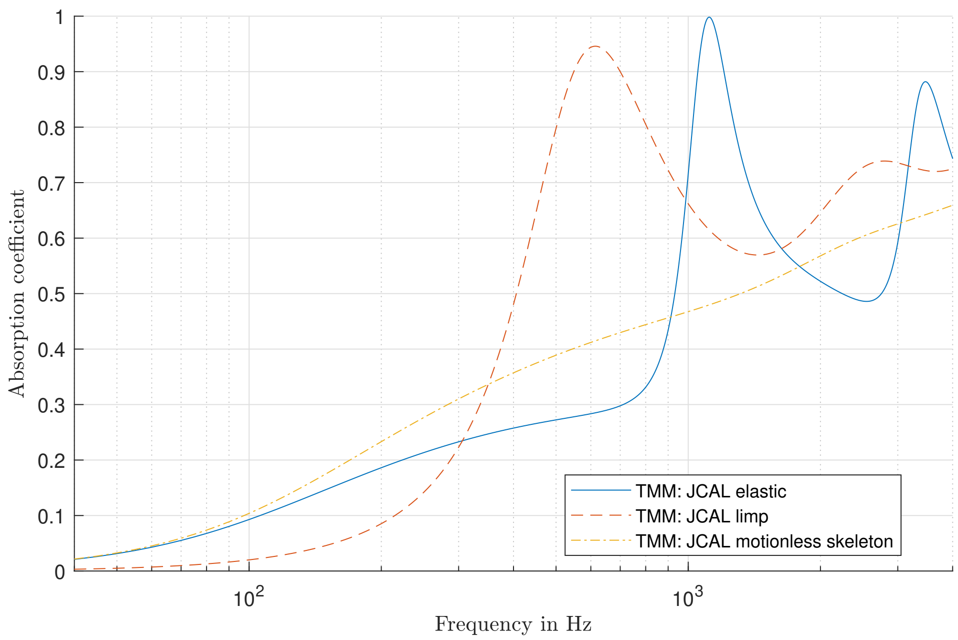

Figure C.3: Single layer of felt with different modelling approaches for the elastic behaviour. The felt modelled here has the same thickness as felt B.

The elastic properties of this material are given in Table C.1.

Table C.1: Properties of the felt investigated in Figure C.3 (different from the felts which are generally investigated in this study).

ρ	26 kg/m^3
E	$1.16\cdot10^5$ Pa
η	0.11
ν	0.43
σ	$2.17\cdot10^5$ Ns/m^4
ϕ	0.98
α_∞	1.28
Λ	$6\cdot10^{-6}$ m
Λ'	$2.77\cdot10^{-4}$ m
κ_0'	$7.4\cdot10^{-9}$ m^2

C.3 Resonances in felt-screen-felt multi-layer system

The behaviour of the felt-screen-felt multi-layer system investigated in Section 3.3.1.3 can be explained illustratively by modelling one of the felts as rigid at a time, as shown in Figure C.4.

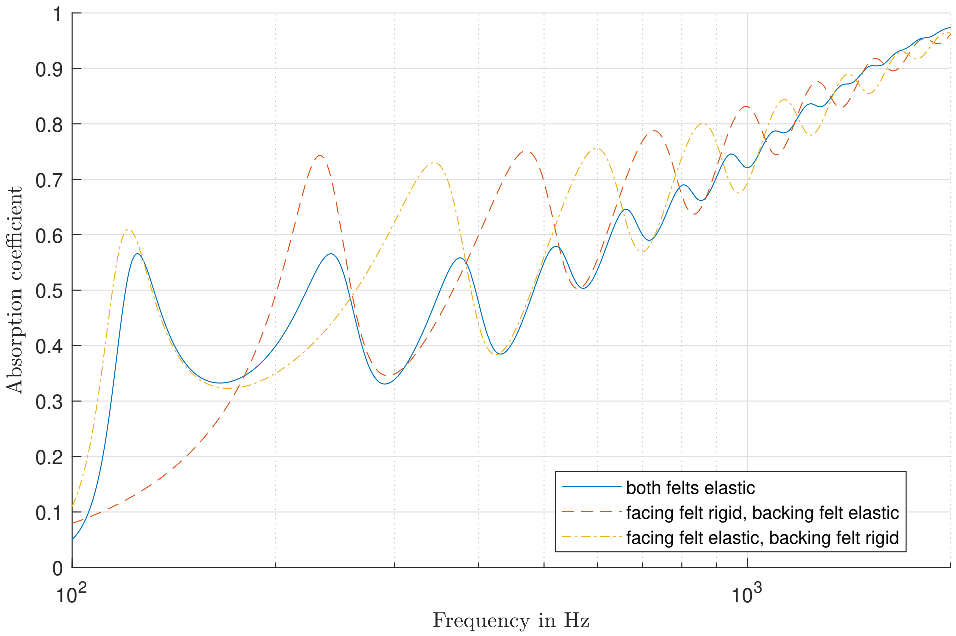

Figure C.4: Felt-screen-felt multi-layer system with different modelling approaches for the two felts.

When the backing felt is considered as rigid, the resistive screen represents a rigid backing for the facing felt. This imposes a pressure maximum at the surface of the facing felt which is touching the resisitive screen and a pressure minimum at the free surface of the facing felt. This leads to resonances for frequencies where the thickness of the felt corresponds to 1/4, 3/4 etc. of the wavelength of the compressional wave in the fluid, which corresponds to the dips in the absorption coefficient at 150 Hz, 450 Hz etc.. When the facing felt is considered as rigid, this imposes a pressure maximum on both ends of the backing felt. This leads to resonances at frequencies, where the thickness of the felt corresponds to 2/4, 4/4, etc. of the wavelength of the compressional wave in the fluid, which corresponds to the dips in the absorption coefficient at 300 Hz, 600 Hz etc.. From Figure C.4 it can be observed that for the case when both felts are modelled as elastic, all of these resonances appear, since there are dips in the absorption coefficient at 150 Hz, 300 Hz, 450 Hz etc..

D
Absorption measurement with Kundt's tube

To validate the TMM and FEM models for plane wave incidence, the absorption coefficient of each sample was measured in the impedance tube at Chalmers (Division of Applied Acoustics). However, due to the lack of proper cutting tools, it was difficult to cut samples to exact dimensions and leave enough tolerance to not compress the sample in the tube without leaving any leakage. The measurements were deemed too poor to be used for an experimental validation of the simulations, but the procedure and results are found below.

D.1 General description of the measurements

The absorption coefficient of different multi-layer samples was measured using an impedance tube according to ISO-10534. The tube, which is seen in Figure D.1a, utilises one microphone which is free to rotate between two positions. The top of the tube, where the sample is mounted, is removable and adjustable, so that the distance between the sample and microphone positions is always the same. When mounted in the correct position, the circumference of the sample was covered with modelling clay, as seen in Figure D.1b, to block leakage on the sides and to keep the sample in place. The tube has a diameter of 99 mm. The length between speaker and sample is about 50 cm and the distance between the closest microphone and sample is about 25 cm. The distance between the microphone positions is 5 cm.

D.2 Theory

D.2.1 Determining the transfer function

The transfer function to be used in this measurement is commonly referred to as the H_1-estimate, which is determined by measuring the sound pressure in two positions. The H_1-estimate is calculated with:

$$H_1 = \frac{S_{12}}{S_{11}}, \tag{D.1}$$

where $S_{12} = p_1(\omega)(p_2(\omega))^*$ is the cross-spectrum of the two measurements and $S_{11} = p_1(\omega)(p_1(\omega))^*$ the auto-spectrum of one of the measurements. $p(\omega)$ is the measured pressure amplitude in the frequency domain.

(a) (b)

Figure D.1: Measurement setup: (a) Impedance tube (b) Mounting of the sample.

D.2.2 Determining the reflection factor

The reflection factor is determined by:

$$r = \frac{H_1 - H_I}{H_R - H_1}, \tag{D.2}$$

where $H_I = e^{-jk_0 s}$ and $H_R = e^{jk_0 s}$. k_0 is the wave number in air and s the distance between the microphones (see Annex D in [32]).

D.3 Criteria, demands and validity

The primary limitation for the valid frequencies are the dimensions of the tube. In the lower range, the valid frequency range is partly limited by the length of the tube, which should be long enough to allow planes waves to develop properly. Non-plane modes, that can develop, will die out at a distance of about 3 diameters, which is the minimum distance between the speaker and microphone.
The lower frequency limit is also dependant on the spacing between the microphone positions, which should not be lower than 5% of the wavelength of the lowest frequency:

$$f_l s > 0.05 c_0. \tag{D.3}$$

This limit is influenced by the accuracy of the analysis system. Therefore, the limit in

Equation D.3 should be seen as a general guideline. If the accuracy is poor, the range between the microphones can be increased at the cost of a decreased upper limit.
For the Chalmers impedance tube, this limit would be 343 Hz, for $c_0 = 343$ m/s.
The upper frequency f_u is limited by the appearance of non-plane modes, which depends on the diameter of the tube:

$$f_u d \leq 0.58 c_0. \tag{D.4}$$

It also depends on the spacing of measurement positions, where:

$$f_u s < 0.45 c_0 \tag{D.5}$$

Using the parameters of the Chalmers impedance tube, the upper frequency limit is 1989 Hz for the first criterion and 3087 Hz for the second.

D.4 Results

As seen in Figure D.2, the measured results differ from the results measured by Matelys – Research Lab. This indicates different boundary conditions, such as the sample being pressed against the periphery of the tube. Since the apparent boundary condition changes between the different samples, any attempt to compensate for it in the model would be futile. The orange line in Figure D.2 is a sample cut to 99 mm diameter with a laser-cutter. Despite the high precision of the cut, the result is very similar, which likely means that the tolerance is too small and that the diameter needed to be decreased by an additional 0.5 mm - 1 mm. The lowest plot in Figure D.2 shows the measured absorption coefficient of the empty tube. Since the system registers absorption below 200 Hz, results below this frequency should be disregarded. This lower frequency limit is in line with what is expected from Equation D.3.

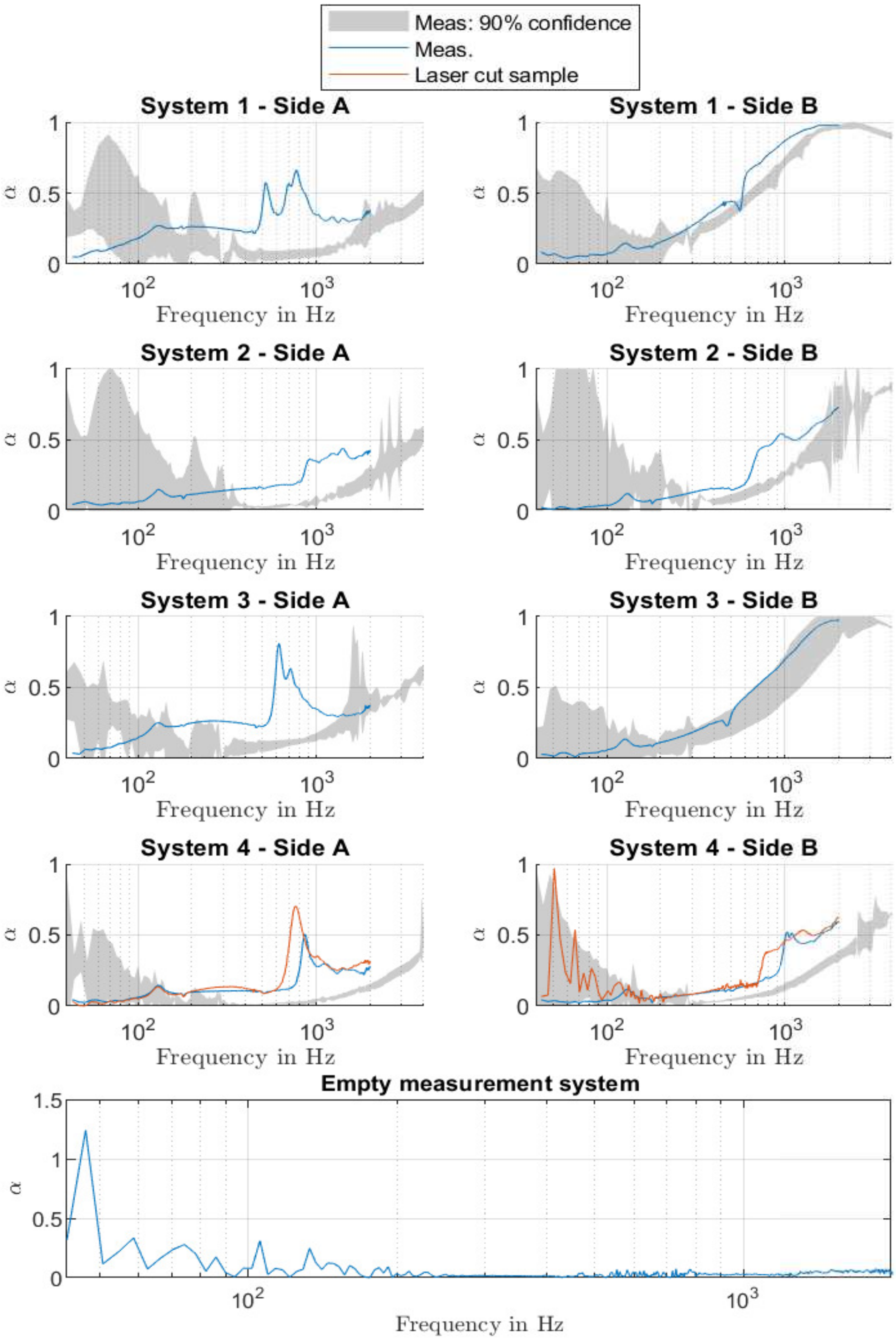

Figure D.2: Comparison between measurements done at Chalmers and the measurements made by Matelys – Research Lab. The lowest curve shows the absorption measured in an empty tube.

E

Transmission measurement

To verify the transmission loss calculated by the TMM and FEM models, a room transmission measurement was planned. Due to the Covid-19 pandemic it could not be carried out. The plan for the measurement can be found below, including calculations to ensure that the sample can be mounted without excessive sound leakage. Note that this pre-study was written early in the project and that the layer interactions of the multi-layer absorber had not yet been fully understood. If the measurement is carried out according to this appendix, additional simulations should be made according to the findings of this report to ensure that the measurement setup fulfils the demands set by the standard.

E.1 Purpose

The purpose of the measurement is to determine if/how the transmission of sound through a truck noise shield composed of several layers of compressed fibrous materials can be accurately modelled using FEM. The results of the measurements are meant to validate the different FEM modelling approaches in Actran, together with the TMM simulations from AlphaCell. The methodology below is adapted to be performed according to ISO 10140-2 at the Chalmers reverberation chamber/transmission lab.

E.2 General description of the measurements

The opening in the partition between the source and the receiving room (inner dimensions of the red frame seen in Figure E.1a: 1.15 m × 1.85 m) is closed with a double leaf gypsum wall (fitting the outer dimensions of the red frame seen in Figure E.1a, 1.32 m × 2.03 m). This wall contains a rectangular opening (0.58 m × 0.38 m), where the test element (truck noise shield) can be mounted. Note that the test element is not plane. The test element should not be tampered with during the mounting unless absolutely necessary. If it is unable to support itself, a layer of silicone can be added along its periphery to keep it in place. As an additional effect, this would also reduce leakage from any potential air gap along the sides of the element.

(a)

(b)

Figure E.1: Opening between the two rooms. As seen, the partition is being pressed against a steel frame (red) from the sending side.

To measure the sound transmission through the double leaf gypsum wall alone, it is necessary to close the opening which is left for mounting the test element. This could be done with a 0.58 m × 0.38 m gypsum board covered with an additional heavy layer (surface density ≈ 25 kg/m^2), as recommended in ISO-standard 10140-2 . When closing the wall, the test element is kept in the opening. The space between the test element and the additionally mounted element is filled with porous absorbing material [1].
In the source room a diffuse sound field is generated and the average sound pressure levels in the diffuse field of the source room and the receiving room are measured. This requires several measurements with changing loudspeaker positions, according to ISO:10140-5. The reverberation time in the receiving room should be measured to determine the absorption area of the room (as specified in ISO:10140-4). Although not required by the standard, the reverberation time of the sending room should also be measured to ensure that it fulfils the characteristics of a diffuse sound field. The temperature, relative humidity and static pressure shall be measured [33][34].

E.2.1 Sequence of measurements

To be able to verify the validity of the setup, several measurements should be done during the construction, looking for cracks or other deviations from the expected results.

- **Setup 1:** The first measurements are made with the double leaf wall assembled without the opening meant for mounting the test element. The reverberation time of the receiving room is measured and the equivalent absorption area calculated. Given the small size of the cut out window, this reverberation time could also be valid for the rest of the measurements, but this should be determined after the measurement. The transmission loss is then measured according to the standard. The result should then be compared to expected results from simulations. If any deviations appear, the setup should be searched for cracks or other defects. Measurements should be done until the setup performs as expected.

- **Setup 2:** After the first setup performs in a satisfying way, the frame where the test element is placed is cut out according to the schematics. When the partition has been cut and reassembled, the frame is closed with the gypsum board covered with a heavy layer. The transmission measurement is then remade and analysed. This should give very similar results to the previous measurement and reasons for any deviations should be determined before proceeding. This is to ensure that the opening has not introduced any leaks.
- **Setup 3:** The gypsum board and the heavy layer are then removed, after which the transmission loss is measured with an empty frame. This is to determine, at which frequency the small sized window starts to block long wavelengths.
- **Setup 4:** If the previous three setups have generated satisfying results, the partition should be good enough to measure accurately. For the fourth and final set of measurements, the test element is fitted in the frame after which the reverberation time is measured once more. The transmission loss can then be measured.

E.3 Theory

In ISO:10140-2 the apparent sound reduction index/transmission loss is defined as:

$$R' = -10\log\tau' \text{ dB}, \tag{E.1}$$

where the apparent transmission ratio τ' is defined as:

$$\tau' = W_2/W_1. \tag{E.2}$$

In this equation, W_1 is the sound power which is incident on a test element and W_2 is the total power radiated into the receiving room (sum of the sound powers radiated by the test element and flanking elements). For laboratory measurements, the apparent sound reduction index is calculated as

$$R' = L_1 - L_2 + 10\log\frac{S_\text{s}}{A} \text{ dB} \tag{E.3}$$

where S_s is the surface area of the opening in which the test element is installed and A the equivalent sound absorption area of the receiving room. L_1 and L_2 are the energy average sound pressure levels measured in the respective rooms. This formula is only valid if the sound fields in both rooms are diffuse. From Sabine's formula, the equivalent sound absorption area is calculated as:

$$A = \frac{55\ V}{c\ T_{60}}, \tag{E.4}$$

where V is the volume in the room, c the speed of sound in air and T_{60} the reverberation time [1].

E.4 Criteria, demands and validity

E.4.1 Room demands

According to ISO:10140-5 the volumes of the rooms should be at least 50 m^3 and differ about 10%. The reverberation time should be

$$1 \leq T_{60} \leq 2(V/50)^{2/3}.$$

As described earlier, the used equation for calculating the sound reduction index is only valid if the sound fields in both rooms are diffuse. A criterion for the diffuseness of a sound field is the Schroeder frequency

$$f_{\text{Schroeder}} = 2000\ \text{Hz}\sqrt{\left[\frac{T_{60}}{V}\right]}, \tag{E.5}$$

above which the sound field in a room can be considered as diffuse [33].

E.4.2 Mounting demands (according to ISO10140-2)

The aperture depths on each side of the test element shall be different and close to the ratio 2:1. The absorption coefficient of the materials lining the aperture shall be smaller than 0.1 for all frequencies of interest.

E.4.3 Partition demands (according to ISO10140-2)

As the test element is smaller than the test opening, a special partition (in our case the double wall construction outlined below) has to be built into the test opening. The energy transmitted through this partition has to be negligible compared to the energy transmitted through the test element, or the measured values have to be corrected. In order to evaluate this, the sound reduction index of the partition wall R'_F has to be measured separately. The energy transmitted through the partition can be neglected if

$$R'_F \geq R'_M + 15\ \text{dB}. \tag{E.6}$$

For small technical elements this is reduced to 10 dB, “since it is practically more difficult to achieve high limits” [1]. If this is not fulfilled, the levels have to be corrected with

$$R = -10\log\left(10^{-R'_M/10} - 10^{-R'_F/10}\right), \tag{E.7}$$

where R'_M is the sound reduction index measured with the test element in the opening and R'_F the measured sound reduction index with the closed test opening. In any case the limit

$$R'_F \geq R'_M + 6\ \text{dB} \tag{E.8}$$

has to be fulfilled (else the correction is 1.3 dB and the corresponding frequencies are to be indicated).

E.4.4 Measurements

In [34] the criteria for microphone positions, averaging times, correction for background noise, measurement of reverberation time and special procedures for measuring at low frequencies are described. Background noise should be at least 10 dB lower than the sound level with the signal. In ISO:10140-5, Annex D-1 the qualification procedure for loudspeaker positions is described [33].

E.5 Setup

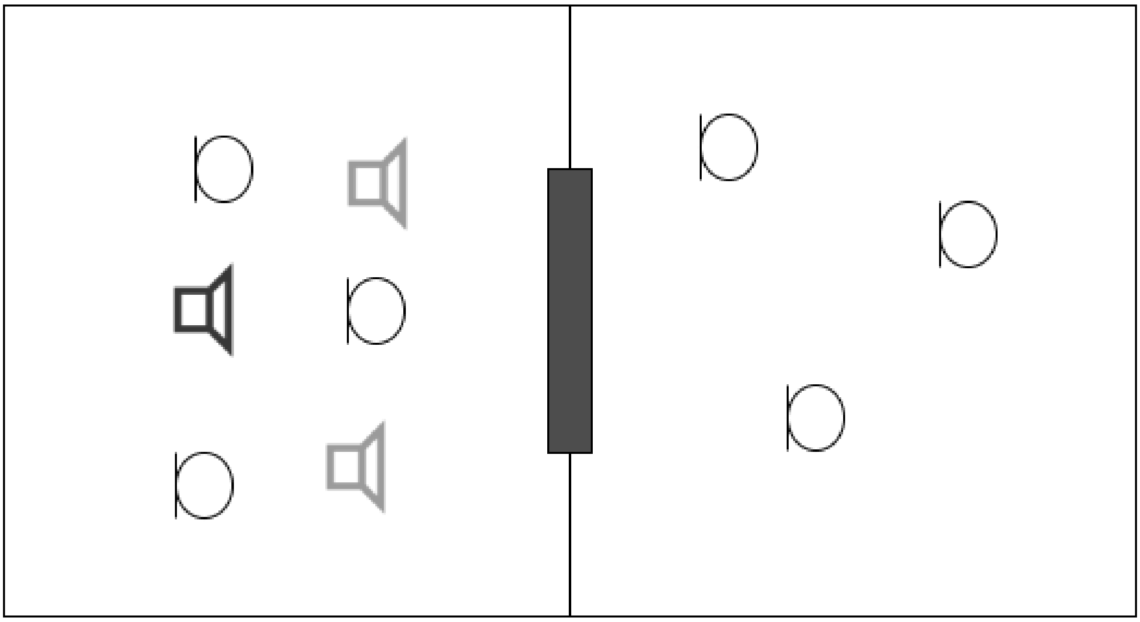

Figure E.2: Setup of transmission measurement.

The measurement should be done according to the demands listed in Section E.4.4. The loudspeaker is set up in the source room and the microphone in the receiving room. The number of necessary loudspeaker positions is then determined according to ISO:10140-5, Annex D.1.3. The loudspeaker is then moved to the first of at least two positions, and microphones mounted to as many positions as possible in the receiving room. One microphone is also mounted in the source room. The measurement is conducted according to the standard, Section 5.2.3, which states that white noise is played through the speaker and measured by the microphones in both rooms. The measurement is then repeated until the sound has been recorded at at least three positions in the receiving and the source room. The loudspeaker is then moved to the next position, where the measurement is repeated for the same microphone positions. Repeat until the demands of Annex D.1.3 in the standard are satisfied [33].

E.6 Planning of double wall construction

In order to measure the sound transmission loss of the noise shield according to [1], it is necessary to also measure the flanking transmission through the wall partition. For this purpose, the opening in the wall partition where the noise shield is mounted is acoustically closed. With the closed opening the sound transmission loss should be at least 15 dB (10 dB for small technical elements) higher than the sound transmission loss with the noise shield mounted. Else, the measurement becomes inaccurate and a correction for flanking transmission has to be applied [1]. The required increase in the sound transmission loss when closing the opening is only achieved when the sound transmission loss of the wall partition and through the closed opening are high enough. A feasibility study of the planned partition wall design was undertaken in *AlphaCell*. The sound transmission losses of the noise shield, the planned occlusion for closing the opening and the double leaf partition wall design were estimated and the difference in sound transmission loss with open and closed opening calculated.

E.6.1 Estimation of the noise shield transmission loss

In *AlphaCell* the expected transmission loss of the noise shield was estimated. For this purpose, a noise shield sample was used, shown in Figure 3.1 and F.1. In *AlphaCell* this was reproduced with the configuration shown in Figure F.2, using the material data shown in Figure F.3. The calculated sound transmission loss for a diffuse incident sound field is shown in Figure E.3. The configuration and material data were estimated and not based on measurements, except from the fluid phase parameters of the fibrous materials No. 14, No. 15 and No. 16, which are (old and possibly inaccurate) measured data.[1] To include elastic behaviour, the Young's modulus of the fibrous materials was estimated.

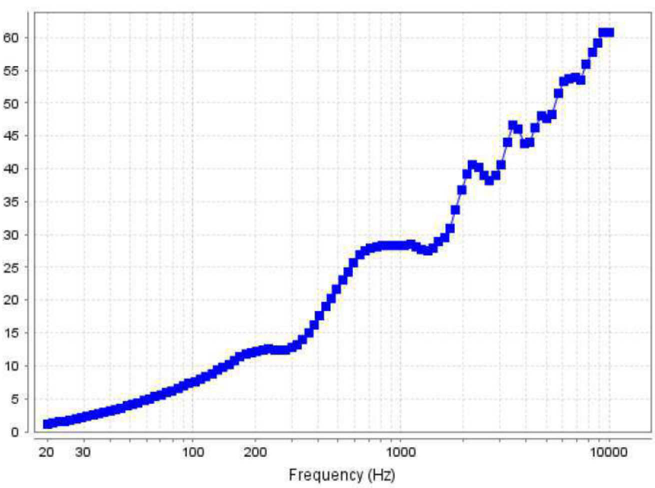

Figure E.3: Predicted transmission loss in dB of the noise shield.

[1] This data stems from the characterisation of the material which has been done earlier than the characterisation by Matelys – Research Lab. The values are given in Appendix F.

E.6.2 Estimation of the double leaf wall transmission loss

The gypsum double leaf wall is planned as follows:

- 2 × 12.5 mm gypsum board
- ~ 80 mm fibrous material
- 3 × 12.5 mm gypsum board

This results in a total thickness of ~ 143 mm (the available space is ~ 170 mm). In the centre of the double leaf wall there is an opening for the mounting of the noise shield. In the available test facility there is an opening in the (brick)wall with the total size 1.32 m × 2,03 m. This opening is framed with a metal plate for the mounting of the wall partition. The opening inside of this metal frame has the size 1.15 m × 1.85 m. This is the area that the above described gypsum double leaf wall will cover. For mounting the double leaf wall to the metal frame, the double leaf wall is framed with wooden beams. In total, the wall geometry can be split up into four areas with different cross-sections (from inside outwards, compare Figure E.4):

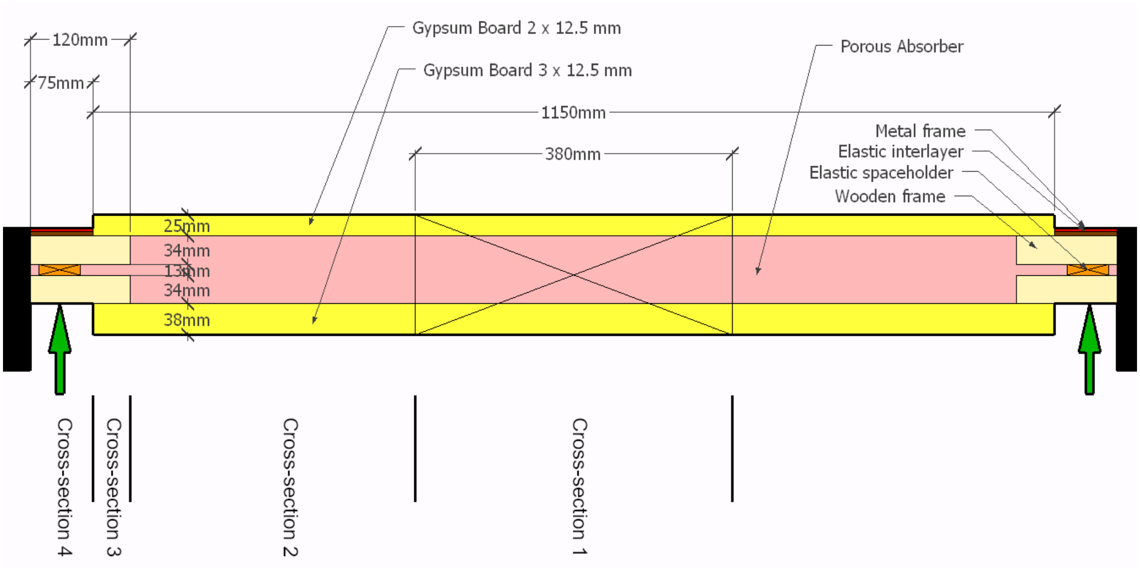

Figure E.4: Cross-section of the double leaf gypsum wall construction with indicated areas of different cross-section. The black areas on the sides indicate the brick wall.

1. Opening, in which the noise shield is mounted (0.22 m^2).[2]
2. Double leaf wall construction as outlined above (1.78 m^2).
3. Outer area of the double leaf wall construction where there are wooden beams between the gypsum plates (0.13 m^2).
4. Area outside of the gypsum double leaf wall construction where there are wooden beams backed by the metal plate that is used for mounting (0.55 m^2). The wooden beams are separated by space holders at the positions where force is applied for the mounting (indicated by green arrows in Figure E.4).

For each of these areas the sound transmission loss has been calculated in *AlphaCell.*

[2]Assuming that the noise shield is cut to an area of 580 mm × 380 mm = 0.2204 m^2. This is the maximum rectangular area without holes that the noise shield can be cut to. When closing the holes the area could be enlarged.

E.6.2.1 Area 1 – Opening

In this area, either the noise shield is mounted, the simulation of which has been presented above, or the opening is closed for the measurement of flanking transmission. For closing the opening, ISO10140-2 recommends mounting an iron plate attached to a gypsum board additionally to the measured test element and filling the space in between with a porous absorber. Since no iron or steel plates were available, it was planned to use bitumen with attached textile-fibre mats instead. These are attached to both sides of a gypsum plate. A schematic of the construction is shown in Figure E.5, with the materials indicated in Figure F.6 and the calculated transmission loss in Figure E.6.

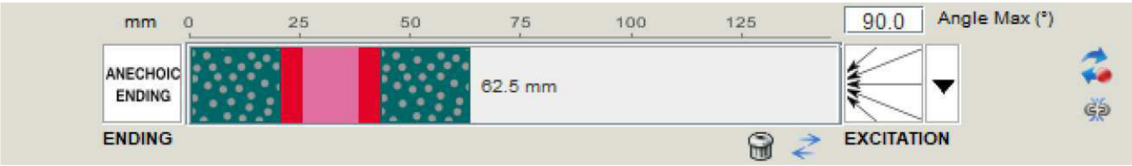

Figure E.5: AlphaCell model of the bitumen-gypsum occlusion.

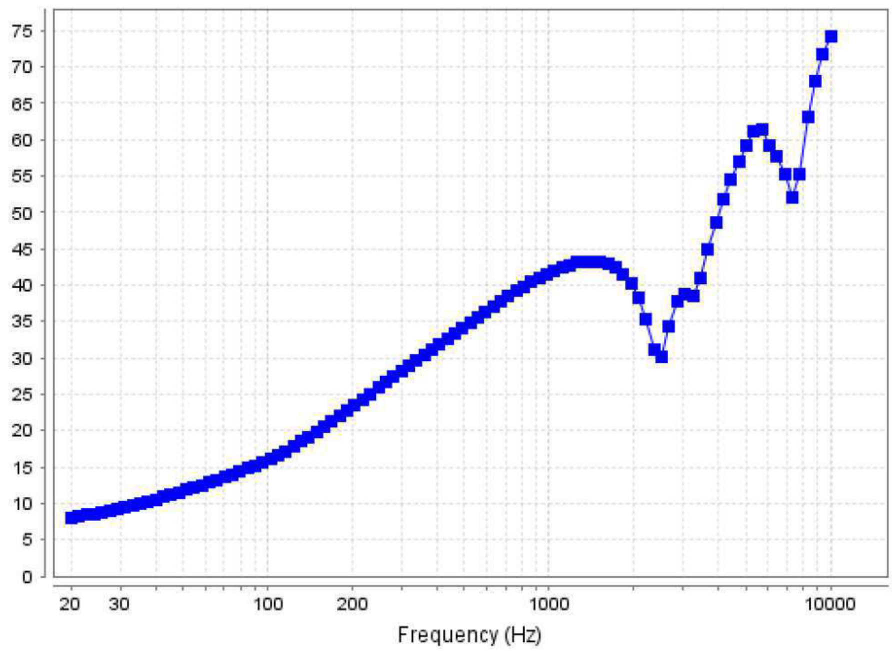

Figure E.6: Predicted transmission loss in dB of the bitumen-gypsum occlusion.

When closing the opening as recommended in [1], i.e. with the noise shield and the additional occlusion mounted together, the construction looks as shown in Figure F.10. The calculated resulting transmission loss is shown in Figure E.7.

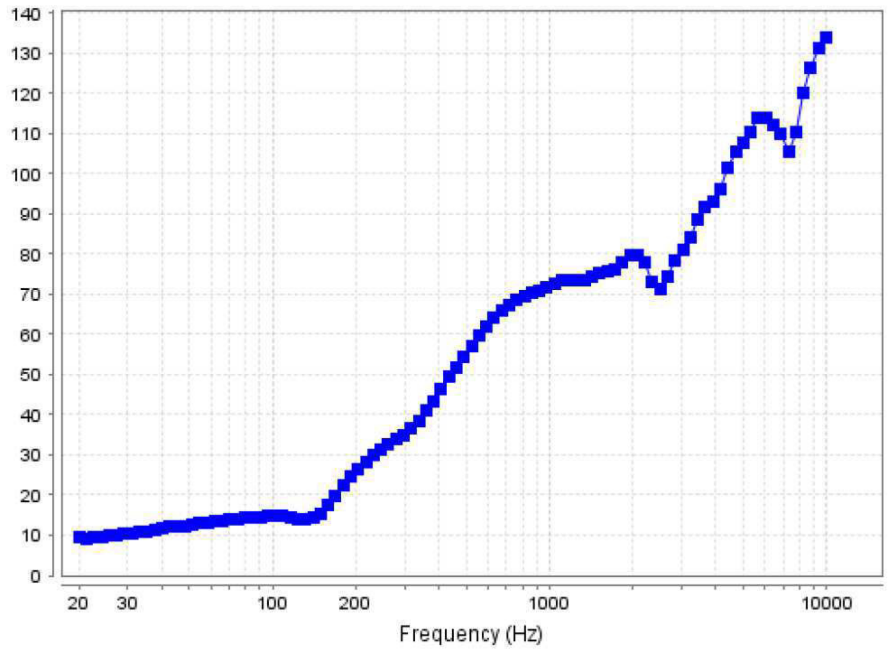

Figure E.7: Predicted transmission loss in dB of the noise shield with the additional bitumen-gypsum occlusion.

E.6.2.2 Area 2 – Gypsum double leaf wall

The construction and materials of the gypsum double leaf wall (cross-section area 2) are shown in Figure E.8 and F.7. The predicted transmission loss is shown in Figure E.11.

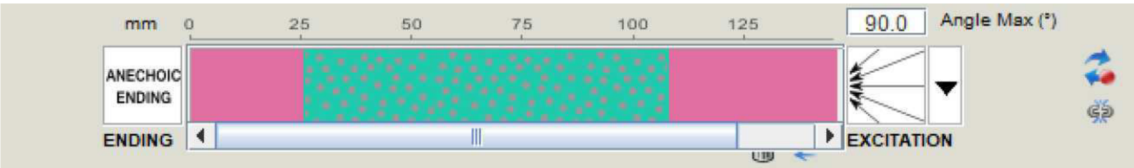

Figure E.8: AlphaCell model of the gypsum double leaf wall (cross-section area 2).

E.6.2.3 Area 3 – Gypsum double leaf wall with wooden beams

The construction and materials of the gypsum double leaf wall with wooden beams (cross-section area 3) are shown in Figure E.9 and F.8. The predicted transmission loss is shown in Figure E.11.

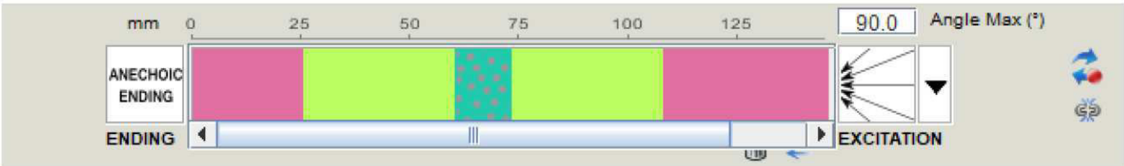

Figure E.9: AlphaCell model of the gypsum double leaf wall with wooden beams (cross-section area 3).

E.6.2.4 Area 4 – Wooden beams backed by steel plate

The construction and materials of the wooden beams backed by the steel frame (cross-section area 4) are shown in Figure E.10 and F.9. The predicted transmission loss is shown in Figure E.11 together with the transmission losses of cross-section areas 2 and 3.

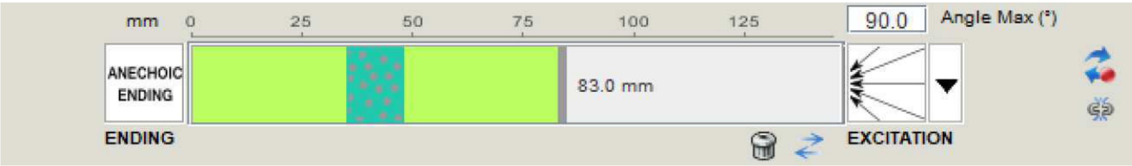

Figure E.10: AlphaCell model of the wooden beams backed by a steel plate (cross-section area 4).

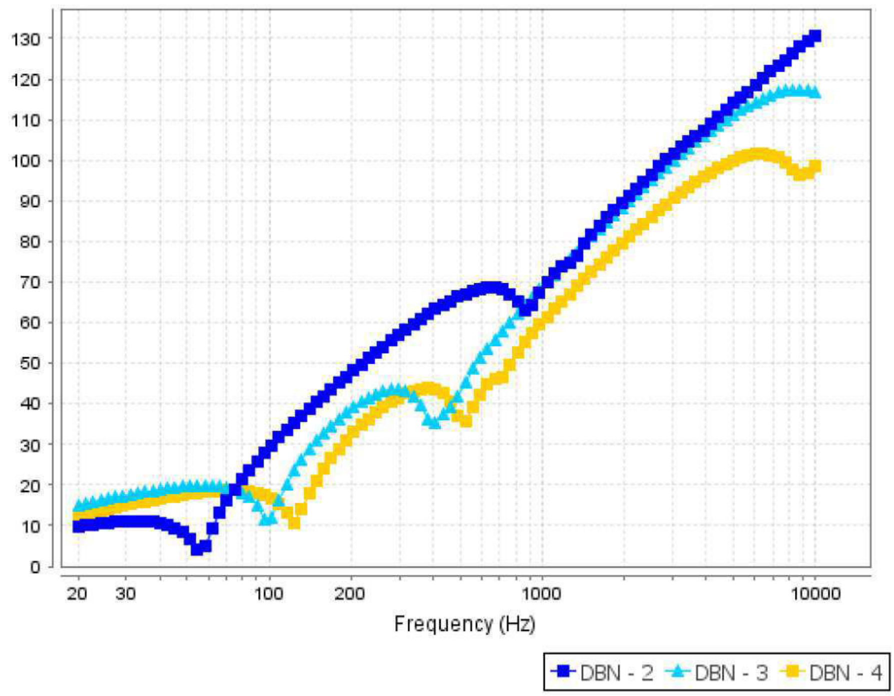

Figure E.11: Predicted transmission loss in dB of the different cross-section areas (2-4)

E.6.3 Combined transmission loss

The total transmission loss, when the wall cross-sections 1–4 are combined considering their respective areas, is shown in Figure E.12 for three different configurations mounted in the opening. In order to correctly measure the flanking transmission, the sound transmission loss with the closed opening should be at least 10 dB above the sound transmission loss with the mounted noise shield [1]. It can be seen that this is the case only in the frequency range ~150 Hz to 1.5 kHz when the bitumen-gypsum occlusion is mounted instead of the noise shield. When both are mounted together, as recommended in [1], this requirement is fulfilled above ~150 Hz. This would, therefore, be the preferable configuration. The measurement at low frequencies (< 300 Hz) would most likely additionally be influenced by other factors like an insufficient diffuseness of the sound field and the small size of the opening.

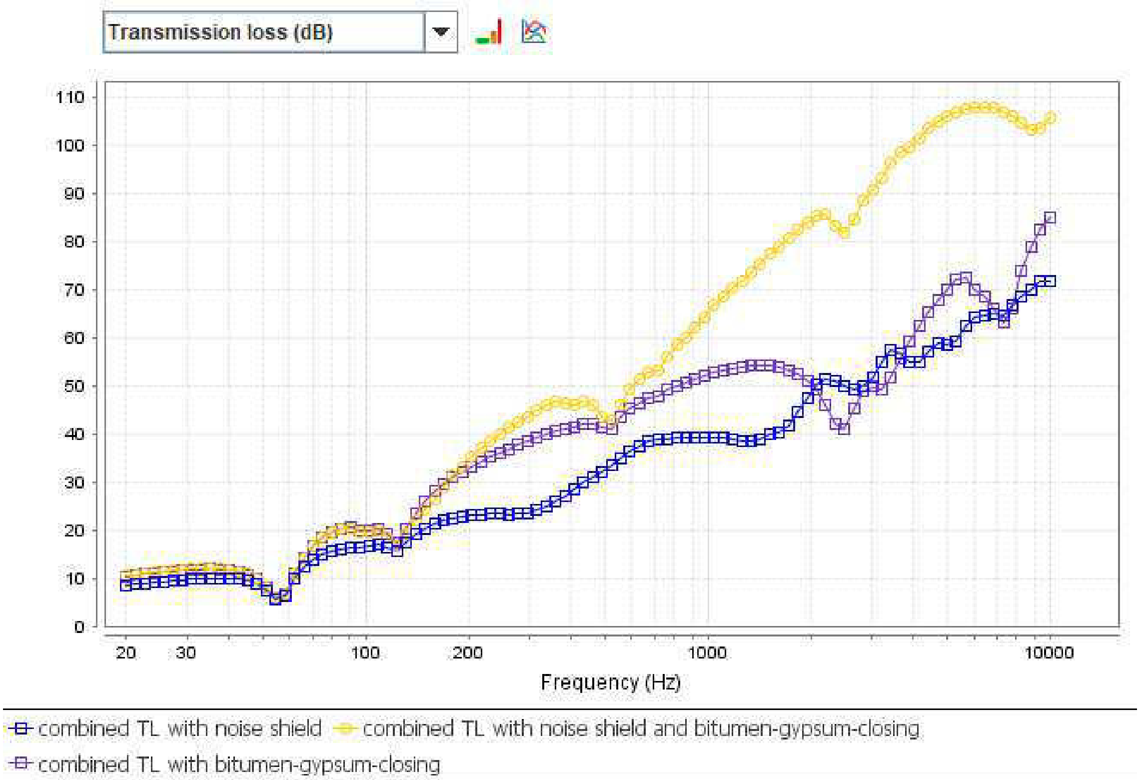

Figure E.12: Combined transmission loss of wall cross-section areas 1–4. The three versions are with just the noise shield in the opening, with just the bitumen-gypsum occlusion in the opening and with both mounted together as suggested in [1].

The procedure applied here (splitting up the wall into different areas, calculating the transmission loss for each area individually and then combining the results), does not account for interactions between the areas. For example, the vibrations of a gypsum plate in the middle of the wall will in reality be influenced by the wooden beams attached to its frame. Investigating this would require a detailed FEM or SEA model with accurate coupling conditions.

When building the double wall construction outlined here, there would most likely occur air gaps between the different layers. These should be included in the TMM model for a more accurate prediction.